Time-reversal symmetry and topology in one-dimensional Josephson junctions

by

Ehren Axel Mellars

A thesis submitted to
The University of Birmingham
for the degree of
DOCTOR OF PHILOSOPHY

Theoretical Physics Research Group
School of Physics and Astronomy
College of Engineering and Physical Sciences
The University of Birmingham

July 2018

Abstract

We explore the roles of topology and time-reversal symmetry in one-dimensional superconducting systems. Specifically, we examine junctions involving time-reversal-invariant topological superconductors, which are characterised by the emergence of zero-energy Majorana–Kramers pairs at their boundaries. For Josephson junctions composed of these superconductors, we obtain, through a scattering matrix technique valid in a regime where the junction length is much shorter than the superconducting coherence length, exact analytical and numerical results for the Josephson current in terms of a small number of independently measurable junction parameters. The current is found to have a number of prominent and robust features which indicate the underlying symmetries and the nontrivial topology inherent in these systems. The most remarkable of these features occurs in the form of switches in the Josephson current, where the sign of the current reverses as a consequence of crossings between energy levels in the subgap spectrum. By utilising a quantum master equation approach, we establish general conditions under which these switches manifest in relation to a phenomenological relaxation rate and a voltage applied across the junction. Our findings enable quantitative predictions for such junctions, potentially assisting in experimental directions regarding the detection of Majorana–Kramers pairs in mesoscopic Josephson systems.

Acknowledgements

First and foremost, I would like to thank my supervisor Dr. Benjamin Béri for his constant support and guidance over the course of my Ph.D., without which this thesis would not have been possible. We had numerous insightful and enjoyable discussions which greatly enriched my understanding of physics.

I recognise the amiable and professional environment provided by the Theoretical Physics Research Group, allowing for a satisfying and engaging Ph.D. experience. I would also like to give thanks to my friends and colleagues who have witnessed some part of this journey, including but not limited to: Matt H., Andy, Austin, Max, Matt R., Jack, Matt S., Gareth, Michael, and James. Lastly, I would like to thank my mother, father, and brother for the support they have given me this past quarter-century.

Publications

[1] E. A. Mellars and B. Béri, *Signatures of time-reversal-invariant topological superconductivity in the Jospehson effect,* Phys. Rev. B **94**, 174508 (2016).

Contents

List of Figures

Introduction

In 1937, the year preceding his mysterious disappearance, Ettore Majorana first disseminated the idea for a new type of fermionic particle which now bares his namesake: the Majorana fermion [1]. The profundity surrounding this fermion lies in its singular characteristic—it is a particle which is its own antiparticle. In the field of high-energy physics, present candidates for the Majorana fermion range from one of the initial suggestions by Ettore Majorana, the neutrino, to the supersymmetric complements of certain bosons [2]. However, despite the fervent interest in this particle, its experimental detection remains yet elusive.

Until relatively recently, the fascination with Majorana fermions has primarily been limited to physicists working in the context of high-energy physics. Almost twenty years ago, an analogue of the Majorana fermion started to become the subject of study in systems of condensed matter [3–6]. In such systems, the Majorana fermion is sought as a zero-energy quasiparticle excitation localised at the boundaries of so-called topological superconductors [7–9]. However, it was not till years later that an important intersection between Majorana fermions and topological insulators was made in the form of a concrete proposal to realise topological superconductors [10], galvanising the condensed matter community's interest in Majorana fermions. Stemming from this, much of the excitement regarding applications has been in proposals to utilise Majorana fermions for fault-tolerant topological quantum computation [11–13].

In this thesis, we explore the interplay between topology, superconductivity, and time-reversal symmetry. Each of these concepts is central to the systems we study: short,

one-dimensional Josephson junctions involving time-reversal-invariant topological superconductors. In the nontopological case, time-reversal symmetry has been known to allow for remarkable results regarding the Josephson current flowing between junctions composed of s-wave superconductors [14–19]. Taking this into consideration, the broad objective of this thesis is to investigate topological junctions with time-reversal symmetry in order to search for analogues of these relations, as well as to identify any strong features, which may be indicative of the underlying Majorana fermions, in the supercurrent that flows across these junctions.

The remainder of this thesis is structured as follows. In the first chapter, we formalise the idea of a Majorana fermion as a quasiparticle and motivate how superconductors are potential environments where the Majorana fermion can arise. By connecting the topological classification of Hamiltonians to superconductors, we can physically interpret the topology in terms of the ground state fermion parity of the superconductor. A toy model known as the Kitaev wire [6] is then reviewed, serving as a useful example to demonstrate the emergence of Majorana fermions as localised zero-energy states at interfaces between a topological superconductor and a nontopological region.

For the second chapter, we focus on the aspects related to time-reversal symmetry and the scattering matrix. We remark upon how time-reversal symmetry is motivated in physical systems with spin-half particles and how the important and well-known result of Kramers' theorem enters. We then pivot to how the scattering matrix can be formulated in relation to a mesoscopic scattering picture. For the systems that we consider throughout the rest of this thesis, the scattering matrix has constraints placed upon it by time-reversal symmetry and particle-hole symmetry. As an exemplary exercise, we review how the scattering matrix approach may be applied to nontopological Josephson junctions between s-wave superconductors in order to obtain the Josephson current arising from the subgap levels and the continuum [15]; similar techniques will be employed in the following chapter.

In the third chapter, we turn to original work investigating the signatures of topologi-

cal superconductivity in the Josephson effect for junctions between time-reversal-invariant topological superconductors.[1] By utilising the ideas developed earlier in this thesis, we formulate a scattering matrix description for one-dimensional Josephson junctions of this type, providing a powerful way to relate the excitation spectrum, and hence the Josephson current, with respect to only a small number of experimentally accessible parameters. By contrasting the results for topological junctions and their nontopological counterparts, we find, in the ac Josephson effect, a number of possible regimes with striking features that can serve as indicators of the nontrivial topological symmetries present in these systems.

For the fourth and final chapter, we describe a dynamical picture underlying one of the aforementioned regimes for topological junctions in terms of an energy relaxation originating from an effective electron-phonon coupling. Before this can happen, some preliminaries are in order. The first is to introduce the density matrix formalism, the primary objective of which is to trace out a reduced density operator for a small subsystem of interest with respect to a bipartite density operator that additionally incorporates a large reservoir. While the exact time evolution of this reduced density operator is given by the von Neumann equation, it ultimately involves the bipartite density operator. Therefore, the second preliminary is to present an outline of a microscopic derivation for the Lindblad form of the quantum master equation, enabling the time evolution of the reduced density operator to be described approximately without need for the full bipartite density operator. The remainder of this chapter regards original results. Through an effective low-energy description of junctions between time-reversal-invariant topological superconductors, the master equation is employed to investigate how the previously mentioned regime can be robustly established in relation to the energy relaxation rate and an applied voltage across the junction.

[1] This chapter is essentially as it appears in Ref. [1] of the Publications section.

Chapter 1

Majorana modes, superconductors, and topology

Topological superconductors in one dimension are characterised by the emergence of zero-energy quasiparticles at their boundaries. These zero-energy quasiparticles are the condensed matter analogue of the Majorana fermion and the purpose of this chapter is to provide a brief review on how they can manifest and to outline their connection with superconductivity and topology.

The remainder of this chapter is organised as follows. First, the Majorana fermion is formally introduced and a distinction is made to differentiate the fundamental Majorana fermion of high-energy physics with the Majorana mode of condensed matter physics. Some important properties of the Majorana mode are then expounded upon through a description in terms of fermions. Afterwards, a brief overview of the Bardeen–Cooper–Schrieffer theory commences, which culminates with the possibility that the Majorana mode may be realised as a superconducting quasiparticle. This leads into a discussion of how particle-hole symmetry and superconductivity are related, and how the former is key in the realisation of the Majorana mode. The discussion of symmetry then transitions to a topological argument concerning superconducting Hamiltonians, allowing for a topological invariant to be linked to the ground state fermion parity of a superconductor. Finally,

the preceding ideas converge in the Kitaev wire: a toy model where unpaired Majorana modes can emerge localised at the ends of the wire.

1.1 The Majorana operator

The hallmark of a Majorana fermion is that it is a particle which is its own antiparticle. This imposes the definitive condition of Hermiticity upon any Majorana operator γ,

$$\gamma^\dagger = \gamma. \tag{1.1}$$

In the context of high-energy physics, these particles also obey Fermi-Dirac statistics. For systems of condensed matter, however, the fermionic constraint is relaxed to requiring only that *different* particle operators anticommute and the term *Majorana operator* is used to describe quasiparticles which satisfy the Hermiticity condition [Eq. (1.1)].

Quasiparticle operators with the property of Hermiticity can be formed by combining fermionic operators. For instance, take an arbitrary fermion system with annihilation and creation operators c and $c^\dagger$; the Hermitian and anti-Hermitian parts of these operators are

$$\gamma_1 = c + c^\dagger, \tag{1.2a}$$

$$i\gamma_2 = \left(c - c^\dagger\right). \tag{1.2b}$$

By construction, the operators γ_1 and γ_2 are Hermitian. These operators, however, do not obey Fermi-Dirac statistics, as can be verified by taking

$$\{\gamma_1, \gamma_1\} = \{\gamma_2, \gamma_2\} = 2, \tag{1.3a}$$

$$\{\gamma_1, \gamma_2\} = 0, \tag{1.3b}$$

which is not the usual set of fermionic anticommutation relations. The operators γ_1 and

γ_2 do, however, anticommute *with each other*. Taken together with their Hermiticity, they are thus indeed Majorana operators.

From Eq. (1.2), it follows that $\gamma^2 = 1$ and hence there is no Pauli exclusion principle and also no way to define an occupation number for these operators; instead, in order for any fermionic intuition to be relevant, one must consider pairing up Majorana operators back into fermions, i.e.

$$c = \frac{1}{2}\left(\gamma_1 + i\gamma_2\right), \tag{1.4a}$$

$$c^\dagger = \frac{1}{2}\left(\gamma_1 - i\gamma_2\right). \tag{1.4b}$$

However, this raises the question as to the meaningfulness of describing a system in terms of Majorana operators; it so far seems superfluous to use them when a fermionic description is equivalent. It turns out, as shall be shown later in this chapter, that systems can be constructed where a pair of spatially separated Majorana operators appear as Majorana *modes*, i.e. operators corresponding to eigenstates of the system [6]. Of course, one still cannot populate or depopulate *these* eigenstates; however, one can do that with their linear combinations into ordinary fermion modes. If the Majorana modes are localised far apart from each other—as will be the case for the systems referred to here—the resulting fermion mode will be inherently nonlocal or, more precisely, bi-local due to the localised nature of the two underlying Majorana modes.

Furthermore, in Eq. (1.2), it is important to note that Majorana operators involve the superposition of an electron and a hole. As the quasiparticle modes which arise in superconducting systems involve combinations of this type, this suggests that superconductors may be of interest with respect to the realisation of Majorana modes. In order to explore this idea further, it is necessary to introduce some preliminaries regarding superconductivity.

1.2 Mean-field Bardeen–Cooper–Schrieffer theory

The Bardeen–Cooper–Schrieffer (BCS) theory [20] involves a microscopic model of superconductivity that incorporates an attractive electron-electron interaction which can be mediated by lattice phonons. A simple form of this model is described by the *reduced BCS Hamiltonian*,

$$H_{\mathrm{BCS}} = \sum_{\mathbf{k}\sigma} \epsilon_{\mathbf{k}} c^{\dagger}_{\mathbf{k}\sigma} c_{\mathbf{k}\sigma} + \frac{1}{2\Omega} \sum_{\substack{\mathbf{k}\mathbf{k}' \\ \sigma_1\sigma_2\sigma_3\sigma_4}} V_{\sigma_1\sigma_2\sigma_3\sigma_4}\left(\mathbf{k},\mathbf{k}'\right) c^{\dagger}_{\mathbf{k}\sigma_1} c^{\dagger}_{-\mathbf{k}\sigma_2} c_{-\mathbf{k}'\sigma_3} c_{\mathbf{k}'\sigma_4}, \tag{1.5}$$

where $c^{\dagger}_{\mathbf{k}\sigma}$ ($c_{\mathbf{k}\sigma}$) creates (annihilates) a fermion at an energy $\epsilon_{\mathbf{k}}$, with indices $\mathbf{k}$ and σ spanning respectively over momentum and spin; Ω is the system volume; and V is the potential between interacting pairs of electrons with symmetry properties following from the fermionic anticommutation relations [21, 22].

The mean-field (MF) approximation of the BCS theory is particularly useful. It involves taking the average number of Cooper pairs to be nonvanishing [23]. In the case of spin-singlet pairing, it is embodied by the BCS wavefunction ansatz [22]

$$|\Psi_{\mathrm{BCS}}\rangle = \prod_{\mathbf{k}} \left(u_{\mathbf{k}} + v_{\mathbf{k}} c^{\dagger}_{\mathbf{k}\uparrow} c^{\dagger}_{-\mathbf{k}\downarrow}\right) |0\rangle\,, \tag{1.6}$$

where $|u_{\mathbf{k}}|^2$ and $|v_{\mathbf{k}}|^2$ are the respective probability amplitudes for the absence and presence of pairs in the system, $|0\rangle$ is the vacuum state, and $\uparrow$ and $\downarrow$ respectively refer to spin-up and spin-down fermions. In the case of general spin-pairings, the mean-field approximation amounts to taking

$$\left(c^{\dagger}_{\mathbf{k}\sigma_1} c^{\dagger}_{-\mathbf{k}\sigma_2} - \left\langle c^{\dagger}_{\mathbf{k}\sigma_1} c^{\dagger}_{-\mathbf{k}\sigma_2} \right\rangle\right) \left(c_{-\mathbf{k}'\sigma_3} c_{\mathbf{k}'\sigma_4} - \left\langle c_{-\mathbf{k}'\sigma_3} c_{\mathbf{k}'\sigma_4} \right\rangle\right) = 0. \tag{1.7}$$

By ignoring constant terms and identifying the order parameter,

$$\Delta_{\mathbf{k}\sigma_1\sigma_2} = \frac{1}{\Omega}\sum_{\substack{\mathbf{k}'\\ \sigma_3\sigma_4}} V_{\sigma_1\sigma_2\sigma_3\sigma_4}\left(\mathbf{k},\mathbf{k}'\right)\left\langle c_{-\mathbf{k}'\sigma_3}c_{\mathbf{k}'\sigma_4}\right\rangle, \tag{1.8}$$

$$\Delta^*_{-\mathbf{k}\sigma_1\sigma_2} = -\frac{1}{\Omega}\sum_{\substack{\mathbf{k}'\\ \sigma_3\sigma_4}} V_{\sigma_3\sigma_4\sigma_1\sigma_2}\left(\mathbf{k}',\mathbf{k}\right)\left\langle c^\dagger_{\mathbf{k}'\sigma_3}c^\dagger_{-\mathbf{k}'\sigma_4}\right\rangle, \tag{1.9}$$

the BCS Hamiltonian may be recast into its mean-field form

$$H_{\mathrm{MF}} = \sum_{\mathbf{k}\sigma}\epsilon_{\mathbf{k}}c^\dagger_{\mathbf{k}\sigma}c_{\mathbf{k}\sigma} + \frac{1}{2}\sum_{\substack{\mathbf{k}\\ \sigma_1\sigma_2}}\left(\Delta_{\mathbf{k}\sigma_1\sigma_2}c^\dagger_{\mathbf{k}\sigma_1}c^\dagger_{-\mathbf{k}\sigma_2} - \Delta^*_{-\mathbf{k}\sigma_1\sigma_2}c_{-\mathbf{k}\sigma_1}c_{\mathbf{k}\sigma_2}\right). \tag{1.10}$$

Furthermore, by introducing the column and row vectors

$$\hat{\mathbf{c}}_{\mathbf{k}} = \begin{bmatrix} c_{\mathbf{k}\uparrow}\\ c_{\mathbf{k}\downarrow}\\ c^\dagger_{-\mathbf{k}\uparrow}\\ c^\dagger_{-\mathbf{k}\downarrow}\end{bmatrix}, \quad \hat{\mathbf{c}}^\dagger_{\mathbf{k}} = \begin{bmatrix} c^\dagger_{\mathbf{k}\uparrow} & c^\dagger_{\mathbf{k}\downarrow} & c_{-\mathbf{k}\uparrow} & c_{-\mathbf{k}\downarrow}\end{bmatrix} \tag{1.11}$$

the Hamiltonian may be written in the form

$$H_{\mathrm{MF}} = \frac{1}{2}\sum_{\mathbf{k}}\hat{\mathbf{c}}^\dagger_{\mathbf{k}}\begin{bmatrix}\epsilon_{\mathbf{k}}\mathbb{1}_2 & \hat{\Delta}_{\mathbf{k}}\\ -\hat{\Delta}^*_{-\mathbf{k}} & -\epsilon_{\mathbf{k}}\mathbb{1}_2\end{bmatrix}\hat{\mathbf{c}}_{\mathbf{k}}, \tag{1.12}$$

where we have assumed that the electron energies are measured from the chemical potential. The superconducting order parameter takes the form of a matrix with spin structure

$$\hat{\Delta}_{\mathbf{k}} = \begin{bmatrix}\Delta_{\mathbf{k}\uparrow\uparrow} & \Delta_{\mathbf{k}\uparrow\downarrow}\\ \Delta_{\mathbf{k}\downarrow\uparrow} & \Delta_{\mathbf{k}\downarrow\downarrow}\end{bmatrix}. \tag{1.13}$$

Fermionic anticommutation relations require that $\hat{\Delta}_{\mathbf{k}} = -\hat{\Delta}^{\mathsf{T}}_{-\mathbf{k}}$. This condition is divided into two more cases dependent on the pairing type; one is associated with spin-singlet pairing, requiring that

$$\hat{\Delta}_{\mathbf{k}} = \hat{\Delta}_{-\mathbf{k}} = -\hat{\Delta}^{\mathsf{T}}_{\mathbf{k}}, \tag{1.14}$$

and the other with spin-triplet pairing, amounting to

$$\hat{\Delta}_{\mathbf{k}} = -\hat{\Delta}_{-\mathbf{k}} = \hat{\Delta}_{\mathbf{k}}^{\mathsf{T}}. \tag{1.15}$$

The general form for the superconducting order parameter matrix can therefore be written in terms of these pairings as

$$\hat{\Delta}_{\mathbf{k}} = \left[D_0\left(\mathbf{k}\right) + \sum_{n=1}^{3} d_n\left(\mathbf{k}\right)\sigma_n \right] i\sigma_2 \tag{1.16}$$

where $D_0\left(\mathbf{k}\right)$ is an even function representing the singlet part of the pairing, the $d_n\left(\mathbf{k}\right)$ are odd functions associated with the triplet part of the pairing, and the σ_i that do not appear as indices are the i^{th} Pauli matrices [22].

In the case with spin-singlet pairing, the mean-field Hamiltonian [Eq. (1.10)] may be diagonalised by the Bogoliubov–Valatin transformation [24, 25]

$$\begin{aligned} \alpha_{\mathbf{k}\uparrow} &= u_{\mathbf{k}} c_{\mathbf{k}\uparrow} - v_{\mathbf{k}} c_{-\mathbf{k}\downarrow}^{\dagger}, \qquad & \alpha_{-\mathbf{k}\downarrow} &= u_{\mathbf{k}} c_{-\mathbf{k}\downarrow} + v_{\mathbf{k}} c_{\mathbf{k}\uparrow}^{\dagger}, \\ \alpha_{\mathbf{k}\uparrow}^{\dagger} &= u_{\mathbf{k}}^{*} c_{\mathbf{k}\uparrow}^{\dagger} - v_{\mathbf{k}}^{*} c_{-\mathbf{k}\downarrow}, \qquad & \alpha_{-\mathbf{k}\downarrow}^{\dagger} &= u_{\mathbf{k}}^{*} c_{-\mathbf{k}\downarrow}^{\dagger} + v_{\mathbf{k}}^{*} c_{\mathbf{k}\uparrow}, \end{aligned} \tag{1.17}$$

and the condition that $2\epsilon_{\mathbf{k}} u_{\mathbf{k}} v_{\mathbf{k}} + \Delta_{\mathbf{k}}^{*} v_{\mathbf{k}}^{2} - \Delta_{\mathbf{k}} u_{\mathbf{k}}^{2}$ and its conjugate vanish. The operators $\alpha_{\mathbf{k}\sigma}^{\dagger}$ are Bogoliubov quasiparticles which create excitations with a minimum energy $\Delta_{\mathbf{k}\sigma}$. While these quasiparticles are the combination of an electron and a hole, they fail to qualify as Majorana modes as a consequence of the constituent parts having opposite spin, which means that the necessary Hermiticity condition [Eq. (1.1)] is not satisfied. However, this failure serves to demonstrate that a different kind of spin-pairing—a spin-triplet type which renders the underlying fermions as effectively spinless—is required in order for a Bogoliubov quasiparticle to be realised as a Majorana mode. While the specific form of the spin-pairing that achieves this is important, it will be shown in the next section that, with respect to a particular symmetry of the Hamiltonian, a general condition involving quasiparticle energy can be formulated for the Majorana mode in superconductors.

As a final note, while the formal definition of symmetries is left to Chapter 2, for the purposes of establishing the connection between superconductors and Majorana modes, it is sufficient to understand the relevant symmetry of superconductors in terms of their eigenspectrum without need for further technical detail.

1.3 Particle-hole symmetry

Superconductors have the property of particle-hole symmetry, relating a positive eigenvalue of the BCS Hamiltonian to a negative eigenvalue of equal magnitude. To understand how this symmetry arises, the mean-field BCS Hamiltonian, in a slightly more convenient form, is taken as

$$H = \sum_{\alpha\beta=1}^{2N} \left[h_{\alpha\beta} c_\alpha^\dagger c_\beta + \frac{1}{2} \left(\Delta_{\alpha\beta} c_\alpha^\dagger c_\beta^\dagger + \Delta_{\alpha\beta}^* c_\beta c_\alpha \right) \right], \tag{1.18}$$

where there are N single-particle states, the indices α and β span over both lattice site and spin, the matrices h and Δ correspond to kinetic and order parameter terms, respectively, and the Fermi energy is taken to be zero. By introducing the vector of creation and annihilation operators

$$\begin{bmatrix} \mathbf{c}^\dagger & \mathbf{c} \end{bmatrix} = \begin{bmatrix} c_1^\dagger & c_2^\dagger & \dots & c_{2N}^\dagger & c_1 & c_2 & \dots & c_{2N} \end{bmatrix}, \tag{1.19}$$

the BCS Hamiltonian is recast into the compact form

$$H = \frac{1}{2} \begin{bmatrix} \mathbf{c}^\dagger & \mathbf{c} \end{bmatrix} H_{\mathrm{BdG}} \begin{bmatrix} \mathbf{c} \\ \mathbf{c}^\dagger \end{bmatrix}, \tag{1.20}$$

where the constant term equal to $\frac{1}{2} \operatorname{tr}(h)$ has been neglected. The square matrix H_{BdG} is the Bogoliubov–de Gennes (BdG) Hamiltonian, which has the form

$$H_{\mathrm{BdG}} = \begin{bmatrix} h & \Delta \\ -\Delta^* & -h^* \end{bmatrix} \tag{1.21}$$

and is of the order $4N$. It is important to note that the additional degrees of freedom introduced with the doubling from $2N$ to $4N$ are redundant, since the matrix $-h^*$ acts upon the same states as the matrix h.

The symmetry becomes apparent upon introducing the antiunitary operator

$$\mathcal{C} = \hat{\sigma}_1 \mathcal{K}, \tag{1.22}$$

where $\mathcal{K}$ is the complex conjugation operator and the matrix

$$\hat{\sigma}_1 = \sigma_1 \otimes \mathbb{1}_{2N}, \tag{1.23}$$

with the first Pauli matrix σ_1, is known as the particle-hole operator since it interchanges particles and holes via

$$\begin{bmatrix} \mathbf{c}^\dagger & \mathbf{c} \end{bmatrix} \hat{\sigma}_1 = \begin{bmatrix} \mathbf{c} & \mathbf{c}^\dagger \end{bmatrix}. \tag{1.24}$$

Furthermore, H_{BdG} and $\mathcal{C}$ anticommute,

$$\mathcal{C} H_{\mathrm{BdG}} \mathcal{C}^{-1} = -H_{\mathrm{BdG}}, \tag{1.25}$$

demonstrating the particle-hole symmetry of H_{BdG}. As a result of this, there is a symmetry in the spectrum of H_{BdG}

$$H_{\mathrm{BdG}} \psi = E \psi, \tag{1.26a}$$

$$H_{\mathrm{BdG}} \mathcal{C} \psi = -E \mathcal{C} \psi. \tag{1.26b}$$

Hence, when an eigenstate ψ is admitted with eigenenergy E, there must be a corresponding eigenstate $\mathcal{C}\psi$ with eigenenergy $-E$. This symmetry about $E = 0$ in terms of the eigenspectrum of H_{BdG} provides a way to intuitively understand particle-hole symmetry [26].

At this point, one might worry: what does it mean to have eigenstates with negative energy? The resolution to this question is in fact related to the possibility of having Majorana modes. To illustrate this, first consider the eigendecomposition of H_{BdG},

$$H_{\mathrm{BdG}} = U\Lambda U^{\dagger} \tag{1.27}$$

where Λ is the matrix of eigenvalues

$$\Lambda = \begin{bmatrix} \lambda & 0 \\ 0 & -\lambda \end{bmatrix}, \quad \lambda = \begin{bmatrix} E_1 & 0 & \dots & 0 & 0 \\ 0 & E_2 & \dots & 0 & 0 \\ \vdots & \vdots & \ddots & \vdots & \vdots \\ 0 & 0 & \dots & E_{2N-1} & 0 \\ 0 & 0 & \dots & 0 & E_{2N} \end{bmatrix}, \tag{1.28}$$

and U is the matrix of eigenvectors

$$U = \left[\psi_{E_1} \; \psi_{E_2} \; \dots \; \psi_{E_{2N}} \; \mathcal{C}\psi_{E_1} \; \mathcal{C}\psi_{E_2} \; \dots \; \mathcal{C}\psi_{E_{2N}} \right]. \tag{1.29}$$

Then, by identifying the quasiparticle operators

$$\alpha^{\dagger}_{E_k} = \begin{bmatrix} \mathbf{c}^{\dagger} & \mathbf{c} \end{bmatrix} \psi_{E_k}, \tag{1.30a}$$

$$\alpha_{E_k} = \psi^{\dagger}_{E_k} \begin{bmatrix} \mathbf{c} \\ \mathbf{c}^{\dagger} \end{bmatrix}, \tag{1.30b}$$

the BCS Hamiltonian can be diagonalised as

$$H = \frac{1}{2} \sum_{k=-2N}^{2N} E_k \alpha^{\dagger}_{E_k} \alpha_{E_k}. \tag{1.31}$$

Moreover, note that

$$\begin{aligned}\alpha_{-E_k} &= \mathcal{C}\psi^\dagger_{E_k}\begin{bmatrix}\mathbf{c}\\ \mathbf{c}^\dagger\end{bmatrix}\\ &= \begin{bmatrix}\mathbf{c} & \mathbf{c}^\dagger\end{bmatrix}\hat{\sigma}_1\mathcal{K}\psi^*_{E_k}\\ &= \alpha^\dagger_{E_k}\end{aligned} \tag{1.32}$$

which explicitly demonstrates that the process of creating a quasiparticle with an energy E_k is equivalent to removing a quasiparticle with an energy $-E_k$. Therefore, the redundancy that went into the description in Eq. (1.20) did not disappear: negative energy quasiparticles are, as they should be, artificial; their creation or annihilation corresponds to the respective annihilation or creation of their positive energy counterparts.

Provided that a nondegenerate quasiparticle exists at the Fermi energy $E_k = 0$, Eq. (1.32) becomes

$$\alpha_0^\dagger = \alpha_0 \tag{1.33}$$

which explicitly satisfies the Hermiticity condition [Eq. (1.1)] and so α_0 is a Majorana operator. As it is also linked to a zero-energy eigenstate, it is referred to as a *Majorana zero mode*. The importance of such modes being nondegenerate may be seen by considering the effect of perturbations, i.e. symmetry-preserving deformations of the Hamiltonian, on the case when it is not: if the zero mode is doubly degenerate, then particle-hole symmetry does not forbid perturbations from splitting the two modes away from zero energy to finite energies with equal magnitude but opposite sign. On the other hand, if the mode is nondegenerate, then, as a consequence of particle-hole symmetry, the zero mode is robust against perturbations as it cannot be shifted up or down in energy without violating the spectral symmetry. Hence, the existence of a nondegenerate zero mode can be viewed as an indicator that remains intact under continuous deformations. As this is precisely how topological indices behave, Majorana zero modes are said to be *topologically protected*.

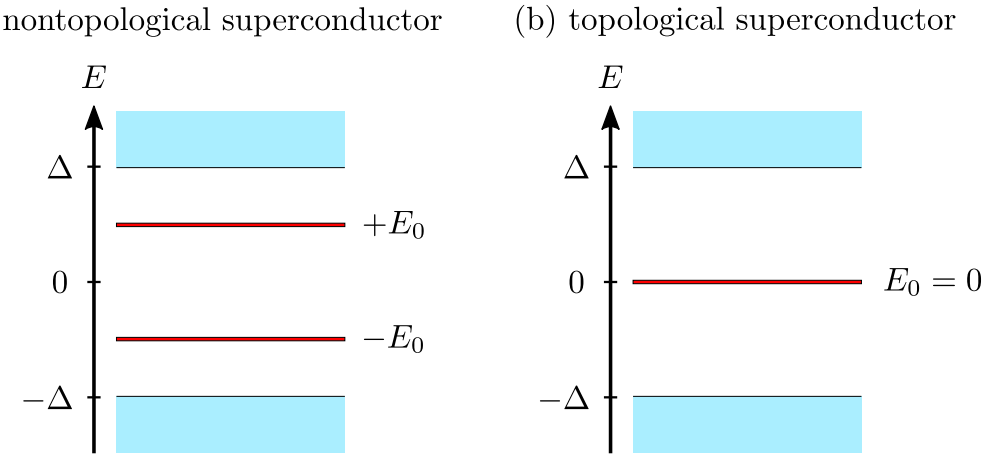

Figure 1.1: Schematic energy spectra of low-energy modes E_0 in a superconductor with superconducting gap Δ. (a) The mode at zero energy is degenerate and is susceptible to deformations that split modes symmetrically away from zero energy—such a superconductor is *nontopological*; (b) the mode at zero energy is nondegenerate and cannot be displaced by perturbations that respect particle-hole symmetry—such a superconductor is *topological*.

Both cases are sketched in Fig. 1.1.

An important caveat arises from the fact that superconductors are fundamentally comprised of fermions, so Majorana zero modes must always come in pairs [recall that it takes two Majorana operators to form an ordinary fermion operator—see Eq. (1.4)]. As a result of this, ordinary superconductors can never have exactly degenerate zero modes: as particle-hole symmetry does not rule out inter-Majorana couplings, terms that cause splitting away from the Fermi energy are inevitable. However, as will be discussed in Sec. 1.5.2, Majorana modes can be spatially localised with exponentially decaying wavefunction tails so that their coupling can be suppressed exponentially in the inter-Majorana distance. When focusing on the local physics near Majorana modes, we can thus, with exponential accuracy, consider it as a nondegenerate zero mode. Provided that there is a way to spatially separate these two states, the existence of Majorana zero modes in superconducting systems seems, so far, plausible.

1.4 Topological invariants

In the previous section, a somewhat nebulous link was made between topology and the protection of Majorana zero modes. In order to further elaborate upon this, a discussion of the topological classification of bulk Hamiltonians, which was alluded to in the preceding section when discussing the concept of deformations, and its connection to Majorana zero modes is necessary. Moreover, consideration of the relation between particle-hole symmetry and the aforementioned topological classification is appropriate.

The topological classification of Hamiltonians assigns every Hamiltonian a class defined by a topological invariant—an integer whose value does not change under continuous deformations. For Hamiltonians with a gap in their energy spectrum, two Hamiltonians H_{a} and H_{b} are defined to be in the same topological class if they can be continuously deformed into one another without closing the energy gap. For instance, consider the composite Hamiltonian $H(\alpha)$ which mixes H_{a} and H_{b} via a parameter $0 \leq \alpha \leq 1$,

$$H(\alpha) = \alpha H_{\mathrm{a}} + (1-\alpha) H_{\mathrm{b}}. \tag{1.34}$$

If the energy gap does not close at any point as α is swept from 0 to 1, then H_{a} and H_{b} are topologically equivalent. One should note that this is only a single path of deformation out of potentially many and the inverse is not generally true: finding the gap to close on a deformation path is not a sufficient condition to state that two Hamiltonians belong to distinct topological classes [27]. (Note that from this point onwards, when the closing and reopening of the gap is discussed, it is assumed that the participating levels actually cross through $E = 0$.)

Furthermore, deformations are constrained to be symmetry-preserving: in terms of the previous example, any relevant symmetries of H_{a} and H_{b} must remain intact over the domain of $H(\alpha)$. The effect of deformations respecting particle-hole symmetry can be understood in reference to the property that energies come in pairs E and $-E$: any deformation that moves one energy level must move its partner by an equal and opposite

amount. As a consequence of this, any deformation which involves the closure of the gap must involve an even number of levels crossing at zero energy; therefore, keeping in mind that the negative energy levels are effectively redundant, when a deformation closes and reopens the gap, it becomes energetically favourable to create or annihilate a quasiparticle, which essentially leads to a change in the fermion parity. Hence, a fermion parity flip effectively heralds the closure of the gap. As a superconductor conserves fermion parity in the absence of external processes, the fermion parity of the ground state can be viewed as a topological invariant [6]. (The value of this invariant, however, has no obvious connection to the Majorana zero mode introduced in the previous section. Nonetheless, it will be an essential ingredient for defining, in the next section, a different topological invariant that indicates the presence of Majorana zero modes.)

In terms of H_{BdG}, which we now take to have $2N$ eigenvalues, one might think the sign of its determinant a suitable candidate to be a measure of the ground state fermion parity as it is the product of all its energy eigenvalues

$$\det\left(H_{\mathrm{BdG}}\right) = \prod_{k=1}^{N}\left(-E_k^2\right), \tag{1.35}$$

of which there are levels which change sign at a gap closing; yet, under such a deformation, the sign of the determinant remains invariant as a result of two energy levels being involved in the crossing so that $\mathrm{sgn}\left[\det\left(H_{\mathrm{BdG}}\right)\right] = (-1)^N$ and the determinant's sign is set by the number of energy levels. Therefore, a different quantity involving H_{BdG} which accounts for this two-level crossing is required: the Pfaffian

$$\mathrm{pf}\left(A\right)^2 = \det\left(A\right), \tag{1.36}$$

which essentially allows for the square root of the determinant to be taken with a uniquely defined sign. Formally, this quantity may be calculated for $2N \times 2N$ antisymmetric

matrices $A = \{A_{ij}\}$ by

$$\mathrm{pf}\,(A) = \frac{1}{2^N N!} \sum_{\substack{i_1,i_2,\ldots,i_N=1 \\ j_1,j_2,\ldots,j_N=1}}^{2N} \epsilon_{i_1 j_1 i_2 j_2 \ldots i_N j_N} \prod_{n=1}^{N} A_{i_n j_n} \tag{1.37}$$

where $\epsilon_{i_1 j_1 i_2 j_2 \ldots i_N j_N}$ is the Levi-Civita symbol of dimension $2N$ [28]. So far, it remains to be seen what antisymmetric matrices and hence Pfaffians have to do with H_{BdG}. For this reason, consider the unitary transformation

$$H'_{\mathrm{BdG}} = \frac{1}{2} \begin{bmatrix} 1 & 1 \\ i & -i \end{bmatrix} H_{\mathrm{BdG}} \begin{bmatrix} 1 & -i \\ 1 & i \end{bmatrix}, \tag{1.38}$$

which, upon inclusion of a factor of i, has the form

$$iH'_{\mathrm{BdG}} = \frac{1}{2} \begin{bmatrix} i\,(h - h^*) + i\,(\Delta - \Delta^*) & (h + h^*) - (\Delta + \Delta^*) \\ -\,(h + h^*) - (\Delta + \Delta^*) & i\,(h - h^*) - i\,(\Delta - \Delta^*) \end{bmatrix} \tag{1.39}$$

and is real antisymmetric as a result of the Hermiticity of h and the antisymmetry of Δ [6, 29].

A real antisymmetric matrix may be decomposed [30] such that

$$iH'_{\mathrm{BdG}} = O \Sigma O^{\mathsf{T}}, \tag{1.40}$$

where O is a square orthogonal matrix of order $2N$ and Σ is a block-diagonal matrix chosen to have the form

$$\Sigma = \begin{bmatrix} i\sigma_2 E_1 & 0 & \ldots & 0 & 0 \\ 0 & i\sigma_2 E_2 & \ldots & 0 & 0 \\ \vdots & \vdots & \ddots & \vdots & \vdots \\ 0 & 0 & \ldots & i\sigma_2 E_{N-1} & 0 \\ 0 & 0 & \ldots & 0 & i\sigma_2 E_N \end{bmatrix}. \tag{1.41}$$

(For a discussion on how this decomposition arises, see Appendix A.) As one may choose the decomposition such that the nonzero elements of the superdiagonal of Σ only contain

positive eigenenergies (i.e. $E_n > 0$ for all n), and given that the determinant of an orthogonal matrix is ± 1, then, under a deformation which involves a single pair of eigenenergies crossing at zero energy, $\det(O)$ must change sign. This property of $\det(O)$ qualifies it as a measure of the ground state fermion parity. Furthermore, the relation between $\det(O)$ and $\mathrm{pf}\left(iH'_{\mathrm{BdG}}\right)$ may be seen through the identity [which follows from Eq. (1.37)]

$$\mathrm{pf}\left(O\Sigma O^{\mathsf{T}}\right) = \det(O)\,\mathrm{pf}(\Sigma)\,. \tag{1.42}$$

Then, by use of the identity $\mathrm{pf}(\Sigma) = \prod_{n=1}^{N} E_n > 0$, it follows that the sign of $\mathrm{pf}\left(iH'_{\mathrm{BdG}}\right)$ is the same as that of $\det(O)$. Therefore, a topological invariant $\mathcal{P}$ may be defined for H_{BdG} as

$$\mathcal{P} = \mathrm{sgn}\left[\mathrm{pf}\left(iH'_{\mathrm{BdG}}\right)\right] \tag{1.43}$$

and this can be physically interpreted as a direct measure of the ground state fermion parity because it flips sign upon a pair of energy eigenvalues crossing at zero energy [29].

Despite motivating the topological invariant $\mathcal{P}$ which tracks the ground state fermion parity for superconducting systems in quite a general way, we have not yet provided a topological invariant that indicates the presence of Majorana zero modes; that is, while at the point where the ground state fermion parity changes value seems to involve a mode at zero energy, the value of this parity alone is not sufficient to serve as an indicator for the existence of Majorana zero modes. To establish such an indicator for superconducting systems, it will turn out to be necessary to compare ground state fermion parities of the corresponding systems in the bulk. This is done in the following section for a toy model with the potential to host Majorana zero modes: the Kitaev wire or chain [6]. By studying the topological transitions of this model, the link between topology and the emergence of zero-energy modes can be clarified, providing a deeper meaning for the topological protection of Majorana zero modes.

1.5 The Kitaev wire

Consider an effectively spinless, one-dimensional p-wave superconductor with N sites. It has the following Hamiltonian

$$H = -\mu \sum_{j=1}^{N} \left(c_j^\dagger c_j - \frac{1}{2} \right) - \sum_{j=1}^{N-1} \left[t \left(c_j^\dagger c_{j+1} + c_{j+1}^\dagger c_j \right) + \Delta_0 e^{i\phi} c_j c_{j+1} + \Delta_0 e^{-i\phi} c_{j+1}^\dagger c_j^\dagger \right], \tag{1.44}$$

where the operator c_j annihilates a fermion at a site j, t is the tunnelling amplitude between neighbouring sites, μ is the chemical potential, Δ_0 is the superconducting order parameter, and ϕ is the superconducting phase. This toy model is known as the Kitaev wire [6] and is, as will be shortly demonstrated, an example of a system where Majorana zero modes can emerge.

Assuming that ϕ is constant for each site, it is convenient to absorb ϕ into the definition of the fermion operators

$$c_j \mapsto e^{-i\phi/2} c_j. \tag{1.45}$$

Moreover, by expressing the fermion operators in terms of their Majorana mode constituents

$$c_j = \frac{1}{2} \left(\gamma_{2j} - i\gamma_{2j-1} \right), \tag{1.46}$$

the Hamiltonian can be rewritten as

$$H = \frac{-i\mu}{2} \sum_{j=1}^{N} \gamma_{2j-1}\gamma_{2j} + \frac{i}{2} \sum_{j=1}^{N-1} \left[(t + \Delta_0)\, \gamma_{2j}\gamma_{2j+1} + (-t + \Delta_0)\, \gamma_{2j-1}\gamma_{2j+2} \right]. \tag{1.47}$$

In this form, two limiting cases become apparent. For the first, perhaps uninteresting,

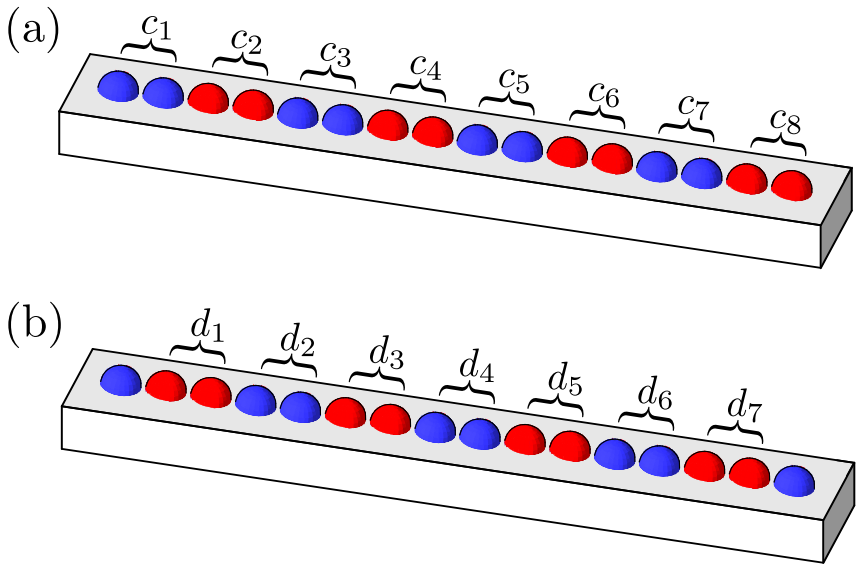

Figure 1.2: Visualisation of the Kitaev wire for $N = 8$ sites. Each hemisphere represents a Majorana mode and the pairing between modes is indicated by two adjacent hemispheres sharing the same colour. For (a) the pairing is such that every Majorana mode can be combined into a local fermion c_j, while in (b) the Majorana modes are paired into fermions d_j such that there is an unpaired Majorana mode at each end of the wire.

case, set $\Delta_0 = t = 0$ and $\mu < 0$, resulting in the Hamiltonian

$$H = -\frac{i\mu}{2} \sum_{j=1}^{N} \gamma_{2j-1}\gamma_{2j} \tag{1.48}$$

that pairs Majorana modes from the same fermion site [Fig. 1.2(a)] with zero occupation number in the ground state.

The second case is more interesting and involves setting $\Delta_0 = t > 0$ and $\mu = 0$, leading to the Hamiltonian

$$H = it \sum_{j=1}^{N-1} \gamma_{2j}\gamma_{2j+1}, \tag{1.49}$$

which pairs Majorana modes from different fermion sites [Fig. 1.2(b)]. An important feature in this case is that the Majorana modes associated with the edges of the wire are absent from the Hamiltonian. In order to understand the implications of this, one can

define new fermion operators which reflect the off-site Majorana pairing,

$$d_j = \frac{1}{2}\left(\gamma_{2j} + i\gamma_{2j+1}\right), \tag{1.50}$$

from which it follows

$$i\gamma_{2j}\gamma_{2j+1} = 2d_j^\dagger d_j - 1. \tag{1.51}$$

so that the Hamiltonian is actually diagonalised. Moreover, the Majorana modes at the edge may be combined into a nonlocal fermion

$$\tilde{d} = \frac{1}{2}\left(\gamma_{2N} - i\gamma_1\right), \tag{1.52}$$

and, as this fermion does not appear in the Hamiltonian in Eq. (1.49), it and its constituent Majorana modes must have zero energy (i.e. $[H, \gamma_1] = [H, \gamma_{2N}] = 0$). Therefore, the presence or absence of the nonlocal fermion results in a twofold degeneracy of the ground state [6].

So far it is not readily apparent what relevance the topological invariant $\mathcal{P}$, which was introduced in the previous section in Eq. (1.43) as a measure of the ground state fermion parity, has to the Majorana zero modes which arise in the Kitaev wire. The two regimes examined in the present section differ by how the Majorana modes are paired and the case with a nonlocal fermion seems to require a fine-tuning of parameters. However, as was mentioned before, the topological invariant indicating the presence of Majorana zero modes involves comparing the ground state fermion parities of the corresponding bulk Hamiltonians. Hence, to clarify the link between topology and the existence of Majorana zero modes, we turn to investigating the bulk properties of the Kitaev chain, where it will emerge that the condition for Majorana zero modes to exist is more general than is suggested by the fine-tuning in Eq. (1.49).

1.5.1 Bulk properties

The topological invariant $\mathcal{P}$ [Eq. (1.43)] is calculated from the Bogoliubov–de Gennes Hamiltonian and is a direct measure of the ground state fermion parity, essentially tracking the openings and closings of the energy gap. Therefore, when examining the related topological properties of the bulk Kitaev wire, it will first be necessary to obtain the Bogoliubov–de Gennes Hamiltonian and its energy eigenvalues. In order to facilitate this, periodic boundary conditions are first imposed before moving to momentum space via [23]

$$c_i = \frac{1}{\sqrt{N}} \sum_k e^{ikr_i} c_k, \tag{1.53}$$

allowing the Hamiltonian in Eq. (1.44) to be recast in terms of the Bogoliubov–de Gennes Hamiltonian

$$H(k) = \frac{1}{2} \sum_k \begin{bmatrix} c_k^\dagger & c_{-k} \end{bmatrix} H_{\mathrm{BdG}}(k) \begin{bmatrix} c_k \\ c_{-k}^\dagger \end{bmatrix}, \tag{1.54}$$

where

$$H_{\mathrm{BdG}}(k) = [-2t\cos(k) - \mu]\,\sigma_3 - 2\Delta_0 \sin(k)\,\sigma_2, \tag{1.55}$$

which obeys the particle-hole symmetry relation Eq. (1.25). [Note that, as momentum is explicit in the Hamiltonian, particle-hole symmetry relates $H_{\mathrm{BdG}}(k)$ to $H_{\mathrm{BdG}}(-k)$.] The resultant bulk energies

$$E_\pm = \pm\sqrt{[2t\cos(k) + \mu]^2 + 4\Delta_0^2 \sin^2(k)} \tag{1.56}$$

are depicted in Fig. 1.3. While a gap generally exists in k-space, there are two exceptions: at $\mu = -2t$, where the gap closes at $k = 0$, and at $\mu = 2t$, where the gap closes at $k = \pi$. Why exactly the gap closings at these particular k-points are pertinent is related

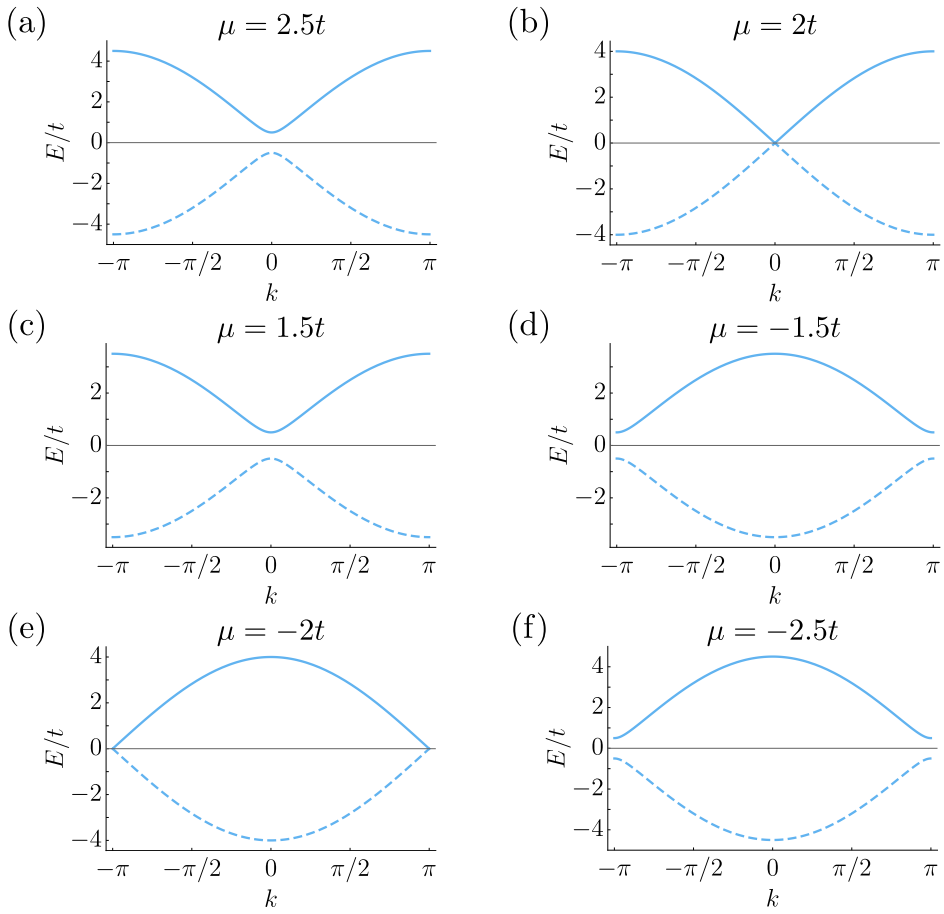

Figure 1.3: Bulk energies E as a function of the momentum k are shown for the Kitaev wire for various values of the chemical potential μ in terms of the tunnelling amplitude t and superconducting gap $\Delta_0 = t$. The levels are symmetric about $E = 0$ as a result of particle-hole symmetry. The wire is generally gapped, except at $k = 0$ for (b) and at $k = \pi$ for (e), indicating a topological transition.

to particle-hole symmetry: they map onto themselves for $k \mapsto -k$, so a single energy is permitted to cross at these special points; in contrast, crossings away from these points are constrained to only occur in pairs so that they cannot flip the fermion parity.

The topological invariant $\mathcal{M}$ that indicates the presence of Majorana zero modes in the open Kitaev chain can be defined in terms of the ground state fermion parities $\mathcal{P}$ of the corresponding bulk Hamiltonians $H_{\mathrm{BdG}}(k)$ at these special k-points, i.e.

$$\mathcal{M} = \operatorname{sgn}\left\{\operatorname{pf}\left[iH'_{\mathrm{BdG}}(0)\right]\operatorname{pf}\left[iH'_{\mathrm{BdG}}(\pi)\right]\right\}, \tag{1.57}$$

where the transformed $H'_{\mathrm{BdG}}(k)$ follows from Eq. (1.38). This quantity $\mathcal{M}$ is the ratio of the ground state fermion parity between a Kitaev ring with periodic boundary conditions to one with antiperiodic boundary conditions. Why exactly the value of $\mathcal{M}$ indicates the presence or absence of Majorana zero modes in the open Kitaev chain can be concisely understood by closing the open chain into a ring via coupling the first Majorana operator γ_1 to the last γ_{2N} through λt, where $\lambda \in [-1, 1]$. When $\lambda = -1$, antiperiodic boundary conditions are enforced, while for $\lambda = 1$ periodic boundary conditions are enforced. Therefore, when the fermion parities of the antiperiodic and periodic Kitaev rings differ (i.e. $\mathcal{M} = -1$), there must be a fermion parity flip as λ is varied over its interval and this occurs (for large enough N) at $\lambda = 0$. This value of λ is precisely where the ring is cut and the open Kitaev chain is recovered. Hence, a zero-energy mode must exist in the open Kitaev chain when $\mathcal{M} = -1$. Furthermore, as was the case in Eq. (1.49), this zero-energy mode is localised to the edge and this will be formally shown in Sec. 1.5.2.

Evaluating Eq. (1.57) yields

$$\mathcal{M} = \operatorname{sgn}\left[(-2t - \mu)(2t - \mu)\right] = \begin{cases} +1 & \text{if } |\mu| > 2t, \\ -1 & \text{if } |\mu| < 2t, \end{cases} \tag{1.58}$$

and, as a single closing and reopening of the gap signals a topological phase transition, there are two distinct topological phases controlled by the relative values of μ and t. The positive sign corresponds to the on-site pairing [e.g., Fig. 1.2(a)] and is the *topologically trivial* or *nontopological* phase, while the negative sign corresponds to the off-site pairing [e.g., Fig. 1.2(b)] which leaves the two Majorana modes at the edges unpaired and is the *topologically nontrivial* or *topological* phase. Moreover, we note that the nontopological phase is topologically equivalent to the system in Eq. (1.48), while the topological phase is topologically equivalent to the system in Eq. (1.49).

Additionally, one can check whether the zero mode is present and, if it is, that it is located at $\lambda = 0$ by taking the Kitaev chain for a given number of fermion sites N and calculating its energies as a function of λ for a given value of μ. This is displayed

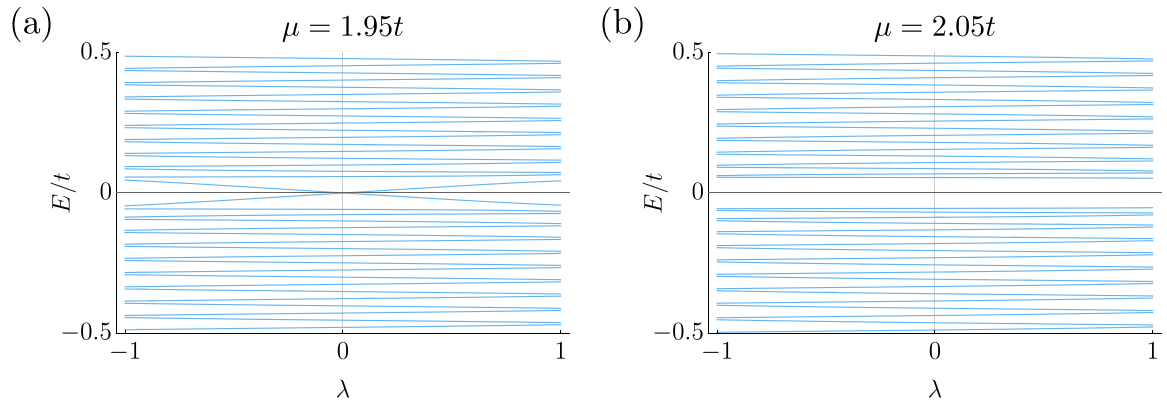

Figure 1.4: The energies of the Kitaev chain for $N = 300$ sites as a function of the parameter λ which couples the first Majorana operator to the last. The presence of the mode at zero energy is determined by the topological invariant $\mathcal{M}$ defined in Eq. (1.58). The chemical potential μ is taken relative to the tunnelling amplitude t between fermion sites such that the zero mode is present in (a) but absent in (b). The superconductor pairing is $\Delta_0 = 1.25t$.

in Fig. 1.4 for $N = 300$ sites with $\Delta_0 = 1.25t$, demonstrating that a zero-energy mode is present at $\lambda = 0$ for $\mathcal{M} = -1$ and absent when $\mathcal{M} = 1$.

1.5.2 Bulk-boundary correspondence

The hallmark of the topological Kitaev wire is the occurrence of Majorana zero modes at the wire's edges, where the term "edge" refers to the real space interface between a nontopological and a topological phase. It remains to be seen how such modes are localised in the system if one considers working away from the special case of $\mu = 0$ and $t = \Delta$ where we have seen that the Majorana zero modes are localised to a single site. In order to clarify this, it is useful to linearise the Bogoliubov–de Gennes Hamiltonian [Eq. (1.55)]

$$H_{\mathrm{BdG}}(k) = (-2t - \mu)\,\sigma_3 - 2k\Delta\sigma_2, \tag{1.59}$$

where the coefficient of the first term is effectively a mass term m and its sign is crucial. The linearised Hamiltonian in real space reads

$$H_{\mathrm{BdG}}(x) = m(x)\,\sigma_3 - i\sigma_2\partial_x, \tag{1.60}$$

where the edge is explicitly incorporated into the Hamiltonian by allowing the mass term to vary in real space. Placing the boundary at $x = 0$ and imposing the requirement

$$\mathrm{sgn}\left[m(x)\right] = \begin{cases} -1 & \text{if } x < 0, \\ 0 & \text{if } x = 0, \\ +1 & \text{if } x > 0. \end{cases} \tag{1.61}$$

enforces a topological phase to the left of the boundary and a nontopological phase to the right of the boundary. Upon requiring the existence of zero-energy modes, the partial differential equation follows

$$\partial_x \psi(x) = \sigma_1 m(x)\,\psi(x), \tag{1.62}$$

which admits only one normalisable solution for the wavefunction

$$\psi(x) = \exp\left[-\int_0^x m\left(x'\right)\mathrm{d}x'\right]\begin{bmatrix} 1 \\ -1 \end{bmatrix}. \tag{1.63}$$

Therefore, provided a zero-energy mode is present, it must be localised at the boundary between a nontopological and a topological region with its peak centred about the point in space where the sign change of $m(x)$ occurs [see Fig. 1.5]. Such boundaries could be realised, for example, between a nontopological and a topological Kitaev wire or the vacuum (which effectively has $\mu \to -\infty$) and a topological Kitaev wire.

This also provides a deeper meaning to the topological invariant defined in Eq. (1.57). The negative value of the topological invariant indicates a switch in the fermion parity of the bulk Hamiltonian between $k = 0$ and $k = \pi$, effectively signalling an odd number of crossings at zero energy between these k-points. Therefore, notwithstanding finite-size

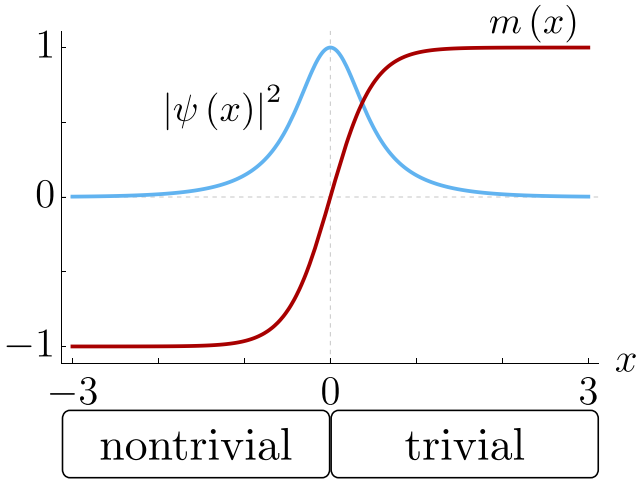

Figure 1.5: Amplitude $|\psi(x)|^2$ (blue curve) and smoothly varying mass term $m(x) = \tanh(2x)$ (red curve) at the interface $x = 0$ between a topological region ($x < 0$) and a nontopological region ($x > 0$). The Majorana zero mode is localised at the edge with exponentially decaying wavefunction tails.

effects, zero-energy modes emerge in the wire localised with exponential accuracy at the boundary. This link between the bulk invariant and the zero-energy edge states is the *bulk-boundary correspondence*. Moreover, though motivated by linearising the Kitaev model in Eq. (1.59), from Eq. (1.60) onwards our considerations only assumed that there was a single (linear) gap closing and nothing else specific about the Kitaev wire. Therefore, the condition for the existence of zero-energy edge states has been generalised to any interface between topological and nontopological superconducting regions regardless of the microscopic details.

1.6 Summary

In this chapter, we have focused on showing how unpaired Majorana modes can emerge in systems of condensed matter. By considering the spectrum of eigenstates associated with particle-hole-symmetric Hamiltonians, the Majorana mode was linked to zero-energy quasiparticles, naturally motivating superconductors as candidates for realising the Majorana zero mode. Building upon these ideas, the model of the Kitaev wire was reviewed, where the topological protection of Majorana zero modes was established upon linking

it to the ratio of the ground state fermion parity of the periodic Kitaev ring to the antiperiodic Kitaev ring. Finally, the connection between topology and the Majorana zero mode was solidified in the bulk-boundary correspondence, demonstrating that the zero-energy state must appear localised at the interface between a nontopological system and a topological system.

These concepts surrounding the Majorana zero mode that can arise in superconductors provide a basis upon which they can be further investigated in more complex systems, as will be done in Chapters 3 and 4. However, the systems under study there warrant further groundwork. For this reason, the concepts of time-reversal symmetry and scattering at mesoscopic normal–superconductor interfaces are introduced in the next chapter.

Chapter 2

Time-reversal symmetry and mesoscopic normal–superconductor interfaces

Time-reversal symmetry provides a powerful way to characterise Hamiltonian systems that has extensive consequences in terms of the system's eigenspectrum; it will be our broad objective to formulate this symmetry in such a way that it can be incorporated seamlessly for the Josephson junction. As a first step, time-reversal symmetry will be intuitively motivated in quantum mechanics by imposing general symmetry conditions on the operation of time inversion $t \mapsto -t$. This allows for the property of time-reversal symmetry to be understood in relation to the eigenspectrum of a system's Hamiltonian, with clear implications for the Majorana zero mode introduced in the previous chapter.

The effects of time-reversal symmetry are then explored in reference to a scattering picture of electronic transport, which is formulated in terms of a one-dimensional mesoscopic system. For a normal system, the central object of interest is the normal-state scattering matrix, which encapsulates entirely the scattering information of the system and whose form has additional constraints for time-reversal-invariant systems. For scattering processes between normal–superconductor interfaces, a special type of reflection

known as Andreev reflection can occur, enabling current transfer across the interface through the retroreflection of an electron to a hole or vice versa.

Consequently, these ideas enable the study of one-dimensional systems composed of two superconducting leads interposed by a normal region—the Josephson junction. Towards this end, we review the quasi-one-dimensional system originally investigated by Beenakker [15], which is concerned with calculating the observable current which may flow across a spinless, time-reversal-invariant junction between s-wave superconductors in the so-called short-junction limit. This serves as an illustrative example which lays the foundations to effectively extend this analysis to the single-channel topological junctions that are studied in Chapter 3.

2.1 Symmetries in quantum mechanics

Symmetry in quantum mechanics refers to a class of transformations which preserve the transition probability between any two states Ψ and Φ in a Hilbert space. For such a transformation M, this amounts to

$$|\langle M\Psi|M\Phi\rangle| = |\langle\Psi|\Phi\rangle|\,. \tag{2.1}$$

A unitary operator U would satisfy this requirement as

$$\langle U\Psi|U\Phi\rangle = \langle\Psi|\Phi\rangle\,. \tag{2.2}$$

Moreover, an antiunitary operator $A = UK$ with conjugation operator K, acting definitively through

$$\langle A\Psi|A\Phi\rangle = \langle\Psi|\Phi\rangle^*\,, \tag{2.3}$$

would also satisfy the conservation of transition probability. These properties are central to Wigner's theorem: symmetry operators preserve transition probability and, in order to do so, must be represented uniquely by unitary or antiunitary operators [31].

To elaborate on the concept of symmetries in quantum mechanics, it is useful to consider how they act on the trajectories of a quantum system. The Schrödinger equation

$$i\hbar\frac{\partial}{\partial t}\left|\psi\left(t\right)\right\rangle = H\left|\psi\left(t\right)\right\rangle, \tag{2.4}$$

which admits a unitary solution at arbitrary time t_0

$$\left|\psi\left(t\right)\right\rangle = e^{-iHt/\hbar}\left|\psi\left(t_0\right)\right\rangle, \tag{2.5}$$

is said to possess a particular symmetry related to M if the corresponding states $\left|\phi\left(t\right)\right\rangle = M\left|\psi\left(t\right)\right\rangle$ are also valid solutions. In this way, symmetries of a quantum system can be viewed as (anti)unitary bijections between two sets of states.

2.2 Time-reversal symmetry

The central idea of time reversal is the inversion of time $t \mapsto -t$. This definition is supplemented by the intuitive idea that any reversal of time should not introduce any change to the magnitude of the rate at which time passes. With respect to a system which is invariant under time reversal, if one considers the system in a particular state at a given time, then applying time reversal to that state and allowing it to evolve for a time t before applying time reversal again and allowing it to evolve for the same duration, the original state should be recovered up to a phase factor [31, 32].

More formally, we now start to consider the properties of the operator $\mathcal{T}$ associated with time reversal. First, we assume that we are dealing with a Hamiltonian H which is time-reversal-invariant, i.e. $\mathcal{T}^{-1}H\mathcal{T} = H$. Now, whether $\mathcal{T}$ is an antiunitary or a unitary operator can be deduced by considering the Schrödinger equation. We take a state $\left|\psi\left(t\right)\right\rangle$

which obeys the forward-evolving Schrödinger equation

$$i\frac{\partial}{\partial t}\left|\psi\left(t\right)\right\rangle = H\left|\psi\left(t\right)\right\rangle . \tag{2.6}$$

The corresponding states related by time-reversal symmetry $\mathcal{T}\left|\psi\left(t\right)\right\rangle$ must obey the backward-evolving Schrödinger equation

$$i\frac{\partial}{\partial\left(-t\right)}\mathcal{T}\left|\psi\left(t\right)\right\rangle = H\mathcal{T}\left|\psi\left(t\right)\right\rangle . \tag{2.7}$$

After operating from the left with $\mathcal{T}$ and using the time-reversal invariance of H, then

$$\mathcal{T}^{-1}i\frac{\partial}{\partial\left(-t\right)}\mathcal{T}\left|\psi\left(t\right)\right\rangle = H\left|\psi\left(t\right)\right\rangle . \tag{2.8}$$

By matching Eqs. (2.6) and (2.8), it follows that

$$\mathcal{T}^{-1}i\frac{\partial}{\partial\left(-t\right)}\mathcal{T} = i\frac{\partial}{\partial t}. \tag{2.9}$$

Since $\mathcal{T}$ does not depend on t, we therefore have that

$$\mathcal{T}^{-1}i\mathcal{T} = -i, \tag{2.10}$$

from which one can conclude that $\mathcal{T}$ is antiunitary [33].

Now that $\mathcal{T}$ has been determined as an antiunitary operator, further properties of $\mathcal{T}$ can be discussed. First, antiunitary operators are defined as in Eq. (2.3). Now, consider two antiunitary matrices A_1 and A_2. Their product A_1A_2 is a unitary matrix U. Then, letting $A_1 = \mathcal{T}$ and $A_2 = K$, we have that

$$\mathcal{T}K = U \tag{2.11}$$

which, operating on the right by K, results in the standard form for an antiunitary matrix

$$\mathcal{T} = UK. \tag{2.12}$$

As argued at the start of this section, the double application of time reversal returns the original state up to a phase factor

$$\mathcal{T}^2 = e^{i\theta} \tag{2.13}$$

where θ is a real number. By substituting Eq. (2.12) into Eq. (2.13), it follows that

$$U^* = e^{i\theta}U^\dagger = e^{i2\theta}U^* \tag{2.14}$$

where the right equality follows from applying the left equality iteratively to itself. Hence $\theta = n\pi$ with n being an integer, or, in terms of the time-reversal operator,

$$\mathcal{T}^2 = \pm 1 \tag{2.15}$$

where the choice of sign depends on a number of factors, the most crucial being the spin of the particles under consideration [31]. In order to clarify this further, it is convenient to discuss the effect of time reversal on a system which admits position and momentum operators X and P.

As the essence of time reversal is the inversion of time, it is not unreasonable to assume that the position operator should be invariant under time reversal

$$X = \mathcal{T}X\mathcal{T}^{-1}. \tag{2.16}$$

Additionally, by requiring that the usual commutation relation

$$[X, P] = i\hbar \tag{2.17}$$

is consistent with an antiunitary time-reversal operator such that

$$\mathcal{T}\,[X,P]\,\mathcal{T}^{-1} = -i\hbar, \tag{2.18}$$

then it follows that the momentum operator must satisfy the relation

$$P = -\mathcal{T}P\mathcal{T}^{-1}. \tag{2.19}$$

Given that the operator for linear momentum transforms in this way, it is assumed to also hold for the total angular momentum operator J, i.e.

$$J = -\mathcal{T}J\mathcal{T}^{-1}, \tag{2.20}$$

where both the orbital and spin angular momenta obey relations of the same form. In terms of a spin-1/2 particle, this amounts to the following set of equations involving the Pauli matrices

$$\sigma_1 = -\mathcal{T}\sigma_1\mathcal{T}^{-1}, \tag{2.21a}$$

$$\sigma_2 = -\mathcal{T}\sigma_2\mathcal{T}^{-1}, \tag{2.21b}$$

$$\sigma_3 = -\mathcal{T}\sigma_3\mathcal{T}^{-1}, \tag{2.21c}$$

which allows for the specific form of $\mathcal{T}$ to be derived. The unitary matrix appearing in the time-reversal operator [Eq. (2.12)] may be parameterised via

$$U = e^{i\chi}e^{-i\frac{\theta}{2}\sigma_3}e^{-i\frac{\zeta}{2}\sigma_2}e^{-i\frac{\eta}{2}\sigma_3}, \tag{2.22}$$

where the parameters χ, θ, ζ, and η are all real numbers [34]. In order to satisfy Eq. (2.21c), $\zeta = (2m+1)\pi$ must hold with an integer m, while for Eqs. (2.21a) and (2.21b) it must be that $\theta = l\pi$ and $\eta = n\pi$ with integers l and n satisfying $l + n = 0 \pmod 2$.

We take

$$\theta = 0, \quad \zeta = -\pi, \quad \eta = 0, \tag{2.23}$$

so that

$$U = e^{i\chi}\sigma_2 \tag{2.24}$$

where the phase χ may be chosen freely. Conventionally $\chi = \pi$ is chosen, resulting in the following form for the time-reversal operator for a spin-1/2 particle

$$\mathcal{T} = i\sigma_2 K \tag{2.25}$$

and the choice of sign in Eq. (2.15) may be evaluated explicitly to give the negative sign $\mathcal{T}^2 = -1$ [26].

2.2.1 Kramers' theorem

So far it remains to be seen what effect time-reversal symmetry has on a system in terms of its eigenspectrum. Given that a time-reversal-invariant Hamiltonian admits a solution

$$H\left|\psi\right\rangle = E\left|\psi\right\rangle, \tag{2.26}$$

it follows that, owing to the commutativity between H and $\mathcal{T}$, the time-reversed solution shares this eigenenergy via

$$H\mathcal{T}\left|\psi\right\rangle = E\mathcal{T}\left|\psi\right\rangle. \tag{2.27}$$

Moreover, for time-reversal operators that square to negative unity, one can write

$$\langle\psi|\mathcal{T}\psi\rangle = \left\langle\mathcal{T}\psi\middle|\mathcal{T}^2\psi\right\rangle^* = -\langle\psi|\mathcal{T}\psi\rangle\,, \tag{2.28}$$

where the property of antiunitarity [Eq. (2.3)] has been used, demonstrating the orthogonality between a state and its time-reversed partner. Therefore, the eigenvalues of H are doubly degenerate—a result known as *Kramers' degeneracy theorem* [26, 35].

In the context of topological superconductors with time-reversal symmetry, Kramers' degeneracy theorem provides an intuitive way to distinguish them from their time-reversal-broken counterparts. For example, in relation to the Majorana zero mode that emerges at each boundary of the the Kitaev wire (as discussed in Sec. 1.5), time-reversal symmetry can be viewed as a property which, when additionally imposed upon the system, doubles the number of modes so that there are now a pair of Majorana zero modes at each end of the wire. These Majorana–Kramers pairs are robust not only because they cannot be split away from one another while time-reversal symmetry is present, but also because they cannot be moved together away from zero energy without violating particle-hole symmetry. Topological systems with Majorana–Kramers pairs will be the primary subject of study in Chapters 3 and 4.

With the idea of eigenstates coming in pairs related by time-reversal symmetry in mind, a general property of time-reversal-invariant Hamiltonians can be derived by considering the Hamiltonian structure. First, the basis of a $2N \times 2N$ system with time-reversal symmetry may be chosen such that there are N states with N distinct time-reversed pairs (i.e. represented by kets $|n\rangle$ and $\mathcal{T}|n\rangle$, where n is a number from 1 to N). Taking the basis states $|n\rangle$ to be invariant with respect to the complex conjugation operator K, the time-reversal operator acts on a generic state via

$$|\psi\rangle = \sum_n \left(c_{n+}|n\rangle + c_{n-}\mathcal{T}|n\rangle\right), \tag{2.29a}$$

$$\mathcal{T}|\psi\rangle = \sum_n \left(c^*_{n+}\mathcal{T}|n\rangle - c^*_{n-}|n\rangle\right), \tag{2.29b}$$

so that the time-reversal operator acting on each subspace spanned by a time-reversed pair has the form

$$\mathcal{T} = -i\sigma_2 K. \tag{2.30}$$

The structure of the Hamiltonian H can then be thought of as being an $N \times N$ block matrix

$$H = \begin{bmatrix} h_{1,1} & h_{1,2} & \dots & h_{1,N-1} & h_{1,N} \\ h_{2,1} & h_{2,2} & \dots & h_{2,N-1} & h_{2,N} \\ \vdots & \vdots & \ddots & \vdots & \vdots \\ h_{N-1,1} & h_{N-1,2} & \dots & h_{N-1,N-1} & h_{N-1,N} \\ h_{N,1} & h_{N,2} & \dots & h_{N,N-1} & h_{N,N} \end{bmatrix} \tag{2.31}$$

with its elements as 2×2 submatrices involving products between two states and their time-reversed pairs

$$h_{mn} = \begin{bmatrix} \langle m|H|n\rangle & \langle m|H|\mathcal{T}n\rangle \\ \langle \mathcal{T}m|H|n\rangle & \langle \mathcal{T}m|H|\mathcal{T}n\rangle \end{bmatrix}. \tag{2.32}$$

By choosing to represent the 2×2 submatrices by the general complex parameterisation [34]

$$h_{mn} = a_{mn}^{(0)}\mathbb{I}_2 - i\sum_{k=1}^{3} a_{mn}^{(k)}\sigma_k, \tag{2.33}$$

time-reversal symmetry then imposes the following condition on every submatrix

$$\begin{aligned} h_{mn} &= \left(\mathcal{T}H\mathcal{T}^{-1}\right)_{mn} \\ &= \sigma_2 h_{mn}^{*}\sigma_2 \\ &= a_{mn}^{(0)*}\mathbb{I}_2 - i\sum_{k=1}^{3} a_{mn}^{(k)*}\sigma_k, \end{aligned} \tag{2.34}$$

so that the parameters $a_{mn}^{(\kappa)}$ with $\kappa = 0, 1, 2, 3$ are all real. A matrix with this property is

said to be *quaternion real* [26]. Furthermore, this property extends to the full $2N \times 2N$ Hamiltonian, as it can be written in the form

$$H = A_0 \otimes \mathbb{1}_2 - i \sum_{k=1}^{3} A_k \otimes \sigma_k, \tag{2.35}$$

where

$$A_\kappa = \begin{bmatrix} a_{1,1}^{(\kappa)} & a_{1,2}^{(\kappa)} & \dots & a_{1,N-1}^{(\kappa)} & a_{1,N}^{(\kappa)} \\ a_{2,1}^{(\kappa)} & a_{2,2}^{(\kappa)} & \dots & a_{2,N-1}^{(\kappa)} & a_{2,N}^{(\kappa)} \\ \vdots & \vdots & \ddots & \vdots & \vdots \\ a_{N-1,1}^{(\kappa)} & a_{N-1,2}^{(\kappa)} & \dots & a_{N-1,N-1}^{(\kappa)} & a_{N-1,N}^{(\kappa)} \\ a_{N,1}^{(\kappa)} & a_{N,2}^{(\kappa)} & \dots & a_{N,N-1}^{(\kappa)} & a_{N,N}^{(\kappa)} \end{bmatrix}, \tag{2.36}$$

so that time-reversal symmetry requires that

$$A_\kappa = A_\kappa^* \tag{2.37}$$

and so the Hamiltonian is also quaternion real. This property will be a necessary condition to be enforced when the parameterisation of Hamiltonians with time-reversal symmetry is required in Chapter 4.

2.3 The mesoscopic scattering picture

Electronic transport in mesoscopic systems can be understood in terms of a quantum mechanical scattering picture: the Landauer-Büttiker approach [36–39]. It is assumed that the system under consideration can be treated as a mesoscopic sample which is connected by leads to macroscopic conductors that serve as reservoirs, providing electrons that are able to undergo scattering in the sample.

In terms of incoming and outgoing modes at a scattering region, electronic transport is characterised by the wavefunction, which may be labelled by incoming amplitudes a_m,

as

$$\Psi = \sum_m a_m \psi_{\text{in}}^{(m)} \tag{2.38}$$

or, by outgoing amplitudes b_n, as

$$\Psi = \sum_n b_n \psi_{\text{out}}^{(n)}. \tag{2.39}$$

Here $\psi_{\text{in}}^{(m)}$ and $\psi_{\text{out}}^{(n)}$ each comprise a separate full and orthonormal basis for a given energy and are normalised such that the states $\psi_{\text{in}}^{(m)}$ and $\psi_{\text{out}}^{(n)}$ carry the same amount of probability current. (They are the so-called scattering states [40, 41].) Given that $\psi_{\text{in}}^{(m)}$ and $\psi_{\text{out}}^{(n)}$ span the same Hilbert space and have the same normalisation, the coefficients a_m and b_n are related by a unitary basis transformation. The matrix for this transformation is provided by the matrix of scattering amplitudes, i.e. the scattering matrix S_{nm} [42]

$$b_n = \sum_m S_{nm} a_m. \tag{2.40}$$

By considering a scattering setup involving a mesoscopic sample in contact with two leads (as depicted in Fig. 2.1), the incoming and outgoing amplitudes can be collected into vectors of size $2N$ (with N being the number of channels in a lead) which are subdivided according to the two leads into N component subvectors $\mathbf{a}_+, \mathbf{a}_-, \mathbf{b}_-$, and $\mathbf{b}_+$, so that

$$\mathbf{a} = \begin{bmatrix} \mathbf{a}_+ \\ \mathbf{a}_- \end{bmatrix}, \quad \mathbf{b} = \begin{bmatrix} \mathbf{b}_- \\ \mathbf{b}_+ \end{bmatrix}, \tag{2.41}$$

where the positive sign indicates right-moving modes and the negative sign left-moving modes. This subdivision of amplitudes introduces a corresponding block structure for the scattering matrix

$$S = \begin{bmatrix} r & t' \\ t & r' \end{bmatrix}, \tag{2.42}$$

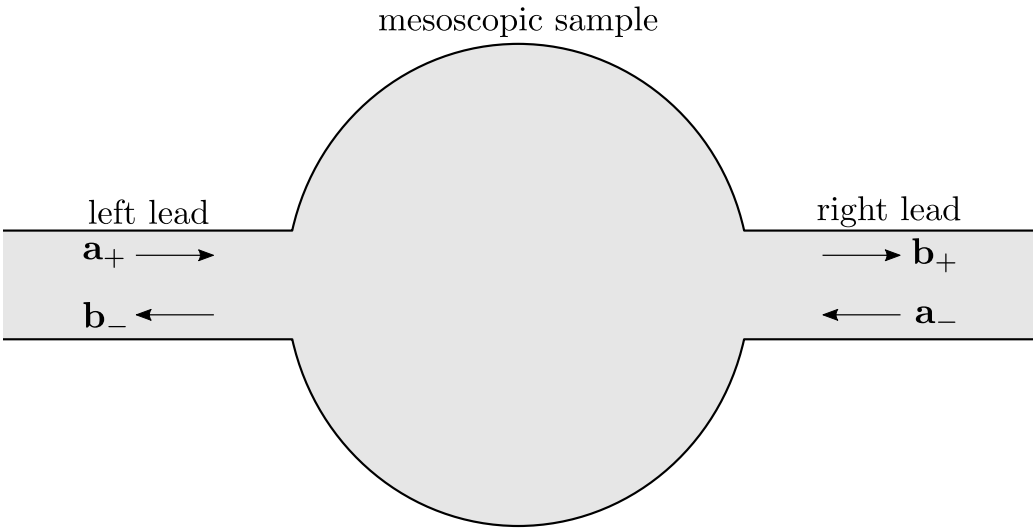

Figure 2.1: Scattering picture of a mesoscopic sample (circular area) in contact with two leads (rectangular protrusions); the incoming modes are described by the vector of coefficients $\mathbf{a}_\pm$ and the outgoing modes by the vector of coefficients $\mathbf{b}_\pm$, where the positive and negative signs respectively indicate right-moving and left-moving modes.

where the $N \times N$ matrices r and r' respectively encode the reflection of the modes described by a_+ into b_- and of a_- into b_+ and the $N \times N$ matrices t and t' respectively encode the transmission of the modes from a_+ to b_+ and from a_- to b_-. Thus, by using the matrix of amplitudes r, t, r', and t', it may be more intuitively understood how the scattering matrix contains the information regarding the scattering properties of the system [41].

Furthermore, the unitarity of the scattering matrix ensures that the probability current (or particle number) is conserved. Given the normalisation of $\psi_{\text{in}}^{(m)}$ and $\psi_{\text{out}}^{(n)}$, this amounts to the relation

$$|\mathbf{a}|^2 = |\mathbf{b}|^2 \,, \tag{2.43}$$

so that the incident electron flux is equal to the outgoing electron flux. This is indeed manifestly satisfied since

$$|\mathbf{b}|^2 = (S\mathbf{a})^\dagger \, S\mathbf{a} = \mathbf{a}^\dagger S^\dagger S \mathbf{a} = |\mathbf{a}|^2 \,. \tag{2.44}$$

2.3.1 Particle-hole symmetry and time-reversal symmetry

In order to address the constraints that particle-hole symmetry and time-reversal symmetry place on the scattering matrix, it is necessary to explicitly consider a setup as depicted in Fig. 2.1 in greater detail. In such a picture, assuming that there is no scattered part, an eigenstate may be written as

$$\psi_{n\alpha,E}\left(x,y\right)=u_{n\alpha,E}\left(x,y\right)\left|\alpha\right\rangle \tag{2.45}$$

where x and y are the respective horizontal (longitudinal) and vertical (transverse) space co-ordinates which describe an appropriately bounded region that spans the system and $\left|\alpha\right\rangle$ is some basis state with four components arising from a spin–particle-hole grading. The coefficient $u_{n\alpha,E}\left(x,y\right)$ appearing on the right-hand-side may be determined with respect to the transverse component $\chi_{n}\left(y\right)$,

$$u_{n\alpha,E}=\frac{1}{\sqrt{k_{n\alpha}}}e^{ik_{n\alpha}x}\chi_{n}\left(y\right),\quad\tilde{u}_{n\alpha,E}=\frac{1}{\sqrt{k_{n\alpha}}}e^{-ik_{n\alpha}x}\chi_{n}\left(y\right) \tag{2.46}$$

where n is a quantum number that labels the transverse mode of a lead, $E=\hbar^{2}k_{n\alpha}^{2}/2m+\epsilon_{n}$ is the corresponding energy with wavenumber $k_{n\alpha}$ and transverse energy contribution ϵ_{n}, and the tilde refers to particles travelling in the opposite direction [41]. In what follows, n and the spatial co-ordinates (x,y) are suppressed for brevity.

A scattering state $\psi_{\text{in}}^{(m)}\left(E\right)$, focusing on its wavefunction within the leads, may therefore be written in terms of an incoming part and a scattered part as

$$\psi_{\alpha,E}=u_{\alpha,E}\left|\alpha\right\rangle+\sum_{\beta}S_{\beta\alpha}\left(E\right)\tilde{u}_{\beta,E}\left|\beta\right\rangle, \tag{2.47}$$

and a general eigenstate at energy E (or, more precisely, the part thereof within the leads)

is a superposition of such terms [see Eq. (2.38)]

$$\begin{aligned}\Psi_E &= \sum_\alpha c_\alpha \psi_{\alpha,E} \\ &= \sum_\alpha c_\alpha u_{\alpha,E} \left|\alpha\right\rangle + \sum_\beta \left[S\left(E\right)\mathbf{c}\right]_\beta \tilde{u}_{\beta,E} \left|\beta\right\rangle . \end{aligned} \tag{2.48}$$

With respect to the grading, the basis is chosen such that the first two entries can be viewed as particles which are differentiated by their spin, while the last two are the corresponding holes.

With this setup, it is now possible to describe the constraint of particle-hole symmetry on the scattering matrix. The particle-hole operator in this basis is

$$\mathcal{C} = \hat{\sigma}_1 K, \tag{2.49}$$

where K is the complex conjugation operator defined with respect to the basis α and $\hat{\sigma}_1 = \sigma_1 \otimes \mathbb{1}_2$ with σ_i as the i^{th} Pauli matrix. The particle-hole operator applied to some basis state then formally yields

$$\mathcal{C} u_{\alpha,E} \left|\alpha\right\rangle = u^*_{\alpha,E} \hat{\sigma}_1 \left|\alpha\right\rangle . \tag{2.50}$$

Intuitively, $\mathcal{C}$ just relates $u_{\alpha,E}\left|\alpha\right\rangle$ to its particle-hole partner (see Fig. 2.2). Therefore, we may take

$$\mathcal{C} u_{\alpha,E} \left|\alpha\right\rangle = \sum_\beta \left(\hat{\sigma}_1\right)_{\beta\alpha} u_{\beta,-E} \left|\beta\right\rangle , \tag{2.51}$$

where, summing over β, the particle-hole operator ensures the correct index of u is chosen relative to α. Next, consider the action of the particle-hole operator on a general

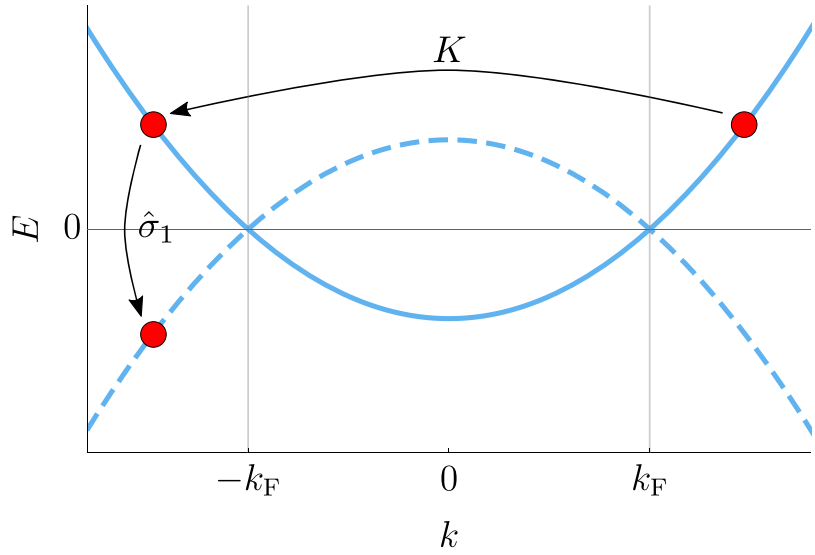

Figure 2.2: The energy-momentum relation for a normal metal, where the solid and dashed blue lines represent the electron and hole branches, respectively. The antiunitary operator $\mathcal{C} = \hat{\sigma}_1 K$ acts sequentially on an electron (red circle at $k > 0$), where conjugation K relates it to the electron at opposite momentum (upper red circle at $k < 0$), before relating it to its corresponding hole (lower red circle at $k < 0$) through the particle-hole operator $\hat{\sigma}_1$.

superposition of these states

$$\begin{aligned}\mathcal{C}\Psi_E &= \sum_\alpha c_\alpha^* \left(\hat{\sigma}_1 K u_{\alpha,E} \left|\alpha\right\rangle\right) + \sum_\beta \left[S\left(E\right)\mathbf{c}\right]_\beta^* \left(\hat{\sigma}_1 K \tilde{u}_{\beta,E} \left|\beta\right\rangle\right) \\ &= \sum_\alpha \left(\hat{\sigma}_1 K \mathbf{c}\right)_\alpha u_{\alpha,-E} \left|\alpha\right\rangle + \sum_\beta \left[\hat{\sigma}_1 K S\left(E\right)\mathbf{c}\right]_\beta \tilde{u}_{\beta,-E} \left|\beta\right\rangle . \end{aligned} \tag{2.52}$$

Upon appropriately inserting unity $\mathbb{1}_4 = \hat{\sigma}_1 K \hat{\sigma}_1 K$ and identifying the transformed coefficients $\mathbf{w} = \hat{\sigma}_1 K \mathbf{c}$, this becomes

$$\mathcal{C}\Psi_E = \sum_\alpha w_\alpha u_{\alpha,-E} \left|\alpha\right\rangle + \sum_\beta \left[\hat{\sigma}_1 S^*\left(E\right)\hat{\sigma}_1 \mathbf{w}\right]_\beta \tilde{u}_{\beta,-E} \left|\beta\right\rangle . \tag{2.53}$$

However, as particle-hole symmetry relates solutions with opposite energy, then it follows

that $\mathcal{C}\Psi_E = \Psi_{-E}$ and hence the solution

$$\mathcal{C}\Psi_E = \sum_\alpha \hat{w}_\alpha u_{\alpha,-E} \left|\alpha\right\rangle + \sum_\beta \left[S\left(-E\right)\hat{\mathbf{w}}\right]_\beta \tilde{u}_{\beta,-E} \left|\beta\right\rangle \tag{2.54}$$

exists for some vector coefficient $\hat{\mathbf{w}}$. By matching the first terms of Eq. (2.53) and Eq. (2.54), it follows that $\hat{\mathbf{w}} = \mathbf{w}$. Equating the second terms results in

$$S\left(E\right) = \hat{\sigma}_1 S\left(-E\right)^* \hat{\sigma}_1, \tag{2.55}$$

which is the property that the scattering matrix must satisfy as a result of particle-hole symmetry.

For a system with time-reversal symmetry, the time-reversal operator $\mathcal{T} = i\breve{\sigma}_2 K$, where $\breve{\sigma}_2 = \mathbb{1}_2 \otimes \sigma_2$, acts upon some collection of basis states via

$$\begin{aligned}\mathcal{T}\sum_\alpha c_\alpha u_{\alpha,E} \left|\alpha\right\rangle &= \sum_\alpha c_\alpha^* \tilde{u}_{\beta,E} \sum_\beta \left(i\breve{\sigma}_2\right)_{\beta\alpha} \left|\beta\right\rangle \\ &= \sum_\beta \left(i\breve{\sigma}_2 K\mathbf{c}\right)_\beta \tilde{u}_{\beta,E} \left|\beta\right\rangle,\end{aligned} \tag{2.56}$$

where it has been used that the time-reverse of the right-moving coefficient $u_{\alpha,E}$ is the corresponding left-moving coefficient $\tilde{u}_{\beta,E}$. Therefore, for a general combination of states

$$\begin{aligned}\mathcal{T}\Psi_E &= \sum_\alpha \left(i\breve{\sigma}_2 K\mathbf{c}\right)_\alpha \tilde{u}_{\alpha,E} \left|\alpha\right\rangle + \sum_\beta \left[i\breve{\sigma}_2 KS\left(E\right)\mathbf{c}\right]_\beta u_{\beta,E} \left|\beta\right\rangle \\ &= \sum_\alpha \left[i\breve{\sigma}_2 KS\left(E\right)^\dagger Ki\breve{\sigma}_2^{\mathsf{T}}\mathbf{v}\right]_\alpha \tilde{u}_{\alpha,E} \left|\alpha\right\rangle + \sum_\beta v_\beta u_{\beta,E} \left|\beta\right\rangle,\end{aligned} \tag{2.57}$$

where the transformed set of coefficients $\mathbf{v} = i\breve{\sigma}_2 KS\left(E\right)\mathbf{c}$ has been used. However, the time-reverse of a given superposition should just map the incident states onto the scattered

states and vice versa. Therefore, it is generally required that

$$\mathcal{T}\Psi_E = \sum_\alpha \left[S\left(E\right)\breve{\mathbf{v}}\right]_\alpha \tilde{u}_{\alpha,E}\left|\alpha\right\rangle + \sum_\beta \breve{v}_\beta u_{\beta,E}\left|\beta\right\rangle \tag{2.58}$$

for some vector coefficient $\breve{\mathbf{v}}$. By matching the second terms of Eq. (2.57) and Eq. (2.58), it follows that $\breve{\mathbf{v}} = \mathbf{v}$. Equating the first terms yields

$$S\left(E\right) = \breve{\sigma}_2 S\left(E\right)^{\mathsf{T}} \breve{\sigma}_2, \tag{2.59}$$

which is the property of the scattering matrix following from time-reversal symmetry.

It should be noted that, in the spinless case, the basis may be taken to effectively reduce to half the size of that in the spinful case. As the particle-hole symmetry grading remains, the condition it imposes on the scattering matrix does not change. However, the effect of time-reversal symmetry on the scattering matrix is altered due to the absence of spin-space, resulting in the simpler relation $S\left(E\right) = S\left(E\right)^{\mathsf{T}}$.

Moreover, when it comes to mesoscopic systems involving topological superconductors, it is convenient to adopt a basis that alters the form of the condition imposed by particle-hole symmetry on the scattering matrix. Further information on this basis change and how it affects time-reversal symmetry and particle-hole symmetry is presented in Appendix B.

2.3.2 Scattering at a normal–superconductor interface

We now shift from a general scattering picture involving electrons and holes in a normal metal to the types of scattering that can occur at the interface between a normal metal and a superconductor. There are a number of important differences for scattering processes at this type of interface which are best discussed in terms of scatterers with an energy below the gap ($E < \Delta$) and above the gap ($E > \Delta$).

For an electron (hole) emanating from the normal metal with an energy magnitude

less than the gap, there are two possibilities. The first of these is normal reflection, where an electron (hole) retraces its path with almost opposite velocity, and no current is transmitted to the superconducting side as a result. The second type is known as *Andreev reflection*, where an electron (hole) is retroreflected as a hole (electron). In order to conserve charge, this retroreflection must be accompanied by the transmittance of a charge of magnitude $2e$—a Cooper pair—through to the superconducting side. Therefore, in contrast to normal reflection, Andreev reflection enables a finite current to flow across the interface.

For an electron (hole) originating from the normal metal with an energy magnitude larger than the gap, there are three possibilities. Two of these are the aforementioned normal and Andreev reflections. The third process is transmission, where an incident electron (hole) joins with a hole (electron) at the interface to form a Bogoliubov quasiparticle which extends indefinitely into the superconductor.

To understand these scattering processes in more detail, one may consider the Blonder-Tinkham-Klapwijk model [43] for a spinless system. Suppose that the interface is one-dimensional and located at $x = 0$, with the lead normal for $x < 0$ and superconducting for $x > 0$ with s-wave symmetry. Deep within the normal part of the system, the electron and hole wavefunctions are characterised by the equations

$$\begin{bmatrix} -\frac{\hbar^2}{2m}\partial_x^2 - \epsilon_{\mathrm{F}} & 0 \\ 0 & \frac{\hbar^2}{2m}\partial_x^2 + \epsilon_{\mathrm{F}} \end{bmatrix} \begin{bmatrix} \psi_{\mathrm{e}}(x) \\ \psi_{\mathrm{h}}(x) \end{bmatrix} = E \begin{bmatrix} \psi_{\mathrm{e}}(x) \\ \psi_{\mathrm{h}}(x) \end{bmatrix}, \tag{2.60}$$

where ϵ_{F} is the Fermi energy and the wavefunction forms a vector $\Psi(x)$ with an electron-part $\psi_{\mathrm{e}}(x)$ and a hole-part $\psi_{\mathrm{h}}(x)$. The electron and hole solutions decouple

$$\psi_{\mathrm{e}}(x) \propto \begin{bmatrix} 1 \\ 0 \end{bmatrix} e^{\pm ikx}, \quad \psi_{\mathrm{h}}(x) \propto \begin{bmatrix} 0 \\ 1 \end{bmatrix} e^{\pm ikx} \tag{2.61}$$

where

$$k = k_{\mathrm{F}}\sqrt{1 \pm \frac{E}{\epsilon_{\mathrm{F}}}}, \tag{2.62}$$

with the positive sign corresponding to electrons, the negative sign to holes, and k_{F} as the Fermi momentum. In the Andreev approximation [44], where $E \ll E_{\mathrm{F}}$, these momenta may be taken at first order to be

$$k = k_{\mathrm{F}} \pm \frac{E}{\hbar v_{\mathrm{F}}} \tag{2.63}$$

so that the magnitudes of their momenta are equivalent up to a small mismatch controlled by the energy.

Similarly, deep within the superconductor, the Bogoliubov–de Gennes equations are

$$\begin{bmatrix} -\frac{\hbar^2}{2m}\partial_x^2 - \epsilon_{\mathrm{F}} & \Delta \\ \Delta^* & \frac{\hbar^2}{2m}\partial_x^2 + \epsilon_{\mathrm{F}} \end{bmatrix} \begin{bmatrix} \tilde{\psi}_{\mathrm{e}}(x) \\ \tilde{\psi}_{\mathrm{h}}(x) \end{bmatrix} = E \begin{bmatrix} \tilde{\psi}_{\mathrm{e}}(x) \\ \tilde{\psi}_{\mathrm{h}}(x) \end{bmatrix}, \tag{2.64}$$

and now the electron-like and hole-like solutions are coupled. By again assuming a plane-wave form for each component, the energy-momentum relation is

$$E = \pm\sqrt{\left(1 - \frac{k^2}{k_{\mathrm{F}}^2}\right)\epsilon_{\mathrm{F}}^2 + |\Delta|^2}. \tag{2.65}$$

The energies described on the normal side [Eq. (2.62)], along with their superconducting counterparts [Eq. (2.65)], allow for an intuitive picture to understand the different types of scattering that can occur for particles impinging from the normal metal at a normal-superconducting interface (Fig. 2.3).

At the interface, solutions are taken directly from the linearised Bogoliubov–de Gennes equations. (The linearisation amounts to having implemented the Andreev approximation.) For the case where Andreev reflection occurs, such that an electron inbound

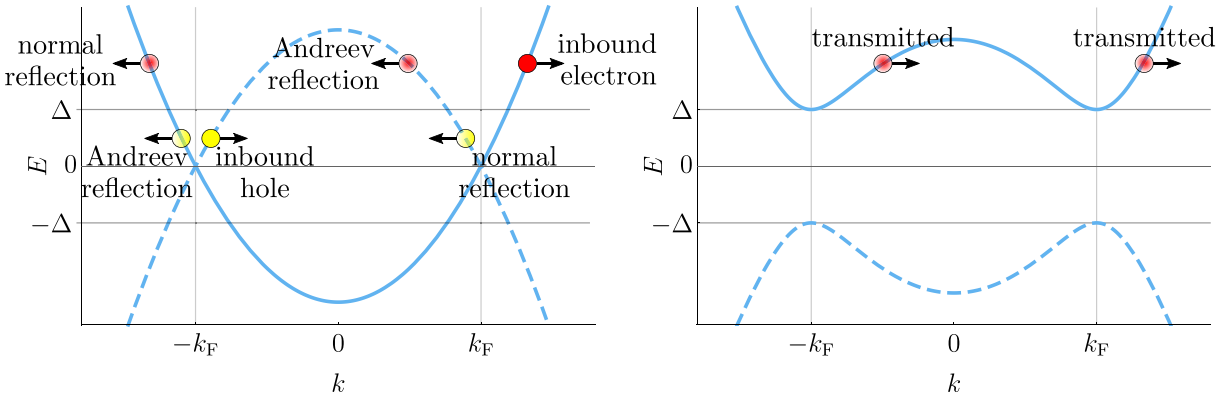

Figure 2.3: An intuitive schematic of the scattering processes that may occur at a normal–superconductor interface. The graphs are energy-momentum relations for normal-state conductors (left) and superconductors (right), with electron (solid lines) and hole (dashed lines) branches. The solid circles represent an incoming particle, while the faded circles represent the respective scattered parts. An incoming electron (red circle) with energy greater than the superconducting gap ($E > \Delta$) can be normally reflected as an electron, Andreev reflected as a hole, or transmitted into the superconductor as an electron-like quasiparticle. Alternatively, an incoming hole (yellow circle) with energy below the superconducting gap ($E < \Delta$) can either undergo normal reflection or Andreev reflection.

from the normal lead is reflected as a hole, these equations are

$$\begin{bmatrix} -i\hbar v_{\mathrm{F}}\partial_x & \Delta \\ \Delta^* & i\hbar v_{\mathrm{F}}\partial_x \end{bmatrix} \begin{bmatrix} \psi_{\mathrm{e}}(x) \\ \psi_{\mathrm{h}}(x) \end{bmatrix} = E \begin{bmatrix} \psi_{\mathrm{e}}(x) \\ \psi_{\mathrm{h}}(x) \end{bmatrix} \tag{2.66}$$

where $\Delta = \Delta_0 e^{i\phi_{\mathrm{R}}/2}\Theta(x)$, with the superconducting phase parameter ϕ_{R} and the Heaviside step function $\Theta(x)$. The wavefunctions will be of the form

$$\Psi(x < 0) = \begin{bmatrix} e^{iEx/\hbar v_{\mathrm{F}}} \\ r_{\mathrm{A}} e^{-iEx/\hbar v_{\mathrm{F}}} \end{bmatrix}, \tag{2.67a}$$

$$\Psi(x > 0) = \begin{bmatrix} f_{\mathrm{e}} \\ f_{\mathrm{h}} \end{bmatrix} C e^{-x\sqrt{|\Delta|^2 - E^2}/\hbar v_{\mathrm{F}}}. \tag{2.67b}$$

where C is an arbitrary constant, r_{A} is the amplitude associated with Andreev reflection, and f_{e} and f_{h} are constants which, as a result of normalisation, must satisfy

$$|f_{\mathrm{e}}|^2 + |f_{\mathrm{h}}|^2 = 1. \tag{2.68}$$

From the hole-like component of Eq. (2.67b), it follows that

$$f_{\mathrm{h}} = \frac{1}{\Delta}\left(E - i\sqrt{|\Delta|^2 - E^2}\right) f_{\mathrm{e}} \tag{2.69}$$

and, by matching the electron-like component at $x = 0$, it must be that

$$r_{\mathrm{A}} = \alpha e^{-i\phi_{\mathrm{R}}/2} \tag{2.70}$$

where

$$\alpha = e^{-i\arccos(E/\Delta_0)} \tag{2.71}$$

has unit modulus. Hence $|r_{\mathrm{A}}| = 1$ for subgap energies in the Andreev approximation, meaning that the sole scattering process undertaken by the electron is Andreev reflection. A similar result holds for the case of an incoming hole.

In terms of scatterers with energies above the gap ($E > \Delta$), the setup is the same except for the wavefunction on the superconducting side which ceases to be evanescent and is transmitted through with an amplitude t,

$$\Psi\left(x > 0\right) = \begin{bmatrix} f_{\mathrm{e}} \\ f_{\mathrm{h}} \end{bmatrix} \frac{t}{\sqrt{|f_{\mathrm{e}}|^2 - |f_{\mathrm{h}}|^2}} e^{ix\sqrt{E^2-\Delta^2}/\hbar v_{\mathrm{F}}}. \tag{2.72}$$

Solution of the Bogoliubov–de Gennes equations leads to the following expressions for the amplitudes

$$r_{\mathrm{A}} = \tilde{\alpha} e^{-i\phi_R/2}, \quad t = \sqrt{1 - \tilde{\alpha}^2}, \tag{2.73}$$

where

$$\tilde{\alpha} = e^{-\operatorname{arcosh}(E/\Delta_0)}, \tag{2.74}$$

such that $0 < |r_{\mathrm{A}}| < 1$. Therefore, Andreev reflection is no longer a certainty and transmittance into the superconducting leads is possible for scatterers above the gap [45].

Moreover, for above-the-gap scatterers, quasiparticles emanating from the superconductor can scatter at the interface and the calculation of their transmission and reflection amplitudes follows similarly to the above. For further detail, see Appendix C.2 for analogous calculations in a more general setup.

2.4 Andreev bound states in an s-wave Josephson junction

A straightforward extension to normal–superconductor interfaces is the composite structure formed of two superconducting leads interposed by a short normal region—the *superconductor–normal-metal–superconductor (SNS) Josephson junction*. Such systems are of interest as electrons and holes in the normal region with energies less than the gap parameter of either superconductor are unable to indefinitely extend into the superconducting leads so that they, in the Andreev approximation, must continuously undergo Andreev reflections at each normal–superconductor interface. This results in the formation of *Andreev bound states* which, in principle, enable a finite current to flow across the junction.

Accordingly, we review an analysis of quasi-one-dimensional junctions with time-reversal symmetry between s-wave superconductors, as was originally treated by Beenakker in Ref. [15], where it will emerge that the bound state spectrum is critical in the determination of the current flowing across the junction. Moreover, such a system provides a convenient example to employ the ideas introduced earlier in this chapter; the core of this time-reversal-invariant technique will again be utilised in Chapter 3, where the analysis is extended in the single-channel case to include asymmetric junctions involving topological superconductors.

The general scattering picture is depicted in Fig. 2.4, where it is convenient to con-

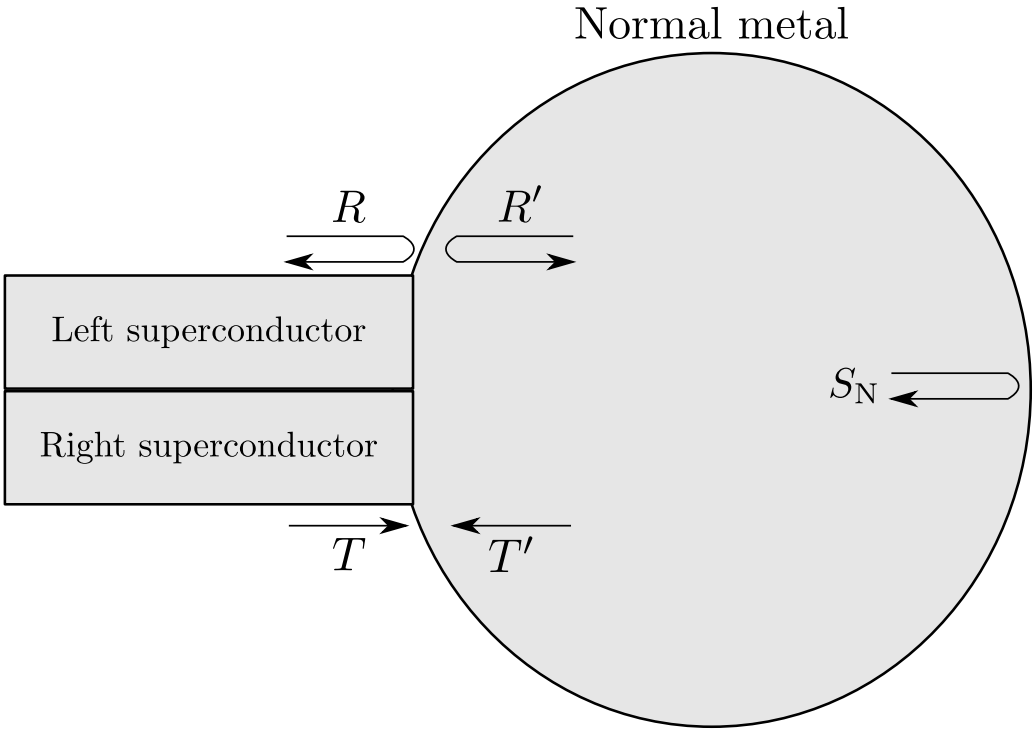

Figure 2.4: The scattering processes that may occur in a quasi-one-dimensional Josephson junction. The system is comprised of two superconducting leads which are bridged together by a short normal region. The reflection and transmission for particles impinging on the normal–superconductor interface are given by R and T for those particles originating from deep within the superconductor and R' and T' for those coming from within the normal region, while scattering in the normal region is described by the matrix S_{N}.

ceptualise the system as having its superconducting leads to the left and the normal region to the right. The general scattering processes at the normal–superconductor interfaces are described by matrices of reflection R and R' and matrices of transmission T and T', where the prime's absence indicates that the scatterers emanate from deep within the superconducting leads and its presence means that the scatterers come from the normal region, and scattering which occurs at the normal region is described by S_{N}. Considering a system with N channels, each of these matrices is of size $4N \times 4N$, and may be considered in terms of an electron-hole grading to be formed of blocks of size $2N \times 2N$, which are further subdivided into blocks of size $N \times N$ according to the left and right leads.

2.4.1 Scattering matrix of the normal region

The scattering matrix of the normal region is given by

$$S_{\mathrm{N}} = \begin{bmatrix} S_{\mathrm{e}}(E) & 0 \\ 0 & S_{\mathrm{h}}(E) \end{bmatrix}, \tag{2.75}$$

where the condition $S_{\mathrm{h}}(E) = S_{\mathrm{e}}(-E)^*$ is enforced as a result of particle-hole symmetry. Owing to the s-wave superconductivity and the spin-rotation invariance, the effect of time-reversal symmetry on S_N reduces to the the condition that $S_{\mathrm{N}} = S_{\mathrm{N}}^{\mathsf{T}}$.

By considering short junctions, where the length of the normal region is much shorter than the superconducting coherence length, we assume that particles pass through the junction very quickly so that $\tau_{\mathrm{dw}}\Delta_0 \ll \hbar$ holds, where τ_{dw} is the typical time taken to traverse the junction and Δ_0 is the magnitude of the superconducting gap. As the blocks of the scattering matrix can only change appreciably if E is changed by at least $\hbar/\tau_{\mathrm{dwell}}$, and we are only concerned with energies on the order of Δ_0, this allows one, to a good approximation, to neglect the energy dependence of S_{N} so that $S_{\mathrm{e}}(E) \approx S_{\mathrm{e}}(0)$ [15, 45].

2.4.2 Scattering below the superconducting gap

We consider a system where both superconductors have an s-wave pairing with gap parameters $\Delta_{\mathrm{L}} = \Delta_0 e^{-i\phi/2}$ and $\Delta_{\mathrm{R}} = \Delta_0 e^{i\phi/2}$. In terms of the subgap scatterers (i.e. those with energy $|E| < \Delta_0$), the matrices R, T, and T' are null as the particles are unable to indefinitely extend into either superconductor. The Andreev reflections are described by the matrix

$$R' = \begin{bmatrix} 0 & r_{\mathrm{eh}} \\ r_{\mathrm{he}} & 0 \end{bmatrix} \tag{2.76}$$

where the blocks may be written in relation to the Andreev reflection amplitudes as in Eq. (2.70), so that

$$r_{\mathrm{eh}} = \alpha\left(E\right) r_{\mathrm{A}}, \quad r_{\mathrm{he}} = \alpha\left(E\right) r_{\mathrm{A}}^{*}, \tag{2.77}$$

with $\alpha\left(E\right)$ as specified in Eq. (2.71) and

$$r_{\mathrm{A}} = \begin{bmatrix} e^{-i\phi/2}\mathbb{1}_{N} & 0 \\ 0 & e^{i\phi/2}\mathbb{1}_{N} \end{bmatrix}. \tag{2.78}$$

[The absence of normal reflections in Eq. (2.76) is due to working within the Andreev approximation.]

The motion of subgap scatterers inside the junction is fully described by the two matrices S_{N} and r_{A}. In regard to the modes impinging on the normal region (described by the vector of coefficients $\mathbf{c}_{\mathrm{N}}$) and those on the superconductor-normal interfaces (described by the vector of coefficients $\mathbf{c}_{\mathrm{S}}$), we have that

$$\begin{aligned} \mathbf{c}_{\mathrm{S}} &= S_{\mathrm{N}}\mathbf{c}_{\mathrm{N}} \\ &= S_{\mathrm{N}}R'\mathbf{c}_{\mathrm{S}}, \end{aligned} \tag{2.79}$$

which allows for the formulation of the secular equation

$$\det\left(\mathbb{1}_{4N} - S_{\mathrm{N}}R'\right) = 0, \tag{2.80}$$

from which the Andreev bound state energies may be derived. The secular equation is simplified by writing it as a product

$$\det\begin{bmatrix} \mathbb{1}_{2\mathrm{N}} & 0 \\ -S_{\mathrm{h}}r_{\mathrm{he}} & \mathbb{1}_{2\mathrm{N}} \end{bmatrix} \det\begin{bmatrix} \mathbb{1}_{2\mathrm{N}} & -S_{\mathrm{e}}r_{\mathrm{eh}} \\ 0 & \mathbb{1}_{2\mathrm{N}} - S_{\mathrm{h}}r_{\mathrm{he}}S_{\mathrm{e}}r_{\mathrm{eh}} \end{bmatrix} = 0, \tag{2.81}$$

which, along with the conditions imposed by particle-hole symmetry and time-reversal

symmetry, further simplifies to

$$\det\left(S_{\mathrm{e}} - r_{\mathrm{he}} S_{\mathrm{e}} r_{\mathrm{eh}}\right) = 0. \tag{2.82}$$

As a result of the unitarity of S_{e} and the singular-value decomposition of its blocks, S_{e} has the so-called polar decomposition

$$S_{\mathrm{e}} = \begin{bmatrix} U & 0 \\ 0 & V \end{bmatrix} \begin{bmatrix} -\sqrt{\mathbb{1}_N - \hat{\tau}} & \sqrt{\hat{\tau}} \\ \sqrt{\hat{\tau}} & \sqrt{\mathbb{1}_N - \hat{\tau}} \end{bmatrix} \begin{bmatrix} U' & 0 \\ 0 & V' \end{bmatrix}, \tag{2.83}$$

where the submatrices U, V, U', and V' are unitary and $\hat{\tau}$ is a diagonal matrix whose elements are the transmission eigenvalues $0 \leq \tau_p \leq 1$ of each channel p [46, 47]. By means of the same folding trick used in Eq. (2.81), the secular equation can be written as

$$Z_1 \det\left[\left(1-\alpha^2\right)\sqrt{\mathbb{1}_N - \hat{\tau}} + \frac{\left(1-\alpha^2 e^{i\phi}\right)\left(1-\alpha^2 e^{-i\phi}\right)\hat{\tau}}{\left(1-\alpha^2\right)\sqrt{\mathbb{1}_N - \hat{\tau}}}\right] Z_2 = 0 \tag{2.84}$$

where

$$Z_1 = \det\left[-\left(1-\alpha^2\right) U \sqrt{\mathbb{1}_N - \hat{\tau}} U' V\right], \quad Z_2 = \det\left(V'\right). \tag{2.85}$$

Provided that there are no perfectly transparent channels, this expression simplifies further to

$$\det\left[\left(1 - \frac{E_p^2}{\Delta_0^2}\right)\mathbb{1}_N - \hat{\tau}\sin\left(\frac{\phi}{2}\right)^2\right] = 0, \tag{2.86}$$

which yields the Andreev bound state energies for each channel p

$$E_p = \Delta_0 \sqrt{1 - \tau_p \sin^2\left(\frac{\phi}{2}\right)}. \tag{2.87}$$

Therefore, for a time-varying phase difference $\phi(t)$ which may be provided by a voltage

V through $\dot{\phi}(t) = 2eV/\hbar$, there is an associated current per channel

$$I_p = -\frac{2e}{\hbar}\frac{\partial E_p}{\partial \phi} \tag{2.88}$$

that flows across the junction at zero temperature as a result of the phase difference between the two superconductors.

2.4.3 Scattering above the superconducting gap

For scatterers with an energy magnitude above the gap, one must take into account the total scattering matrix of the junction S_{SNS} which has a structure dependent on the reflection matrices R and R', the transmission matrices T and T', and the normal scattering matrix S_{N}. The reflection matrices take the form

$$-R = R' = \tilde{\alpha}(E) \begin{bmatrix} 0 & r_{\mathrm{A}} \\ r_{\mathrm{A}}^* & 0 \end{bmatrix} \tag{2.89}$$

and the transmission matrices are

$$T = T' = \sqrt{1 - \tilde{\alpha}^2(E)}\mathbb{1}_{4N}, \tag{2.90}$$

where $\tilde{\alpha}(E)$ is of the form as presented in Eq. (2.74). S_{SNS} is then constructed by considering incoming scatterers emanating from the superconducting leads and writing down every possible scattering process that can occur within the junction,

$$S_{\mathrm{SNS}} = R + TS_{\mathrm{N}}T' + TS_{\mathrm{N}}R'S_{\mathrm{N}}T' + TS_{\mathrm{N}}R'S_{\mathrm{N}}R'S_{\mathrm{N}}T' + \ldots, \tag{2.91}$$

which forms a series whose sum is

$$S_{\mathrm{SNS}} = R + T\left(\mathbb{1}_{4N} - S_{\mathrm{N}}R'\right)^{-1} S_{\mathrm{N}}T'. \tag{2.92}$$

By using the unitarity of S_{N} and the Hermiticity of the reflection and transmission matrices, along with the relations

$$\frac{R^2}{\tilde{\alpha}^2} = \frac{T^2}{1-\tilde{\alpha}^2} = \mathbb{1}_{4N}, \tag{2.93}$$

the scattering matrix of the junction can be written as

$$S_{\mathrm{SNS}} = \left(\mathbb{1}_{4N} - S_{\mathrm{N}}R'\right)^{-1}\left[\mathbb{1}_{4N} - \left(S_{\mathrm{N}}R'\right)^{\dagger}\right] S_{\mathrm{N}}. \tag{2.94}$$

Moreover, the phase-dependent contribution to the density of states ρ is given by [48]

$$\rho = \frac{1}{i2\pi}\frac{\partial}{\partial E}\ln\det S_{\mathrm{SNS}} \tag{2.95}$$

and the associated current in the zero-temperature limit is

$$I_{\mathrm{c}} = -\frac{2e}{\hbar}\int_{\Delta}^{\infty} \mathrm{d}E\, E\, \frac{\mathrm{d}\rho}{\mathrm{d}\phi}\,. \tag{2.96}$$

However, by use of the expression for S_{SNS} in Eq. (2.94), the phase derivative of ρ is

$$\frac{\partial\rho}{\partial\phi} = -\frac{1}{\pi}\frac{\partial^2}{\partial\phi\partial E}\,\mathrm{Im}\ln\det\left(\mathbb{1}_{4N} - S_{\mathrm{N}}R'\right). \tag{2.97}$$

Note that, by using a decomposition of the form in Eq. (2.81), the determinant may be rewritten as

$$\begin{aligned}\det\left(\mathbb{1}_{2N} - \tilde{\alpha}S_{\mathrm{e}}^{*}r_{\mathrm{A}}^{*}\tilde{\alpha}S_{\mathrm{e}}r_{\mathrm{A}}\right) &= \det\left(\tilde{\alpha}S_{\mathrm{e}}^{*}r_{\mathrm{A}}^{*}\right)^{-1}\det\left(\mathbb{1}_{2N} - \tilde{\alpha}S_{\mathrm{e}}^{*}r_{\mathrm{A}}^{*}\tilde{\alpha}S_{\mathrm{e}}r_{\mathrm{A}}\right)\det\left(\tilde{\alpha}S_{\mathrm{e}}^{*}r_{\mathrm{A}}^{*}\right)\\ &= \det\left(\mathbb{1}_{2N} - \tilde{\alpha}S_{\mathrm{e}}^{*}r_{\mathrm{A}}^{*}\tilde{\alpha}S_{\mathrm{e}}r_{\mathrm{A}}\right)^{*},\end{aligned} \tag{2.98}$$

from which it follows that $\det\left(\mathbb{1}_{4N} - S_{\mathrm{N}}R'\right)$ is real. Hence, in the short-junction limit, scatterers with energies above the superconducting gap do not contribute to the current that flows across the junction.

Therefore, the Josephson current is solely due to energies in the subgap spectrum. Had topological superconductors been under consideration, one might wonder if a similar setup would yield interesting results: Majorana zero modes at the junction form part of the subgap spectrum, and, if the contributions to the current from the continuum are negligible, then readouts of the current may provide a clear window to view features associated with the inherent topological symmetries. However, even in the s-wave case, it turns out that contributions from the continuum are only zero in the case of gap-symmetric junctions [49]. A more careful examination of topological junctions is thus necessary, taking into account possible gap asymmetries and the different contributions to the Josephson current. Such an analysis is provided for single-channel junctions in Chapter 3.

2.5 Summary

Over the course of this chapter, two concepts have been introduced and employed: time-reversal symmetry and the scattering matrix approach to mesoscopic transport. In the case of the former, we have seen the constraints that time-reversal symmetry places upon the Hamiltonian and one of its primary consequences: Kramers' degeneracy theorem. With regard to the latter, the scattering formalism and the Bogoliubov–de Gennes description allow for transport through mesoscopic structures to be understood in terms of scattering matrices. The confluence of these two ideas takes place in the Josephson junction between gap-symmetric s-wave superconductors, where it emerged, in the short-junction limit, that the current flowing across the junction depends upon only the Andreev bound states that reside within the junction. This hints that similar systems with non-trivial topology may be of interest, since any effects arising from the underlying Majorana zero modes could be observed in isolation.

These ideas, along with those explored in Chapter 1, provide a solid foundation upon which the original work of this thesis can be conducted. While this chapter largely avoided

the discussion of the Majorana zero mode motivated in the previous chapter, the remainder of this thesis will be concerned with the effects of Kramers pairs of Majorana modes in Josephson junctions. Restricting our analysis to single-channel junctions, the time-reversal-invariant junction between s-wave superconductors is effectively extended to an approach which incorporates gap asymmetries and allows for topological superconductors. As in the strictly s-wave case, such a theory allows for predictions of the Josephson current relative to a small number of experimentally accessible parameters.

Chapter 3

Signatures of time-reversal-invariant topological superconductivity in the Josephson effect

As a preface to this chapter, it should be noted that the work contained within is essentially a reformatted version of Ref. [1] of the Publications section. The author of this thesis originally drafted this publication, carrying out the bulk of the calculations which appear outside of Sec. 3.6 and additionally running the code described in Sec. 3.6, part of which involved a fitting procedure, to produce the numerical lattice data showcased in Figs. 3.2–3.5. Dr. Benjamin Béri coauthored this paper, providing invaluable guidance and direction overall with the calculations and the preparation of this manuscript and also performing the calculations and writing the code associated with the lattice model in Sec. 3.6.

3.1 Introduction

Josephson junctions involving Majorana fermions [6, 8–10] are under intensive theoretical [50–63] and experimental [64–68] investigation for the promising routes they provide towards demonstrating topological superconductivity [7–9, 69] and as potential building

blocks towards topological quantum computation [9–12]. In the most frequently studied class of systems, Majorana fermions are nondegenerate zero-energy end states in hybrid devices realising one-dimensional (1D) effectively spinless p-wave superconductors [6, 50, 70–74]. A number of concrete platforms exist to realise this time-reversal symmetry breaking (so-called class D [75]) topological superconductivity, all of which use the proximity effect to combine s-wave superconductors, strong spin-orbit coupling (e.g., via nanowires [70, 71], topological insulators [50], or the superconductor itself [72–74]) and magnetic fields (e.g., via Zeeman coupling [70, 71, 76] or ferromagnetism [50, 72–74]).

The past years have seen a rapidly increasing interest in realising [56, 77–86] and detecting [56–59, 62, 87, 88] time-reversal invariant (so-called class DIII [75]) analogues of such Majorana fermion systems. In 1D, class DIII topological superconductors host a Kramers pair of Majorana fermions at each end which can be combined into a zero-energy fermion end mode with anomalous time-reversal properties [69]. The proposed platforms for realisation again include hybrid devices based on spin-orbit coupling [56, 62, 79, 81, 85] and the superconducting proximity effect [56, 62, 77, 78, 80], albeit now with unconventional (but nontopological) superconductors (e.g., iron-based superconductors with $s_{\pm}$-wave pairing [89–91]). These hybrids realise spinful effectively p-wave pairing with the admixture of a smaller s-wave pairing component.

In this chapter, we study Josephson junctions involving 1D class DIII topological superconductors. We obtain the energy spectrum and the consequent Josephson current in terms of the normal-state scattering properties, requiring only that the junction be much shorter than the superconducting coherence length (i.e. the short-junction limit). Our results apply for a number of physically relevant situations including disordered junctions, or junctions of intermediate transparency that are away from both the tunnelling and the highly transparent limits considered in previous works [56–58].

We obtain results for two types of setups (Fig. 3.1): junctions between two topological superconductors [Fig. 3.1(a)] and junctions between an s-wave superconductor and a topological superconductor [Fig. 3.1(b)]. For the first type of setup [Fig. 3.1(a)], we study

the conditions under which a time-reversal invariant generalisation [56, 58] of the so-called fractional Josephson effect [6, 50, 51, 70, 71, 92, 93] can arise. This hallmark signature in class D topological superconductors refers to the appearance of a 4π periodic current-phase relation, replacing the more conventional 2π periodic one as Majorana fermions enable charge transfer in terms of electrons instead of Cooper pairs. In addition to establishing the form in which such behaviour can appear in class DIII topological Josephson junctions with generic junction properties, we also consider the role of the characteristic timescale for energy relaxation. The latter aspect, to the best of our knowledge, has not so far been considered; however, as we show, it presents an important channel for the loss of 4π periodicity.

For the second type of setup [Fig. 3.1(b)], we investigate how the anomalous time-reversal properties of the fermion f, built from the two interface Majoranas, appear in

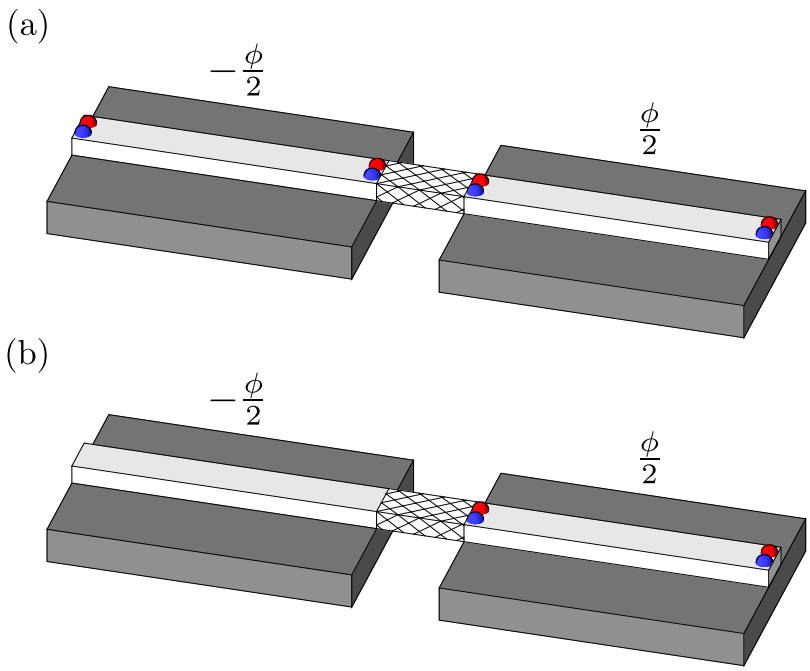

Figure 3.1: Majorana–Kramers setups for 1D Josephson junctions with a phase difference ϕ across the junction. The superconductors (dark grey slabs) each have a 1D, spin-orbit coupled quantum wire (light grey blocks) deposited on top of them. By the proximity effect, superconductivity is induced in each quantum wire. The wires with Majorana–Kramers pairs (red and blue hemispheres) display induced topological superconductivity, arising from coupling to unconventional (e.g., $s_{\pm}$-wave) superconductors. The normal region (e.g., tunnel barrier, point contact, disordered metal) between the superconductors is indicated by cross-hatching.

the features of the Josephson current. Here general considerations [57] show that there is an anomalous, time-reversal protected contribution that gives nonzero current at $\phi = n\pi$ (where n is integer) with sign set by the parity of f. To positively establish the origin of this contribution in an experimental system (e.g., that the current at $\phi = n\pi$ is not due to broken time-reversal invariance [92]), however, a theory for the current-phase relationship is needed that accounts for other, nonanomalous contributions and which holds for generic junctions. Such a theory may also be useful in scenarios where access to changes in ϕ are more readily available than to ϕ itself; for example, the AC Josephson effect where the phase sweep speed is controlled by the voltage across the junction (i.e. $\dot{\phi} = 2eV/\hbar$). In this chapter we provide such a theory.

The signatures mentioned above are for junctions with a conserved fermion parity. We also investigate, for both setups, the case where the fermion parity is allowed to relax (i.e. the DC Josephson effect regime). For all the regimes to be considered, we compare topological junctions to their nontopological counterparts (i.e. without Majorana fermions) in order to search for unique signatures of topological superconductivity.

The rest of this chapter is organised as follows. We start, in Sec. 3.2, by describing 1D class DIII topological superconductors in terms of the Bogoliubov–de Gennes Hamiltonian near the Fermi points. This will allow us, in Sec. 3.3, to obtain the Andreev reflection matrices of normal-topological superconductor interfaces, and thus to formulate a scattering matrix description for our systems. In Sec. 3.4 we investigate the bound state spectrum supported by topological–topological (Sec. 3.4.1) and s-wave–topological (Sec. 3.4.2) Josephson junctions. Then in Sec. 3.5 we calculate the Josephson currents for our junction setups and contrast the results to the corresponding nontopological cases. To test our scattering matrix predictions, in Sec 3.6, we compare our results to numerical simulations of a lattice model of time-reversal invariant Josephson junctions. Finally, in Sec. 3.7 we present our conclusions.

3.2 Hamiltonian description of topological superconductors

In mean field theory, the excitations of superconductor systems can be described in an effectively single-particle picture in terms of the so-called Bogoliubov–de Gennes Hamiltonian [94], which is a 2×2 matrix in electron-hole space

$$H_{\mathrm{BdG}} = \begin{pmatrix} h_{\mathrm{e}} & \Delta \\ \Delta^{\dagger} & h_{\mathrm{h}} \end{pmatrix}. \tag{3.1}$$

Here h_{e} and h_{h} are the single-particle Hamiltonians for electrons and holes, respectively, and Δ is the superconducting pair potential. Each of the blocks of Eq. (3.1) act on spin-1/2 electrons and we have $h_{\mathrm{h}} = -\mathcal{T} h_{\mathrm{e}} \mathcal{T}^{-1}$ where $\mathcal{T} = i\sigma_2 K$ is the operator for time-reversal with Pauli matrices σ_j acting in spin-space and complex conjugation operator K. This choice of h_{h} corresponds to a basis which makes spin-rotation properties manifest: in a spin-rotation symmetric system, all blocks of H_{BdG} are proportional to the identity matrix in spin-space.

A Josephson junction is composed of two superconductors linked together by a normal region with a phase difference ϕ across the junction. We will describe such junctions, with normal regions $|x| \leq \frac{l}{2}$, using the step-function model [95]

$$\Delta = \begin{cases} \Delta_{\mathrm{L}} e^{-i\frac{\phi}{2}} & x < -\frac{l}{2}, \\ 0 & |x| \leq \frac{l}{2}, \\ \Delta_{\mathrm{R}} e^{i\frac{\phi}{2}} & x > \frac{l}{2}. \end{cases} \tag{3.2}$$

To describe topological superconductors in our setups, we focus on the case where h_{e} describes a spinful system that is, at least in the superconductors and at the normal–superconductor interfaces, effectively 1D (e.g., the spin-orbit coupled nanowire in the hybrid proposals [58, 78]) with a single conducting channel. The two spin components give rise to two right-moving and two left-moving Fermi points. Class DIII topological superconductivity arises [56] when the spectrum acquires superconducting gaps $\Delta_{\pm}$ of

opposite signs at the two right-moving Fermi points. The gaps at the left-moving pair of Fermi points follow by time-reversal symmetry. For our purposes, it is sufficient to focus on the physics in the vicinity of the Fermi points. In this case, in addition to spin, h_{e} acquires a further 2×2 block structure for left- and right-movers. We have

$$h_{\mathrm{e/h}} = \pm i\hbar \, \mathrm{diag}\,(v_+, v_-, -v_-, -v_+)\, \partial_x, \tag{3.3a}$$

$$\Delta_o = \mathrm{diag}\,(\Delta_{+o}, \Delta_{-o}, \Delta_{-o}, \Delta_{+o})\,, \tag{3.3b}$$

where the entries are ordered from the rightmost to the leftmost Fermi point. In Eq. (3.3a), v_+ and v_- are the Fermi velocities where the upper sign refers to the electron Hamiltonian and the lower to the hole Hamiltonian. In Eq. (3.3b), $o = \mathrm{L}, \mathrm{R}$ refers to the left/right superconductor and, without loss of generality, we will take $\Delta_{+o} > 0$. Moreover, by parameterising the pairings as $\Delta_\pm = \Delta_s \pm \Delta_p$, the system can be viewed as having a time-reversal invariant p-wave pairing Δ_p with the admixture of a smaller s-wave pairing Δ_s. In line with a number of concrete proposals describing systems conserving the z-component of spin, one can view $v_\pm$ as the right-/left-moving spin-$\uparrow$ velocities and $\Delta_\pm$ as the pairing at the corresponding Fermi points. (The complementary spin-$\downarrow$ quantities follow via time-reversal.) The Hamiltonian (3.3) is, however, more general and holds in the absence of a conserved spin component; it can be used to describe the superconductors in both setups we consider. For the topological–topological junction, we consider the gap-symmetric case $\Delta_{\mathrm{L}} = \Delta_{\mathrm{R}}$, while for the s-wave–topological junction we impose no such requirement.

3.3 Scattering matrix description of (topological) Josephson junctions

For nontopological, singlet superconductor based, Josephson junctions in the short-junction limit, time-reversal invariance is known to allow for elegant relations to the normal-state

scattering properties, [14–19] such as Beenakker's formula for s-wave junctions [15]

$$E = \sqrt{1 - \tau \sin^2(\phi/2)}, \tag{3.4}$$

expressing the Andreev (i.e. subgap) bound state energies in terms of the normal-state transmission probability τ at the Fermi energy. As we show below, a number of analogous exact relations exist in the topological case. The starting point for establishing these are the Andreev reflection matrices at normal (topological) superconductor interfaces.

3.3.1 Andreev reflection matrices for topological superconductors

Excitations with energies below the superconducting gap can be described in terms of Andreev reflections at the superconductor/normal (SN) interfaces. These Andreev reflections are described by the Andreev reflection matrices r_{eh} and r_{he}, which respectively contain amplitudes for a hole reflecting into an electron and vice versa.

We now use Eq. (3.3) as a starting point to derive the Andreev reflection matrices at SN interfaces, which will serve as key ingredients for formulating the scattering matrix description of our systems. The superconductors are 1D, forming single transport channels which carry electrons and holes of a particular spin, leading to four subchannels overall. The key assumption that we make is that the four electron-hole Dirac cones at the four Fermi points remain uncoupled for clean SN interfaces. This so-called Andreev approximation [44] holds when the superconducting coherence length is much longer than the inverse of the separation between neighbouring Fermi points or, when the bulk superconducting system conserves a spin component, between the left- and right-moving Fermi points.

The approach to deriving the Andreev reflection matrices is essentially the same as for the Josephson junction composed of s-wave superconductors, as treated by Beenakker

[15]. The Andreev reflection matrices take the form

$$r_{\mathrm{eh}} = \begin{bmatrix} \kappa_{1\mathrm{L}} & 0 \\ 0 & \kappa_{2\mathrm{R}} \end{bmatrix}, \quad r_{\mathrm{he}} = \begin{bmatrix} \kappa_{2\mathrm{L}} & 0 \\ 0 & \kappa_{1\mathrm{R}} \end{bmatrix}, \tag{3.5}$$

where we have introduced the subblocks

$$\kappa_{1o} = \begin{bmatrix} \alpha_{-o} & 0 \\ 0 & \alpha_{+o} \end{bmatrix} e^{-i\frac{\phi}{2}}, \quad \kappa_{2o} = \begin{bmatrix} \alpha_{+o} & 0 \\ 0 & \alpha_{-o} \end{bmatrix} e^{i\frac{\phi}{2}}, \tag{3.6}$$

with

$$\alpha_{\pm o} = e^{-i \arccos\left(E/\Delta_{\pm o}\right)}. \tag{3.7}$$

(Further details of the scattering calculation may be found in Appendix C.)

3.3.2 Normal-state scattering matrix and the energy spectrum

The scattering of electrons and holes about the normal region is described by the scattering matrices S_{e} and S_{h}, respectively. Together these matrices must obey certain symmetry relations as a result of the structure of the Hamiltonian (3.1). The first relation that must be satisfied as a consequence of particle-hole symmetry is

$$S_{\mathrm{h}}(E) = \mathcal{T} S_{\mathrm{e}}(-E) \mathcal{T}^{-1}. \tag{3.8}$$

The second relation that must be satisfied due to time-reversal invariance is

$$S_{\mathrm{e}}(E) = \sigma_2 S_{\mathrm{e}}^{\mathsf{T}}(E) \sigma_2. \tag{3.9}$$

The elements of $S_{\mathrm{e}}(E)$ change on the scale of $\hbar/t_{\mathrm{dw}}$, where t_{dw} is the dwell time in the junction. In terms of t_{dw} and Δ, the short-junction limit requires $\Delta \ll \hbar/t_{\mathrm{dw}}$. Since we will consider energies on the scale of a few Δ or less, the energy dependence of the scattering matrix $S_{\mathrm{e}}(E)$ may be neglected [15], allowing us to take the scattering matrix

at the Fermi level $S_{\mathrm{e}}(E) = S_{\mathrm{e}}(E=0)$.

The electron subblock of the scattering matrix has the general form

$$S_{\mathrm{e}} = \begin{bmatrix} r & t' \\ t & r' \end{bmatrix} \tag{3.10}$$

and, upon using time-reversal symmetry [Eq. (3.9)] in the single channel case of interest, we can parameterise [96]

$$r = \rho \mathbb{1}_2, \quad r' = \rho' \mathbb{1}_2, \quad t = \sigma_2 t'^{\mathsf{T}} \sigma_2 = \sqrt{\tau} U, \tag{3.11}$$

where ρ and ρ' are complex numbers. The transmission probability τ encodes the normal-state conductance as $G = \left(2e^2/h\right)\tau$. The spin-orbit scattering has been introduced through the 2×2 unitary matrix $U = \widetilde{U} e^{i\chi}$, where χ is a real phase and $\widetilde{U}$ is an SU(2) matrix which can be parameterised by Euler angles (θ, ω, η) via

$$\widetilde{U} = e^{-i\frac{\theta}{2}\sigma_3} e^{-i\frac{\omega}{2}\sigma_2} e^{-i\frac{\eta}{2}\sigma_3}, \tag{3.12}$$

where the parameter ω is a measure of the degree of spin-flip scattering. Furthermore, due to the unitarity of S_{e}, we have the following identity

$$\rho\rho' = -e^{i2\chi}(1-\tau). \tag{3.13}$$

At this point, we are now ready to consider specific junction setups and how the Andreev energies may be obtained.

3.4 Andreev bound state spectrum

The scattering processes described in the previous section lead to Andreev bound states in the normal region of the Josephson junction, where the bound states have a spectrum

of energies dependent on ϕ. These energies are the roots of the secular equation [15]

$$\det\left[\mathbb{1}_4 - r_{\mathrm{he}}\left(E\right) S_{\mathrm{e}}\left(E\right) r_{\mathrm{eh}}\left(E\right) S_{\mathrm{h}}\left(E\right)\right] = 0, \tag{3.14}$$

where we have introduced $\mathbb{1}_4$ as the 4×4 identity matrix. We now turn to obtaining the Andreev levels by solving the secular equation for the junction setups depicted in Fig. 3.1(a) and Fig. 3.1(b).

3.4.1 Junction between topological superconductors

Here we work towards obtaining the spectrum of Andreev bound states in the topological–topological junction depicted in Fig. 3.1(a). For simplicity, we take the pairing strengths to be identical on either side of the junction, allowing us to suppress the o index for convenience.

By substituting the scattering matrix (3.10) and the Andreev reflection matrices (3.5) into the secular equation (3.14) and also employing Eq. (3.13), particle-hole symmetry and time-reversal symmetry in Eq. (3.8)-(3.9), and the folding identity

$$\det\begin{bmatrix} A & B \\ C & D \end{bmatrix} = \det\left(AD - ACA^{-1}B\right), \tag{3.15}$$

the secular equation may be recast into the form

$$\det\left[\left(1 - \tau - \mathrm{Re}\,\gamma\right)\mathbb{1}_2 + \frac{\tau}{2}\left(Ye^{-i\phi} + Y^{\dagger}e^{i\phi}\right)\right] = 0, \tag{3.16}$$

where we have used $\gamma = \alpha_{+}\alpha_{-}$, $Y = \tilde{\kappa}_1\widetilde{U}\tilde{\kappa}_1\widetilde{U}^{\dagger}$, and $\tilde{\kappa}_1 = e^{i\phi/2}\gamma^{-1/2}\kappa_1$. Since $Y \in \mathrm{SU}(2)$, we may rewrite Eq. (3.16) as

$$\det\left[\left(1 - \tau - \mathrm{Re}\,\gamma\right)\mathbb{1}_2 + \tau\,\mathrm{Re}\left(D_Y e^{i\phi}\right)\right] = 0, \tag{3.17}$$

where D_Y is the diagonal matrix of eigenvalues of Y. We now demonstrate that the only

relevant SU(2) parameter in Eq. (3.12) is ω. Directly substituting this parameterisation into Y, we find that

$$Y = e^{-i\frac{\theta}{2}\sigma_3}\left(\tilde{\kappa}_1 e^{-i\frac{\omega}{2}\sigma_2}\tilde{\kappa}_1 e^{i\frac{\omega}{2}\sigma_2}\right)e^{i\frac{\theta}{2}\sigma_3}, \tag{3.18}$$

so that the eigenvalues contained in D_Y are those of

$$Y' = \tilde{\kappa}_1 e^{-i\frac{\omega}{2}\sigma_2}\tilde{\kappa}_1 e^{i\frac{\omega}{2}\sigma_2} \tag{3.19}$$

and hence only the parameter ω plays a role.

Since the determinant in the secular equation (3.17) is of a diagonal matrix, the secular equation amounts to either one or both of two equations being satisfied. Introducing $E_\pm = E/\Delta_\pm$ and $x_\pm = 1 - z_\pm \cos^2(\omega/2)$, where

$$z_\pm = 1 - E_+E_- \pm \sqrt{1-E_+^2}\sqrt{1-E_-^2}, \tag{3.20}$$

the two equations are

$$z_- + \tau\left[x_+\cos(\phi) \pm \sqrt{1-x_+^2}\sin(\phi) - 1\right] = 0 \tag{3.21}$$

and these equations together can contribute up to four solutions to the Andreev spectrum.

3.4.1.1 Without s-wave pairing

If we consider the special case where $\Delta_+ = -\Delta_-$ (i.e. setting the s-wave admixture to zero), a compact expression may be obtained for the bound state energies

$$E = \pm'\Delta_+\sqrt{\tau}\cos\left(\frac{\phi \pm \omega}{2}\right), \tag{3.22}$$

where the $\pm'$ has a superscript prime in order to distinguish it from the $\pm$. Eq. (3.22) already illustrates the effect of the spin-orbit scattering: as it is varied, it translates half of

the Andreev levels to the left and the other half to the right in E-ϕ space. Furthermore, as a result of time-reversal symmetry, the branch crossings at $\phi = n\pi$, where n is an integer, are protected by Kramers' theorem. Eq. (3.22) is a result in line with a related system where the normal region is modelled as a tunnel barrier with a delta function potential [92].

3.4.1.2 The effect of an s-wave pairing component

For the case where $\Delta_+ \neq -\Delta_-$ (i.e. in the presence of an s-wave pairing admixture), the secular equation (3.17) may be solved analytically, but such an expression is cumbersome due to its size. It, however, displays a number of salient and robust features shared with the purely p-wave case. The first of these is the crossing of the energy branches at $\phi = n\pi$ (with n integer); as these are time-reversal invariant phases, this is simply a consequence of Kramers' theorem. A less obvious finding regards the zero crossings ϕ_n of the energies, defined by $E(\phi_n) = 0$. From the secular equation (3.17), we analytically extract the values of ϕ_n as

$$\phi_n = \pm\omega + (2n+1)\,\pi. \tag{3.23}$$

The locations of these zero crossings are identical to the case of a junction without s-wave pairing, as in Eq. (3.22), meaning that the inclusion of a weak s-wave pairing does not move or remove the zero crossings. As a result of this, the Andreev branches will remain 4π periodic in the presence of an s-wave pairing. (Strictly speaking, in the linear junctions we consider, the zero crossings and the consequent 4π periodicity are only approximate, neglecting the hybridisation with the Majorana–Kramers pairs at the far ends of the wires given its exponential suppression in system size. Exact zero crossings arise in a ring geometry when the only Majorana fermions in the system are in the junction.) The bound state energies for this junction display one of the electron-hole and time-reversal symmetry protected topological patterns proposed by Zhang and Kane [97] in the context

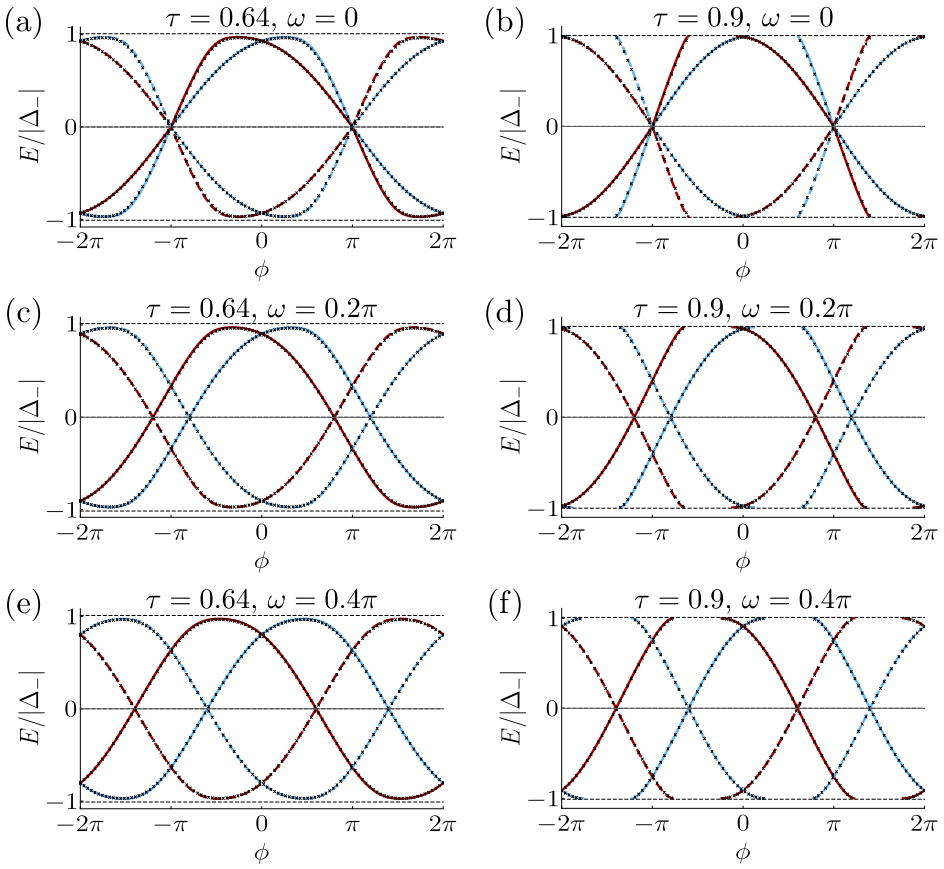

Figure 3.2: Andreev bound state energies for a Josephson junction between topological superconductors with a weak s-wave pairing ($\Delta_s < \Delta_p$) corresponding to $\Delta_+ = -2\Delta_-$. The transmission probability τ and spin-orbit parameter ω vary throughout. The transmission probability above which bound states are lost to the continuum is $\tau_c = 0.75$ [see Eq. (3.24)]. Here and in what follows, we express results in terms of the gap parameter with smallest magnitude and also show data (black crosses/dashed lines) from a numerical lattice simulation (see Sec. 3.6) of the corresponding junctions. The gaps in the simulations here are $\Delta_{0L} = \Delta_{0R} = -0.032$ and $\Delta_{1L} = \Delta_{1R} = 0.054$; their parameterisations in terms of $\Delta_\pm$ may be found in Eq. (3.45).

of anomalous topological pumps. Examples of the subgap energies are depicted in Fig. 3.2.

An important feature of the finite s-wave pairing admixture is the existence of an intergap energy regime ($-\Delta_- < |E| < \Delta_+$) where the subgap energies generally cannot exist. Branches which would appear to extend past Δ_- up towards Δ_+ vanish after hitting the Δ_- threshold [e.g., see Fig. 3.2(b)]. As these branches approach the threshold, their derivatives are found to smoothly tend to zero. The existence of an intergap regime has ramifications for the Josephson current and is discussed in Sec. 3.5.

Whether there are subgap branches which reach the Δ_- threshold is dependent only

on the magnitude of τ and the pairings $\Delta_{\pm}$. We find a critical transmission probability τ_{c} above which branches of the Andreev spectrum are lost to the intergap regime. It has the form

$$\tau_{\mathrm{c}} = \frac{\Delta_+ - \Delta_-}{2\Delta_+}. \tag{3.24}$$

An exception is the case of perfect transmission and a conserved z-component of spin (i.e. $\tau = 1$ and $\omega = 0$), where the Δ_+ and Δ_- modes are not mixed and hence the subgap energies are not lost to the continuum.

3.4.1.3 Nontopological variant

In the case where the s-wave admixture is stronger than the p-wave pairing (i.e. $\Delta_- > 0$), the superconductor is nontopological. From the secular equation (3.17), the Andreev energies for a nontopological junction are given by the solutions to the two equations

$$z_+ + \tau \left[x_- \cos(\phi) \pm \sqrt{1 - x_-^2} \sin(\phi) - 1 \right] = 0. \tag{3.25}$$

From this equation it may be demonstrated that, other than the exceptional case of $\tau = 1$, there are no zero-energy modes for nontopological junctions.

As a consequence of time-reversal symmetry, the Andreev levels must cross at phases $\phi = n\pi$. We also note that the spin-orbit parameter plays a role in splitting up the Andreev levels in ϕ-space; this is depicted for various values of ω in Fig. 3.3. These levels correspond to the trivial pump in terms of Ref. [97].

3.4.2 s-wave–topological superconductor junctions

We now investigate the Andreev bound state energies in the s-wave–topological superconductor setup, depicted in Fig. 3.1(b). Specifying that the s-wave superconductor is to the left of the topological superconductor, the Andreev reflection matrices are as in

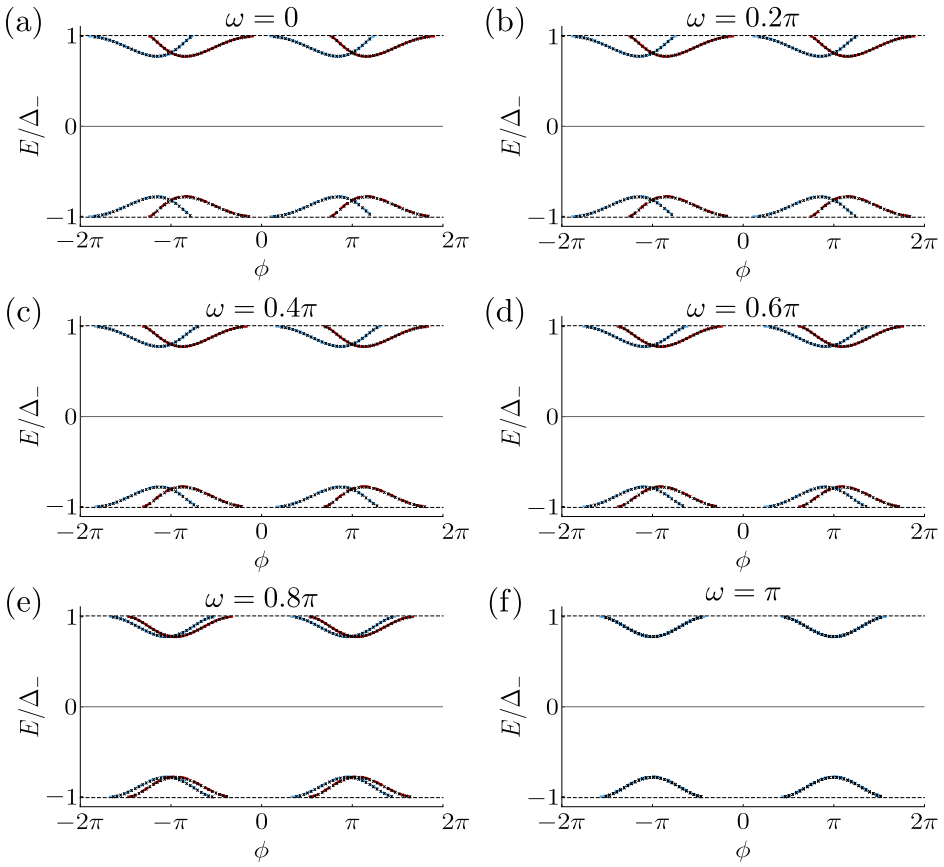

Figure 3.3: Andreev bound state energies for a Josephson junction between nontopological superconductors ($\Delta_s > \Delta_p$) corresponding to $\Delta_+ = 2\Delta_-$. The transmission probability is $\tau = 0.64$. The spin-orbit parameter ω is varied in (a)-(f), highlighting its role in splitting the levels in ϕ-space. Levels are lost to the continuum around $\phi = 0$ which is a generic feature when $\Delta_- \neq \Delta_+$. The numerical lattice data (black crosses/dashed lines) has gap parameters $\Delta_{0\mathrm{L}} = \Delta_{0\mathrm{R}} = 0.0027$ and $\Delta_{1\mathrm{L}} = \Delta_{1\mathrm{R}} = 0.018$.

Eqs. (3.5)–(3.7), where the gap parameters have the form

$$\Delta_{\pm\mathrm{L}} = \Delta_0 e^{-i\frac{\phi}{2}}, \quad \Delta_{\pm\mathrm{R}} = \Delta_\pm e^{i\frac{\phi}{2}}, \tag{3.26}$$

and we also take $\alpha_{\pm\mathrm{L}} = \alpha_0$ and $\alpha_{\pm\mathrm{R}} = \alpha_\pm$. Now by employing the parameterisation of the scattering matrix (3.10) and the folding identity (3.15), the secular equation (3.14) may be brought to the form

$$\det\left(\mathrm{Im}\,{\gamma_\mathrm{L}}^{\frac{1}{2}}\,\mathrm{Im}\,{\gamma_\mathrm{R}}^{\frac{1}{2}}\mathbb{1}_2 - \frac{\tau}{2}\,\mathrm{Re}\,\frac{{\gamma_\mathrm{L}}^{\frac{1}{2}}\mathbb{1}_2 - \kappa_{1\mathrm{R}}e^{-i\frac{\phi}{2}}}{{\gamma_\mathrm{R}}^{\frac{1}{2}}}\right) = 0, \tag{3.27}$$

where we have introduced $\gamma_{\mathrm{L}} = {\alpha_0}^2$ and $\gamma_{\mathrm{R}} = \alpha_- \alpha_+$ and the branch choice of the square root is irrelevant as long as the same choice is made for both γ_{L} and γ_{R}. Note here that the secular equation is already independent of the spin-orbit scattering. Furthermore, it may be demonstrated from this equation that the zero crossings occur when $\phi = n\pi$, where n is an integer. This is precisely the behaviour one expects as for these phases the junction realises a time-reversal invariant interface between a topological and a nontopological gapped system which must harbour a Kramers pair of Majorana zero modes. (The zero crossings, again, are strictly speaking approximate, neglecting the hybridisation with the Majorana–Kramers pairs at the far ends of the wire.)

3.4.2.1 No s-wave admixture

A number of interesting limiting cases exist where the subgap energies have a compact solution. If we first consider the gap-symmetric case (i.e. $\Delta_\pm = \pm\Delta_0$), the Andreev bound state energies have the analytical solution

$$E = \pm' \frac{\Delta_0}{\sqrt{2}} \sqrt{1 \pm \sqrt{1 - \tau^2 \sin^2(\phi)}}, \tag{3.28}$$

where two of the bound states are low energy (corresponding to the negative sign of $\pm$) and the other two are high energy (corresponding to the positive sign of $\pm$). This result is in accordance with some related models of this junction that use certain specific choices for the tunnel barrier potential [92, 98].

Another interesting limit is when the conventional superconductor is strong compared to the topological superconductor (i.e. $\Delta_0 \gg \Delta_+$), where the subgap energies are

$$E = \pm \frac{\tau}{2 - \tau} \Delta_+ \sin(\phi)\,. \tag{3.29}$$

In the converse case (i.e. $\Delta_+ \gg \Delta_0$), the subgap energies are independent of the trans-

mission probability, taking the form

$$E = \pm\Delta_0 \sin(\phi), \tag{3.30}$$

provided that $\tau > 0$. The τ-independence of the energies in this limit can be attributed to the fact that, for $\Delta_+ \gg \Delta_0$, on the effectively p-wave side, only $\alpha(E \to 0)$ is involved in the Andreev reflections which therefore become resonant [72, 99, 100].

In the absence of an s-wave admixture and also where the left and right superconducting gaps differ in magnitude (i.e. $\Delta_+ = -\Delta_- \neq \Delta_0$), an intergap regime opens up where it is possible for Andreev levels to escape into the continuum. This result is in agreement with Ioselevich *et al.* [60] and also explains why the high-energy solutions are absent in Eqs. (3.29) and (3.30).

3.4.2.2 Generic s-wave–topological junctions

Upon the inclusion of a small s-wave pairing component in the topological superconductor, we find that a second intergap regime ($-\Delta_- < |E| < \Delta_+$) opens up where the Andreev bound states are able to escape into the continuum. This second intergap regime is of the same type as in the case of topological–topological superconductor junctions in Sec. 3.4.1.2.

With both of these intergap regimes, there are three types of junction that are possible depending on the relative magnitudes of the superconducting gaps. In general, the intergap regime spans over the range of energies $\min\{\Delta_0, |\Delta_-|, \Delta_+\} < |E| < \max\{\Delta_0, |\Delta_-|, \Delta_+\}$.

We find that the feature of a pair of high-energy solutions and a pair of low-energy solutions that arose in the gap-symmetric case remains generally true in the gap-asymmetric case with one caveat: as the high-energy solutions would appear to extend up to the largest gap of the system, high-energy subgap states are generally lost to the continuum as the intergap regime always spans from the smallest gap parameter to the largest. Illustrative

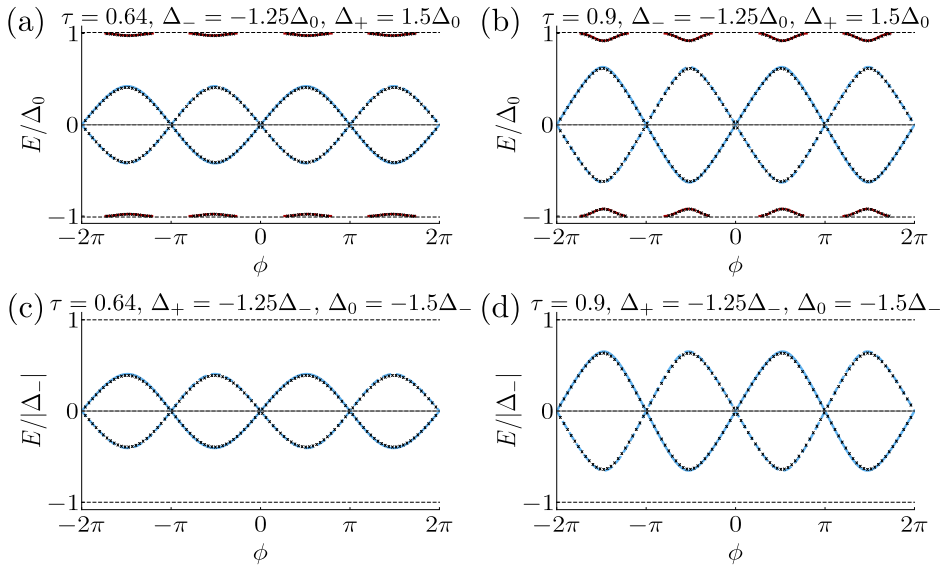

Figure 3.4: Andreev bound state energies for a Josephson junction between an s-wave superconductor (with gap Δ_0) and a topological superconductor (with gaps $\Delta_\pm$) with a finite s-wave pairing admixture. For (a) and (b) high-energy Andreev levels are generally present, while for (c) and (d) they are lost to the continuum for all phase differences ϕ. The numerical lattice data (black crosses/dashed lines) uses gap parameters $\{\Delta_{0\mathrm{L}}, \Delta_{1\mathrm{L}}, \Delta_{0\mathrm{R}}, \Delta_{1\mathrm{R}}\}$ with (a)-(b) $\{0.02, 0, -0.065, 0.099\}$ and (c)-(d) $\{0.03, 0, -0.053, 0.081\}$.

examples of the bound state spectrum are depicted in Fig. 3.4.

3.4.2.3 Nontopological variant

The system becomes nontopological when the s-wave admixture becomes greater than the p-wave pairing (i.e. $\Delta_- > 0$ in our convention). From the secular equation (3.27) it follows that, in this case, Andreev levels cross zero energy only in the exceptional case $\tau = 1$ at phase differences $\phi = (2n+1)\pi$ with n integer. The Majorana–Kramers pair at each $\phi = n\pi$ are now absent. Various nontopological subgap energies are depicted in Fig. 3.5.

3.5 Josephson current

The Josephson current I for our junctions comes from two contributions. One of these has been our focus so far: the Andreev bound state spectrum – states which are confined

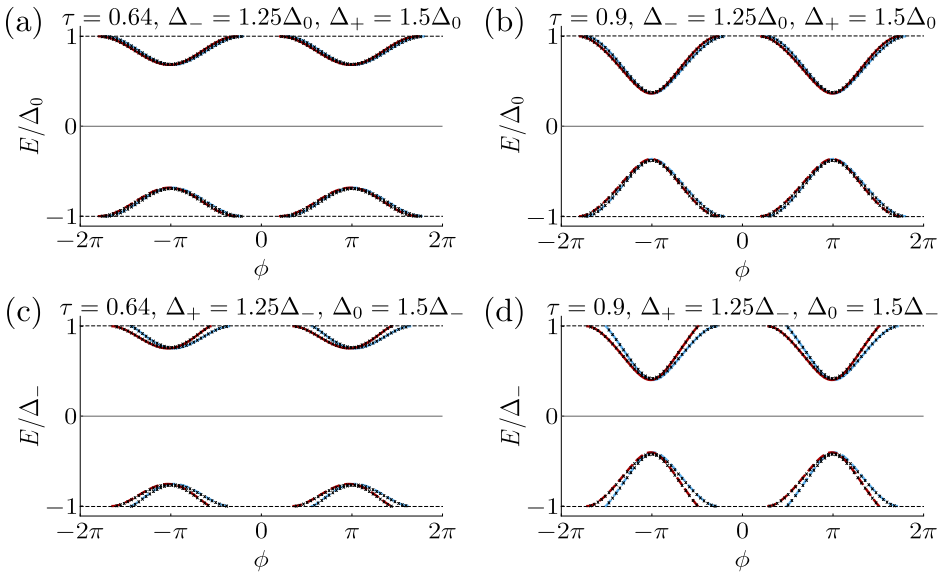

Figure 3.5: Andreev bound state energies for a Josephson junction between an s-wave superconductor with pairing Δ_0 and a nontopological superconductor with pairings Δ_+ and $\Delta_- > 0$. The numerical lattice data (black crosses/dashed lines) uses gap parameters $\{\Delta_{0\mathrm{L}}, \Delta_{1\mathrm{L}}, \Delta_{0\mathrm{R}}, \Delta_{1\mathrm{R}}\}$ with (a)-(b) $\{0.02, 0, 0.021, 0.009\}$ and (c)-(d) $\{0.03, 0, 0.016, 0.009\}$.

to the normal region of the Josephson junction. The other current contribution originates from the continuous spectrum – states with an energy larger than the smallest of the superconducting gaps, allowing them to extend into their respective superconductors. The total current is

$$I = I_{\mathrm{A}}(\phi) + I_{\mathrm{cont}}(\phi), \tag{3.31}$$

where I_{A} is the current due to the Andreev bound states and I_{cont} is the current due to the continuous spectrum. In what follows, for simplicity, we will consider the zero temperature limit and some related cases where the Bogoliubov–de Gennes energy levels have definite occupancies. (We will comment on finite temperature considerations in Sec. 3.7). In this case, each of the contributions can be calculated as

$$I_X(\phi) = \frac{2e}{\hbar}\frac{\mathrm{d}}{\mathrm{d}\phi}E_X(\phi), \qquad X = \mathrm{A},\ \mathrm{cont} \tag{3.32}$$

where $E_X(\phi)$ is the contribution of the part X of the spectrum to the total energy. We find, for both of our junction setups, that the contribution I_{cont} is zero for energies above the largest superconducting gap of the junction, while it is generally nonzero for energies that lie within an intergap regime. I_{A} is also generally nonzero for both of our topological junction setups.

The current that is measured depends on the speed at which ϕ changes relative to the energy and fermion parity relaxation times of the junction. In what follows, given that fermion parity relaxation often involves [50] energy relaxation but not necessarily vice versa, we consider three complementary cases: (i) when both energy and fermion parity relaxation can be neglected, (ii) with fast energy relaxation but fermion parity conservation, and (iii) when both energy and fermion parity relaxation are fast. In all cases, we use a protocol where the intended sweep is preceded by some period of slow sweep in regime (iii), which ensures definite Bogoliubov–de Gennes level occupancies. In addition to this, we assume the sweep speeds described in all cases are slow enough that unintended Landau-Zener tunnelling between branches or to the continuum is avoided.

Potential mechanisms for these relaxation processes are phonon or photon coupling in the case when parity is conserved and quasiparticle poisoning (e.g., from bulk localised [50]) when it is not. In terms of typical timescales for these processes, we assume that, depending on the relaxation regime one works in, the time taken to traverse a 4π period of the junction is either much faster or much slower than the relevant relaxation timescales. A recent experiment [101] on a Majorana-related mesoscopic superconductor system has been conducted working in the regime where the dominant relaxation respects fermion parity.

3.5.1 Junctions between topological superconductors

The contribution to the Josephson current by the Andreev levels is dependent on the fermion parity of the junction. As the Andreev levels come in particle-hole pairs, only half of them may be occupied at a given moment (due to the redundancy $c_E^\dagger = c_{-E}$ of

the corresponding fermion operators). If we associate one pair to have energy $\pm E_1(\phi)$ and the other pair to have energy $\pm E_2(\phi)$, where the Andreev levels are labelled as in Fig. 3.6(a), then the total energy from the Andreev levels is [102]

$$E_{\mathrm{A}}(\phi) = -\frac{1}{2}\left[(-1)^{n_1} E_1(\phi) + (-1)^{n_2} E_2(\phi)\right], \tag{3.33}$$

where $p = n_1 + n_2 \pmod 2$ is the fermion parity of the junction. In using the quantum numbers n_j, we neglect the hybridisation with the Majorana–Kramers pairs at the far ends of the wires as this is exponentially suppressed with system size. (This approximation influences only the parity conserving cases discussed below, where it amounts to assuming that ϕ changes quickly enough so that Landau-Zener tunnelling occurs with probability unity across the exponentially small splittings that the zero crossings approximate.) The concrete choice of n_j, as ϕ is varied, will depend on the junction's interaction with its environment, specifically on whether the junction is able to relax to the ground state (potentially subject to a parity constraint). We will separately discuss each of these cases in what follows.

3.5.1.1 Subgap current in the absence of relaxation

We consider the possible energies and currents in the absence of energy relaxation and, additionally for Landau-Zener tunnelling to the continuum to be in principle avoidable, with no levels escaping into the continuum. We have four branches of energy for the four values of $\{n_1, n_2\}$, each of which is 4π periodic in ϕ. This is illustrated in Fig. 3.6(b). The consequent current contribution is also 4π periodic.

3.5.1.2 Subgap current in the presence of energy relaxation

We now consider the subgap energy and its contribution to the current when the energy relaxation is much faster than the sweep speed of ϕ. This amounts to choosing the minimum energy $E_{\mathrm{A}}(\phi)$ within a given parity sector, resulting in branch switches at the

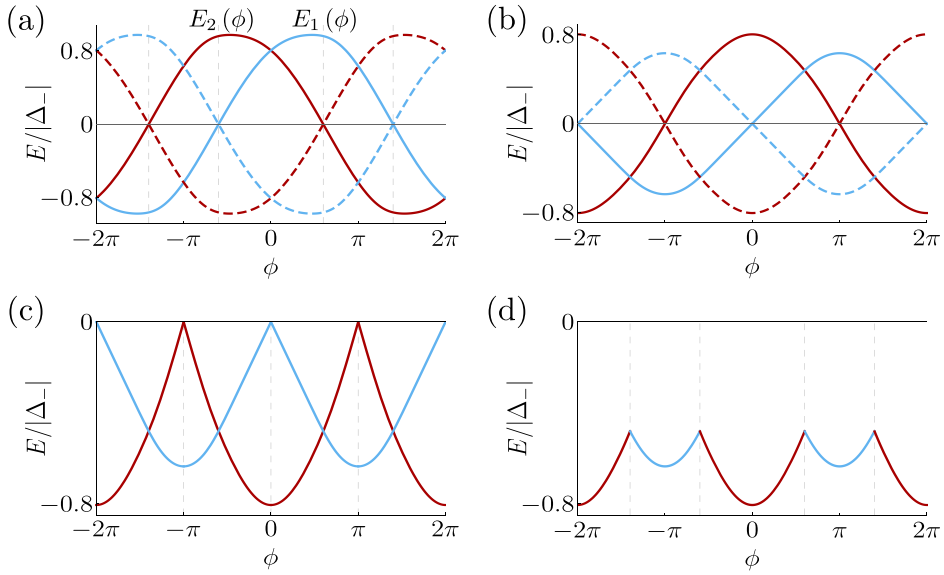

Figure 3.6: The subgap energies for a Josephson junction between topological superconductors. The superconductor pairing is $\Delta_+ = -2\Delta_-$, while the transmission probability and spin-orbit parameter are $\tau = 0.64$ and $\omega = 0.4\pi$. In (a) the blue and red curves represent $E_1(\phi)$ and $E_2(\phi)$, respectively [as in Eq. (3.33)], while the dashed lines signify their particle-hole partners. In (b)-(d), the blue lines are odd parity, the red lines are even parity energies. Fermion parity is conserved in (b) and (c), but not in (d). Energy relaxation is absent in (b), but not in (c) and (d). Numerical lattice data has been omitted as the agreement has already been demonstrated to be excellent.

locations $\phi = (p + 2n + 1)\pi$. These locations correspond to those of finite energy Andreev branch crossings which are where energy-minimising Andreev branch occupancy switches can occur without a change in fermion parity. Examples are depicted in Fig. 3.6(c). The corresponding current contribution is 2π periodic and has jumps ("current switches") at the branch switch locations.

3.5.1.3 Subgap current without fermion parity conservation.

Finally we consider the case where the junction relaxes to its ground state without conserving fermion parity. In this case the junction takes the minimum energy regardless of fermion parity, resulting in energy branch switches at the locations specified by Eq. (3.23). Underlying the switches are now the zero-energy Andreev branch crossings which, via changing the fermion parity, ensure that all of the negative energy Andreev levels are occupied for all ϕ. Such switches are indicative of the topological pattern of subgap branches

of Ref. [97]. Examples are shown in Fig. 3.6(d). The energies and the corresponding current contribution are 2π periodic. The branch switches, again, are accompanied by switches in the current contribution. These current switches are the class DIII analogues of the switches in class D systems, discussed in Ref. [61].

3.5.1.4 Continuous contributions to the Josephson current

In Sec. 3.4.1, we identified the energy regime $|E| > |\Delta_-|$ as where the spectrum is continuous. The Josephson current due to this spectrum will depend on the density of states ρ, whose structure is dependent on whether the energy is in the intergap regime $|\Delta_-| < |E| < \Delta_+$ or the above gap regime $|E| > \Delta_+$. Such a supercurrent may be calculated according to Eq. (3.32) and noting that the contribution of the filled negative energy Bogoliubov–de Gennes energy levels is $\frac{1}{2}\sum_{E_j<0} E_j$, [102]

$$I_{\text{cont}} = \frac{e}{\hbar}\int_{-\infty}^{-|\Delta_-|} \mathrm{d}E\, E\frac{\partial \rho}{\partial \phi}, \tag{3.34}$$

where ρ may be expressed in terms of the total scattering matrix of the junction S_{SNS}, [48]

$$\rho = \frac{1}{2\pi i}\frac{\partial}{\partial E}\ln\left[\det\left(S_{\text{SNS}}\right)\right] + \text{constant}. \tag{3.35}$$

The matrix S_{SNS} has the general form

$$S_{\text{SNS}} = \hat{R} + \hat{T}'\left(\mathbb{1} - S_{\text{N}}\hat{R}'\right)^{-1} S_{\text{N}}\hat{T}, \tag{3.36}$$

with $\hat{R}$ and $\hat{T}$ describing reflection and transmission for modes incoming from within the superconductor at the SN interface, $\hat{R}'$ and $\hat{T}'$ describing reflection and transmission for modes incoming from the normal region at the SN interface, and $S_{\text{N}} = \text{diag}\left(S_{\text{e}}, S_{\text{h}}\right)$ describing scattering off the normal region.

(a) Above the gaps. In the above the gap regime ($|E| > \Delta_+$), we demonstrate that

there are no continuous contributions to the Josephson current. The matrix $\hat{R}'$ has the general form

$$\hat{R}' = \begin{bmatrix} 0 & r_{\mathrm{eh}} \\ r_{\mathrm{he}} & 0 \end{bmatrix}, \tag{3.37}$$

where r_{eh} and r_{he} are the 4×4 matrices from Eq. (3.5) evaluated for $|E| > \Delta_+$. The other three scattering matrices are related via

$$\hat{R} = -\sigma_1 \hat{R}' \sigma_1, \quad \hat{T}' = \sqrt{\mathbb{1}_8 + \hat{R}\hat{R}'}, \quad \hat{T} = \sigma_1 \hat{T}' \sigma_1, \tag{3.38}$$

(Further details regarding the scattering may be found in Appendix C.) By using the relations in Eq. (3.38) in the expression for S_{SNS} (3.36), it may be shown, with some algebra, that

$$S_{\mathrm{SNS}} = \hat{T}' \left(\mathbb{1}_8 - S_{\mathrm{N}} \hat{R}' \right)^{-1} \left(S_{\mathrm{N}} \sigma_1 - \sigma_1 \hat{R}' \right) \hat{T}'^{-1} \sigma_1. \tag{3.39}$$

Then, using that $\alpha_\pm$ are real for energies above the gaps and substituting Eq. (3.39) into the density of states (3.35), we find that

$$\rho = -\frac{1}{\pi} \frac{\partial}{\partial E} \operatorname{Im} \ln \det \left(\mathbb{1}_4 + a a^* \right) + \text{constant}, \tag{3.40}$$

where $a = S_{\mathrm{e}}^* \sigma_2 r_{\mathrm{he}}$. It follows that $\det \left(\mathbb{1}_4 + a a^* \right)$ is real and hence the density of states (3.40) is constant. Therefore, there is no contribution to the Josephson current in the above the gap regime.

(b) Between the gaps. For energies in the intergap regime ($|\Delta_-| < |E| < \Delta_+$) we show that there are nonvanishing contributions to the Josephson current. The matrix $\hat{R}'$ has the same form as in Eq. (3.37); however, the rest of the matrices which describe scattering at the SN interface have reduced dimension since the Δ_+ modes cannot be transmitted into the superconducting leads. As a result, S_{SNS} is a 4×4 matrix.

The continuous contributions to the Josephson current are obtained numerically by substituting Eq. (3.36) into Eq. (3.34). The currents are found to be 2π periodic and their magnitude increases with the transmission probability. For small values of τ, the contributions resemble sinusoidal functions, becoming increasingly nonsinusoidal as τ is increased; this must occur as the continuous contributions compensate for subgap levels which escape into the continuum above τ_c. Examples of continuous contributions to the current (measured in in terms of the flux quantum $\Phi_0 = h/2e$) are depicted in Fig. 3.7(a)-(d) for the topological case and in Fig. 3.7(e)-(h) for the nontopological case.

3.5.1.5 Total Josephson current

The total current is calculated by combining the subgap and continuous contributions, as in Eq. (3.31). In the case without energy relaxation, as in the subgap case, we focus on junctions where Andreev levels do not escape into the continuum. However, in the presence of relaxation our discussion includes also the case of escaping levels. Examples are depicted in Fig. 3.8 for topological junctions and in Fig. 3.11(a) for nontopological junctions.

Generally, we find the continuous contributions to be significant relative to the subgap current when the gap asymmetry between Δ_+ and $|\Delta_-|$ is appreciable. The continuous contributions are typically most significant when there are subgap states which escape into the continuum, as then the continuous contributions must account for the missing subgap levels.

There are some distinguishing features between topological and nontopological junctions. One such feature is the fractional Josephson effect: when the phase is swept much faster than the relaxation time of the junction (but not so fast that Landau-Zener tunnelling between branches or to the continuous spectrum occurs), the supercurrent of a topological–topological junction will be 4π periodic [see Fig. 3.8(a)-(b)], twice that of the conventional Josephson effect. This 4π periodicity, however, is sensitive to energy relaxation, which motivates the need for a topological signature in junctions where energy

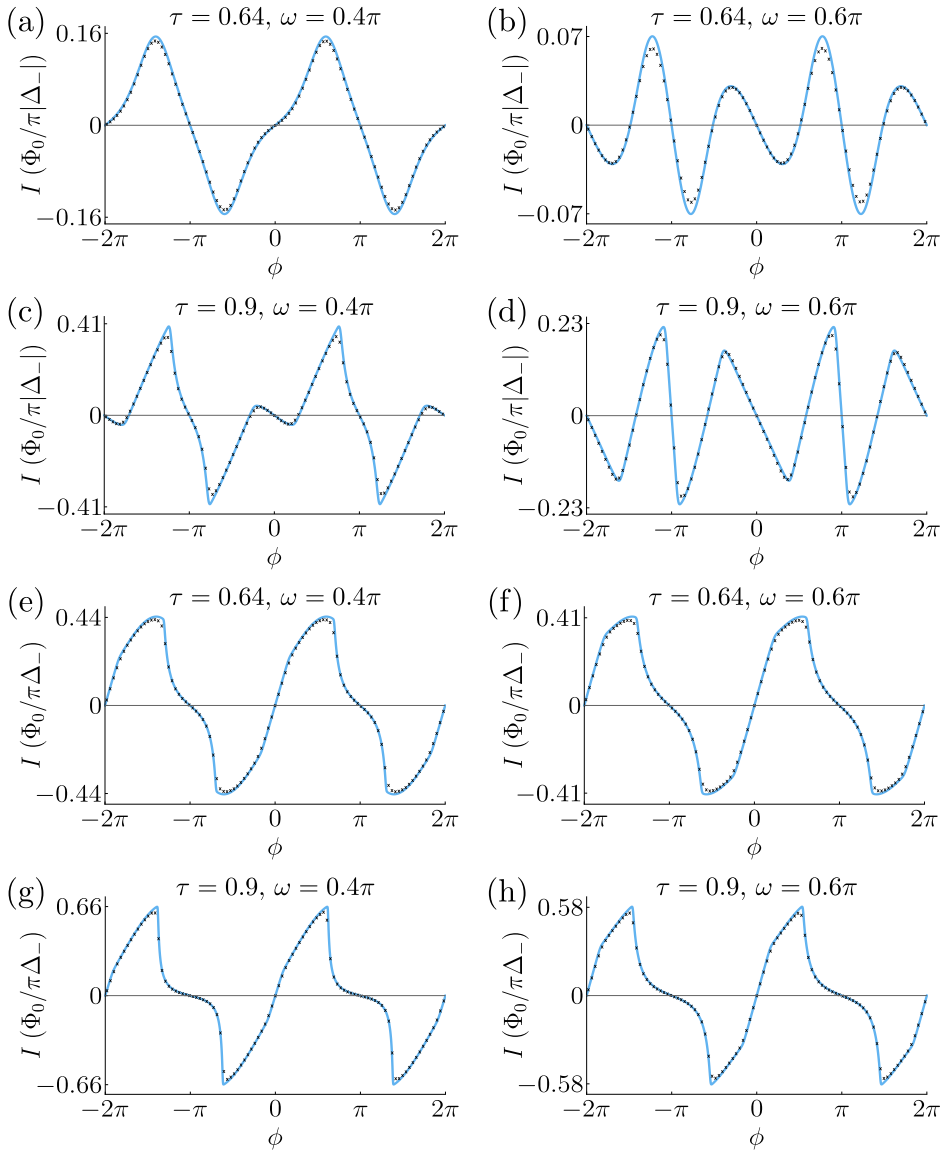

Figure 3.7: (a)-(d) Continuous contributions to the supercurrent for a Josephson junction between topological superconductors with gap parameter $\Delta_+ = -2\Delta_-$ and (e)-(h) its nontopological counterpart with gap parameter $\Delta_+ = 2\Delta_-$. For topological junctions, the critical transmission above which subgap states escape into the continuum is $\tau_c = 0.75$ [see Eq. (3.24)]. The numerical lattice data (black crosses) has gap parameters $\Delta_{0L} = \Delta_{0R} = -0.032$ and $\Delta_{1L} = \Delta_{1R} = 0.054$ for the topological junctions and $\Delta_{0L} = \Delta_{0R} = 0.0027$ and $\Delta_{1L} = \Delta_{1R} = 0.018$ for the nontopological junctions.

relaxation takes place.

A distinctive feature appears in the case with energy relaxation: in topological Josephson junctions, the Josephson current is 2π periodic and displays a current switch at $\phi = (p + 2n + 1)\,\pi$ with $p = 0, 1$ the fermion parity of the junction and n an integer [see Fig. 3.8(c)-(f)]. We have investigated the analogous situation in the nontopological case

where, due to the absence of Andreev level zero crossings and the use of the preparation protocol in Sec. 3.5, only the even parity ground state arises and the corresponding current exhibits switchlike behaviour at $\phi = (2n+1)\,\pi$ when τ is close to unity [see Fig. 3.11(a)]. With regard to establishing switches as topological, it is most judicious to work with junctions having an intermediate value of τ in order to suppress nontopological switches, while still realising Josephson currents of an appreciable magnitude.

When both energy and fermion parity are allowed to relax, further qualitative distinctive features are found to emerge. A single pair of switches occurs in the interval $-\pi < \phi \leq \pi$, with the switch locations given by the zero crossings in Eq. (3.23). As these switches occur symmetrically about $\phi = n\pi$, junctions with a value of ω sufficiently (i.e. determined by the resolution of ϕ) far enough away from $n\pi$ have topological switches that are distinct compared to possible nontopological counterparts. In the case that ω is near $n\pi$, switches may be distinguished from their nontopological variants provided that τ is not too close to unity, as then potential nontopological switchlike false positives do not arise [see Fig. 3.11(a)]. Besides being a topological signature (as explained in Sec. 3.5.1.3), identifying the location of these switches provides a way to measure the value ω for the junction. Lastly, an important characteristic of these topological switches is that the magnitude of the current is not necessarily the same after a switch. Examples of these switches are depicted in Fig. 3.8(g)-(j).

3.5.2 *s*-wave–topological superconductor junctions

For s-wave–topological superconductor junctions, due to the high-energy and low-energy subgap branches being generically (i.e. for τ away from unity) well separated and using the protocol outlined in Sec. 3.5, the cases without relaxation and with energy relaxation only coincide: in terms of the subgap current, they both correspond to always taking the positive high-energy subgap level to be empty. Therefore it is sufficient to consider the cases distinguished by the (non)conservation of fermion parity.

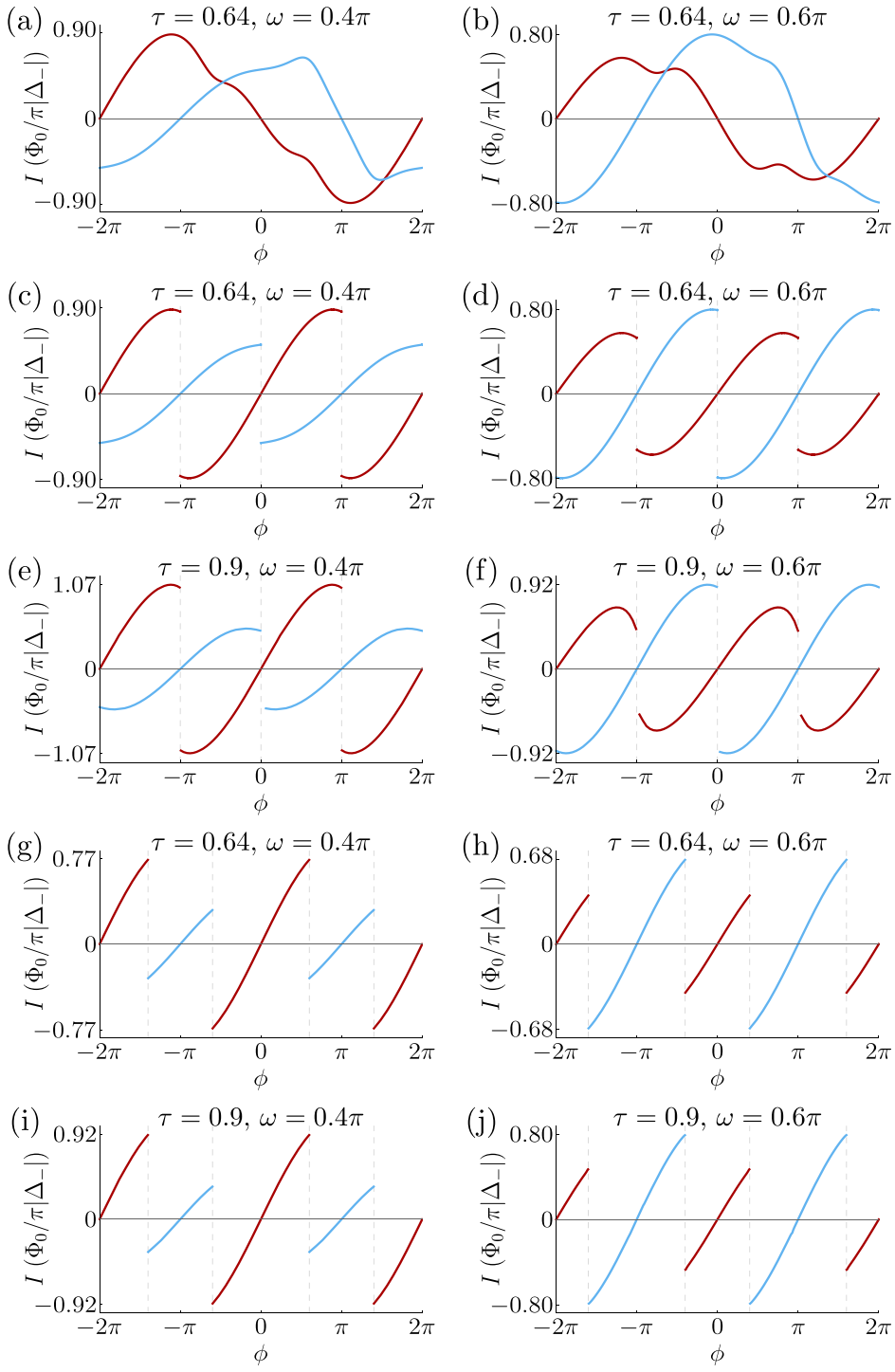

Figure 3.8: The total supercurrent for topological–topological junctions with gap parameter $\Delta_+ = -2\Delta_-$. The blue and red curves represent odd and even parity currents. For (a)-(b) there is no relaxation, for (c)-(f) only energy relaxation is present, and for (g)-(j) fermion parity relaxation is also allowed. Panels (a) and (b) show one of the odd and one of the even parity currents (not displaying the complementary two with opposite subgap contributions). Numerical lattice data has been omitted since the agreement with subgap energies and continuous current contributions has already been shown to be excellent.

3.5.2.1 Subgap current with conserved fermion parity

With a conserved fermion parity, we include the contribution of one of the low-energy branches where the choice of branch depends on the fermion parity of the junction. The resultant current has 2π periodicity.

The nature of the low-energy and high-energy contributions to the Josephson current can be understood in terms of symmetries of the system. Time-reversal symmetry relates an energy at ϕ to one of equal value at $-\phi$. As a result of this and the 2π periodicity of the spectrum, the high-energy Andreev branches are even in ϕ about the time-reversal invariant phases $\phi = n\pi$ and the corresponding current contribution is odd, vanishing at these phases. For the low-energy branches, applying time-reversal brings the energy to the opposite branch related to the initial one by particle-hole symmetry. This implies that time-reversal flips fermion parity, signifying the anomalous time-reversal properties of Majorana–Kramers doublets [69]. At the same time, this also means that the low-energy branches are odd in ϕ about $\phi = n\pi$ and the corresponding contribution to the current is even with finite currents at $\phi = n\pi$. Moreover, as a consequence of particle-hole symmetry, each parity sector of the low-energy Andreev levels contributes oppositely to the current.

3.5.2.2 Subgap current with nonconserved fermion parity

For a nonconserved fermion parity, the energy of the junction is always minimised and branch switches occur at $\phi = n\pi$ (n is an integer), where the low-energy branches cross each other at zero energy due to the emergence of a Kramers pair of Majorana zero modes. This leads to switches in the subgap Josephson current contribution, in agreement with the work of Chung *et al.* [57] in the tunnelling limit. As a result of the vanishing high-energy contribution at $\phi = n\pi$, these current switches are entirely due to the low-energy Andreev levels. Moreover, at the switches the sign of the current is flipped while its magnitude is preserved, which is a feature dictated by the time-reversal properties of the spectrum: the contributions just after the switch are the time-reverse of those just before

the switch. The switch itself, in this sweep regime, is indicative of a flip in the fermion parity. Taken together, these magnitude-preserving sign switches therefore indicate the anomalous time-reversal properties of Majorana–Kramers pairs. As we will see below, this feature is left intact when continuous contributions are taken into consideration.

3.5.2.3 Continuous contributions to the Josephson current

The Josephson current due to the continuous contributions is calculated by substituting the total scattering matrix S_{SNS}, which has the same general form as in Eq. (3.36), into the density of states (3.35), and finally into Eq. (3.34). We find that the continuous contributions are generally nonzero, but only when the energies lie in an intergap regime. Moreover, as with the subgap contributions, the continuous contributions are independent of the spin-orbit scattering.

(a) Above the gaps. The calculation of the contribution to the Josephson current here is similar to the topological–topological case. The Andreev reflection matrix here assumes the same general form as in Eq. (3.37) and the relations (3.38) also hold. As a result of this, S_{SNS} takes the same form as in Eq. (3.39) and so an analogue to Eq. (3.40) can be derived (i.e. involving a determinant which is real). Therefore the contribution to the Josephson current due to energies above the gaps is zero.

(b) Between the gaps. As mentioned in Sec. 3.4.2, there are a number of intergap energy regimes that arise. The specific form of S_{SNS} will change depending on which intergap energy window one works in (as this controls what is allowed to extend indefinitely into the superconductors) and the relative magnitudes of the gap parameters. If we specify the relevant gap parameters $\Delta = \{-|\Delta_-|, -\Delta_+, -\Delta_0\}$, then the intergap contributions are calculated in an analogous fashion to Eq. (3.34) by the integral

$$I_{\mathrm{cont}} = \frac{e}{\hbar}\int_{\min(\Delta)}^{\max(\Delta)} \mathrm{d}E\, E\frac{\partial\rho}{\partial\phi}. \tag{3.41}$$

This integral is calculated numerically in the same way as with topological–topological

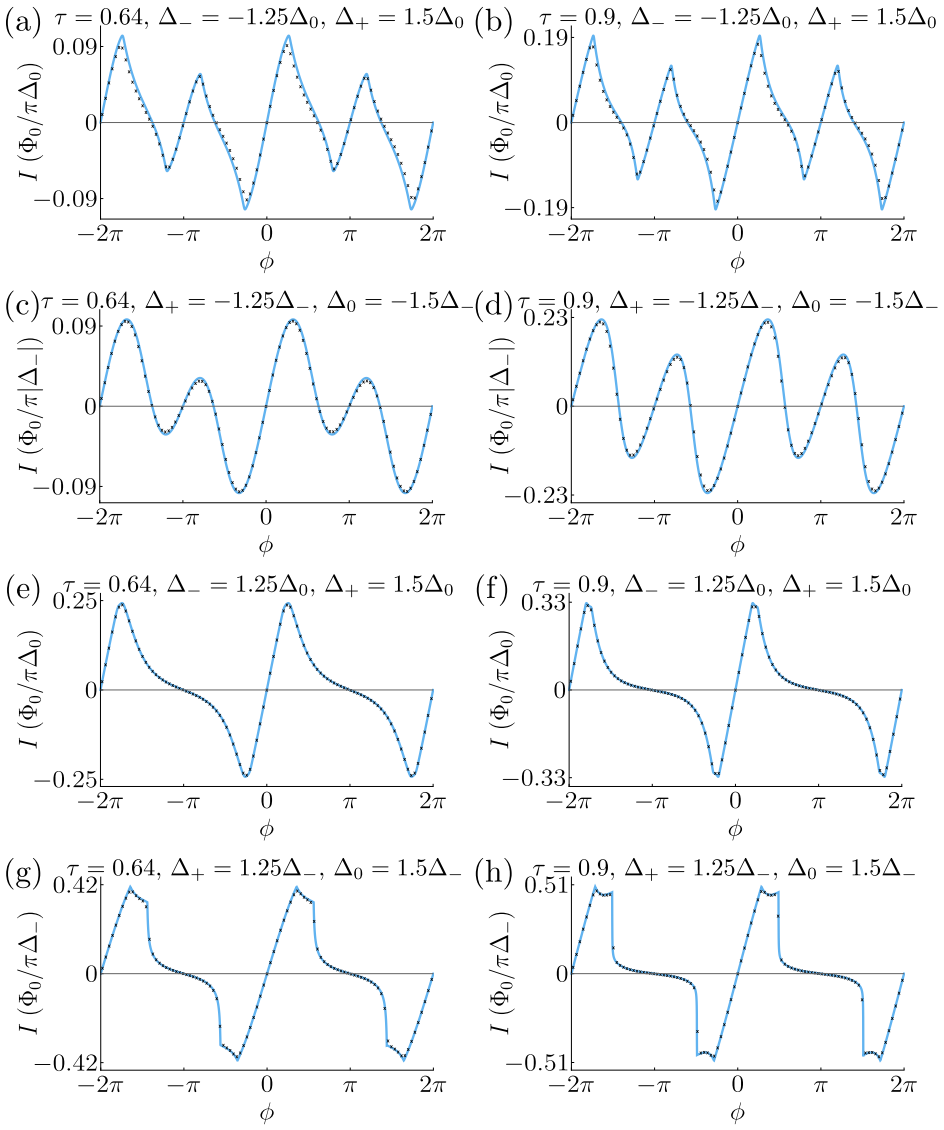

Figure 3.9: (a)-(d) Continuous intergap contributions to the supercurrent for an s-wave–topological Josephson junction and (e)-(h) its nontopological counterpart. The numerical lattice data (black crosses) has gap parameters $\{\Delta_{0\mathrm{L}}, \Delta_{1\mathrm{L}}, \Delta_{0\mathrm{R}}, \Delta_{1\mathrm{R}}\}$ with (a)-(b) $\{0.02, 0, -0.065, 0.099\}$, (c)-(d) $\{0.03, 0, -0.053, 0.081\}$, (e)-(f) $\{0.02, 0, 0.021, 0.009\}$, and (g)-(h) $\{0.03, 0, 0.016, 0.009\}$.

junctions. The continuous contributions for various gap parameters and transmission probabilities can be found for the topological case in Fig. 3.9(a)-(d) and for the nontopological case in Fig. 3.9(e)-(h).

The continuous contributions are zero at $\phi = n\pi$ (with n integer) as energy levels in the continuum must be even in terms of ϕ about the phases $\phi = n\pi$ as a result of time-reversal symmetry. Therefore, the contribution to the total current at these phases is

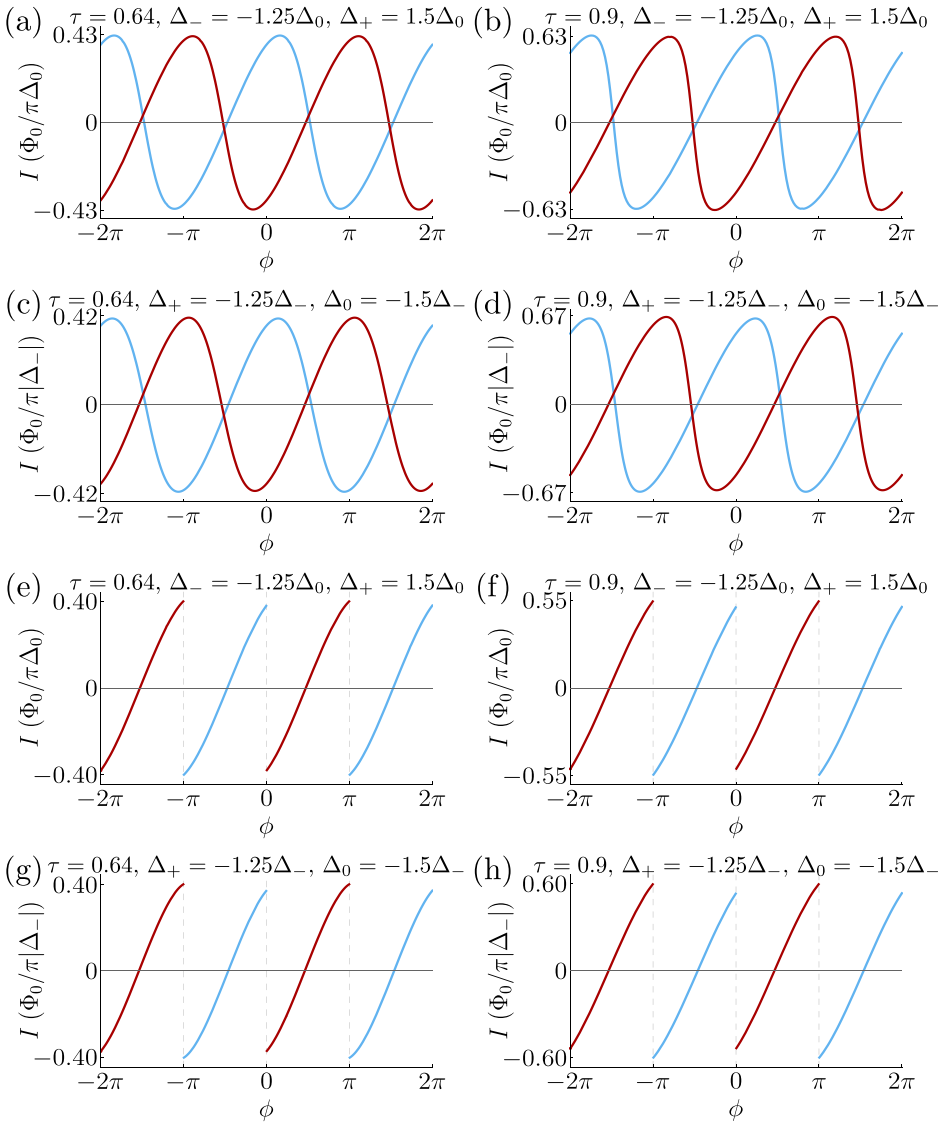

Figure 3.10: The total supercurrent of the s-wave–topological junction. The blue and red curves represent odd and even parity currents. For (a)-(d) local fermion parity is conserved while for (e)-(h) it is violated via relaxation, resulting in current switches at phase differences $\phi = n\pi$ with n integer. Numerical lattice data has been omitted here since the agreement with subgap energies and continuous contributions to the current has already been shown to be excellent.

entirely due to the low-energy Andreev levels, implying that the highlighted key features in the preceding section are not obscured.

3.5.2.4 Total Josephson current

Following Eq. (3.31), the total current is the combination of both the subgap and continuous contributions. We consider the two cases which differ by the conservation of

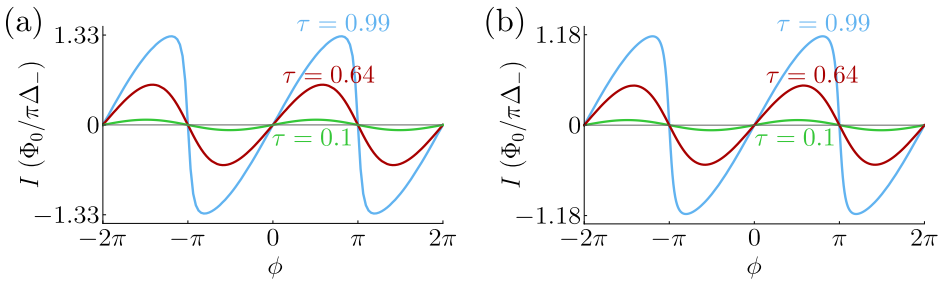

Figure 3.11: The total supercurrent for the nontopological variants of time-reversal-invariant Josephson junctions, where we see the emergence of switchlike features at phase differences $\phi = \pm\pi$ as the transmission probability τ approaches unity. Displayed in (a) is the total supercurrent for a nontopological–nontopological junction with spin-orbit parameter $\omega = 0.4\pi$ and superconducting gaps $\Delta_+ = 2\Delta_-$ and in (b) the total supercurrent for an s-wave–nontopological junction with superconducting gaps $\Delta_+ = 1.25\Delta_-$ and $\Delta_0 = 1.5\Delta_-$. Lattice numerics are omitted here as the agreement with subgap energies and continuous contributions to the current has already been shown to be excellent.

fermion parity. Examples are showcased in Fig. 3.10 for s-wave–topological junctions and in Fig. 3.11(b) for s-wave–nontopological junctions. We remark that, while Fig. 3.10 displays currents for only a few configurations of the gap parameters, other configurations have been calculated with no important qualitative features that are distinct from those shown.

There are some key features in the Josephson currents which can reveal whether or not a junction is topological. The most prominent of these arise in the case with both energy and fermion parity relaxation: topological junctions have magnitude-preserving current switches at phase differences $\phi = n\pi$ (with n integer), where the current at these switch locations is solely due to the low-energy subgap levels. Furthermore, provided that the transmission probability τ of the junction is not too close to unity, analogous magnitude-preserving switches are absent in the nontopological case [see Fig. 3.11(b)]. However, as can be demonstrated using Eq. (3.27), nontopological variants are only able to support switchlike features at $\phi = (2n+1)\pi$, so the observation of current switches in phase increments of π indicates the topological nature of a junction.

In addition to these qualitative signatures, our results allow a quantitative fit to experimental data using the normal-state conductance and the induced gaps as inputs, which may facilitate progress in identifying topological Josephson junctions.

3.6 Numerical simulation

We now turn to testing our predictions on a lattice model [56] for topological superconductivity in hybrid structures based on a Rashba spin-orbit coupled nanowire in proximity to an $s_{\pm}$-wave superconductor. The Hamiltonian consists of a left and a right subsystem, each with N sites,

$$H = H_{0\mathrm{L}} + H_{S\mathrm{L}} + H_{0\mathrm{R}} + H_{S\mathrm{R}} + H_t, \tag{3.42}$$

where $H_{0\mathrm{L}} + H_{S\mathrm{L}}$ describes the left proximitised nanowire, $H_{0\mathrm{R}} + H_{S\mathrm{R}}$ describes the right proximitised nanowire, and

$$H_{0\mathrm{L}} = \sum_{j=1}^{N-1} \left[\left(c_{j+1}^{\dagger} V c_j + \mathrm{H.c.} \right) - \mu c_j^{\dagger} c_j \right], \tag{3.43a}$$

$$H_{0\mathrm{R}} = \sum_{j=N+1}^{2N-1} \left[\left(c_{j+1}^{\dagger} V c_j + \mathrm{H.c.} \right) - \mu c_j^{\dagger} c_j \right], \tag{3.43b}$$

where μ is the chemical potential, $c_j = \begin{pmatrix} c_{j\uparrow} & c_{j\downarrow} \end{pmatrix}^{\mathsf{T}}$, and $V = -\lambda \mathbb{1}_2 - i\lambda_{\mathrm{SO}}\sigma_3$ with real hopping λ and spin-orbit energy λ_{SO}. The pairing is

$$\begin{aligned} H_{S\mathrm{L}} = \frac{1}{2} e^{-i\phi/2} \Bigg(& \sum_{j=1}^{N} \Delta_{0\mathrm{L}} c_j^{\dagger} (i\sigma_2) c_j^{\dagger} + \mathrm{H.c.} \\ & + \sum_{j=1}^{N-1} \Delta_{1\mathrm{L}} c_{j+1}^{\dagger} (i\sigma_2) c_j^{\dagger} + \mathrm{H.c.} \Bigg), \end{aligned} \tag{3.44a}$$

$$\begin{aligned} H_{S\mathrm{R}} = \frac{1}{2} e^{i\phi/2} \Bigg(& \sum_{j=N+1}^{2N} \Delta_{0\mathrm{R}} c_j^{\dagger} (i\sigma_2) c_j^{\dagger} + \mathrm{H.c.} \\ & + \sum_{j=N+1}^{2N-1} \Delta_{1\mathrm{R}} c_{j+1}^{\dagger} (i\sigma_2) c_j^{\dagger} + \mathrm{H.c.} \Bigg) \end{aligned} \tag{3.44b}$$

and in terms of $\Delta_\pm = \Delta_s \pm \Delta_p$, this leads to

$$\Delta_s = \Delta_0 - \Delta_1 \frac{\mu\lambda}{\lambda^2 + \lambda_{\mathrm{SO}}^2}, \tag{3.45a}$$

$$\Delta_p = 2\Delta_1 \lambda_{\mathrm{SO}} \frac{\sqrt{\lambda^2 + \lambda_{\mathrm{SO}}^2 - \mu^2/4}}{\lambda^2 + \lambda_{\mathrm{SO}}^2}. \tag{3.45b}$$

The coupling between the two subsystems is via

$$H_t = c_{N+1}^\dagger \widetilde{V} c_N + \mathrm{H.c.} \tag{3.46}$$

and we allow for arbitrary coupling consistent with time-reversal symmetry, i.e. we take $\widetilde{V} = -\tilde{\lambda} M$ with arbitrary $M \in \mathrm{SU}(2)$ and $\tilde{\lambda}$ real.

The normal-state transmission matrix t, via wavefunction matching, can be shown to be

$$t = \tau e^{i\chi} M, \qquad \tau = \frac{x^2(4 - y^2)}{(x^2+1)^2 - x^2 y^2}, \tag{3.47}$$

where $x = \tilde{\lambda}/\sqrt{\lambda^2 + \lambda_{\mathrm{SO}}^2}$ and $y = \mu/\sqrt{\lambda^2 + \lambda_{\mathrm{SO}}^2}$; the phase χ, explicitly expressible in terms of x and v, plays no role in what follows.

This lattice model is used to numerically investigate the topological–topological and s-wave–topological Josephson junctions and their nontopological counterparts. In general there is excellent agreement between the scattering matrix results and the numerical lattice model. This is despite considering finite size systems and without imposing the Andreev approximation. Parameter values that were used (in units of λ) are $N = 4000$, $\lambda_{\mathrm{SO}} = 0.15$, and $\mu = -0.7$. The corresponding value for $\tilde{\lambda}$ to produce a desired value of τ may be derived from Eq. (3.47). The values for gap parameters depend on the specific junction setup and may be found in the relevant figure captions.

The numerical lattice data is plotted as black crosses and black dashed lines along with various subgap energies and continuous current contributions. For numerical simulations of topological junctions, the subgap energies display a constant line at zero energy which is due to the Majorana fermions at the wire end points away from the junction.

By taking a sufficiently long nanowire, the splitting of these modes is exponentially suppressed to zero. For the nontopological variant, there is no line at zero energy, reflecting the absence of Majorana fermions in the system.

Andreev levels for topological–topological junctions are depicted in Fig. 3.2. The numerics fit closely to the scattering matrix results, correctly reproducing the effect of ω to move the zero crossings in ϕ-space and the feature of subgap states escaping into the continuum. Similar agreement between the lattice model and the scattering matrix results is also achieved for the nontopological variants in Fig. 3.3. The lattice model provides the energy levels of the occupied continuous spectrum and hence the continuous contributions to the current via $I_{\mathrm{cont}} = (\pi/\Phi_0)\,(\mathrm{d}E_{\mathrm{cont}}/\mathrm{d}\phi)$. These contributions are seen for topological–topological junctions in Fig. 3.7(a)-(d) and for nontopological variants in Fig. 3.7(e)-(h), displaying excellent agreement between the lattice model and the scattering matrix calculation.

Similarly for s-wave–topological junctions and the corresponding nontopological variants, the lattice model and scattering matrix calculation are in excellent agreement. The case where an s-wave admixture is included is depicted in Fig. 3.4 for the topological case and in Fig. 3.5 for the nontopological case. The continuous contributions to the supercurrent are shown in Fig. 3.9(a)-(d) for the topological case and in Fig. 3.9(e)-(h) for the nontopological case.

3.7 Conclusion

We have studied the Josephson effect for time-reversal invariant topological–topological and s-wave–topological junctions in the short-junction limit. In terms of the subgap energy spectrum, we found topological generalisations of Beenakker's formula [Eq. (3.4)] for both of the junction setups considered. For topological–topological junctions, one such expression [Eq. (3.22)] holds in the case when the topological superconductors are characterised by $|\Delta_s| \ll |\Delta_p|$. For s-wave–topological junctions in the analogous $\Delta_s \ll$

Δ_p regime, three expressions are found to hold for the cases $\Delta_0 = \Delta_p$ in Eq. (3.28), $\Delta_0 \gg \Delta_p$ in Eq. (3.29), and $\Delta_0 \ll \Delta_p$ in Eq. (3.30), where Δ_0 is the gap parameter for the conventional s-wave superconductor and Δ_s and Δ_p are the respective s-wave and p-wave pairings for the topological superconductor. For more general cases we are able to find simple analytical expressions to establish key features, such as the location of zero crossings and when subgap states are lost to the continuum.

The supercurrent generally has contributions from both the subgap Andreev levels and the continuous spectrum. The continuous contributions originate from states with an energy lying in an intergap regime (arising when there is either an s-wave admixture present in the topological superconductor or a gap asymmetry across the junction). The continuous contributions are generally significant in magnitude relative to the subgap contributions provided that the junction is away from the tunnelling limit and that the intergap regime is not too small.

For topological–topological junctions, we found that the fractional Josephson effect can occur, which has the hallmark of a 4π periodic current. The establishment of such a current, however, is challenging due to energy relaxation. As with class D superconductors, the periodicity can be measured via the AC Josephson effect: the phase sweep may be controlled by the voltage ($\dot{\phi} = 2eV/\hbar$) across the junction and the resulting periodicity of the supercurrent can be measured. The 4π periodicity of the current will only remain intact provided that the phase sweep speed is much faster than t_r ($eV \gg \hbar/t_r$), the typical timescale for energy relaxation (but still slow enough so that Landau-Zener tunnelling between branches or to the continuum is avoided). For the case with energy relaxation ($eV \ll \hbar/t_r$), the current is 2π periodic. This is in contrast to class D superconductors, where the conservation of local fermion parity at the junction suffices to ensure that the 4π periodicity is robust against energy relaxation.

Due to the difficulties posed by energy relaxation in realising a 4π periodic current, we have proposed signatures unique to topological junctions in the presence of energy relaxation. For topological–topological junctions, the regime of fermion parity noncon-

servation is particularly useful. This is the DC Josephson effect where the zero-energy crossings of the Andreev levels [Eq. (3.23)], directly linked to the topological symmetry protected energy-phase relation of Ref. [97], lead to a pair of current switches in the interval $-\pi < \phi \leq \pi$. Via Eq. (3.23), the distance between the switches also provides a direct measure of the spin-orbit parameter ω. For the special values $\omega = n\pi$, the pair of switches degenerate and can be at the same location as the switchlike features of highly transmitting nontopological junctions. To be able to attribute the current switches to that of a topological origin, it is therefore useful to either move the junction away from such special points by changing the spin-orbit coupling or to work away from unit transparency.

For s-wave–topological superconductor junctions, we also found the DC Josephson effect to be the regime with the clearest signatures of topological superconductivity. In this case, magnitude-preserving current switches occur at the time-reversal invariant phases $\phi = n\pi$ (with n integer), reflecting the existence and anomalous time-reversal properties of Majorana–Kramers pairs at these phases. In contrast, nontopological analogues may only support switchlike features for τ close to unity at $\phi = (2n+1)\pi$. Therefore, the observation of magnitude-preserving switches after every phase increment of π is an indicator of topology.

We have worked in the zero temperature limit for both types of junction setup. In terms of the DC Josephson effect, our work may be straightforwardly extended to finite temperature T [15]. The current switches remain intact away from zero temperature provided that $k_{\mathrm{B}}T/\Phi_0 \ll I_{\mathrm{s}}$ is satisfied, where I_{s} is the magnitude of the current switch. As the temperature increases outside of this regime, the switchlike features are lost as they are smoothed out over ϕ-space.

Our work on these junctions provides a direct relationship between the excitation spectrum, the Josephson current, the normal-state conductance $G = \left(2e^2/h\right)\tau$, the various superconducting gaps, and, in the case of topological–topological junctions, the spin-orbit parameter ω. Relations of this type in the nontopological case have been known to be of exceptional utility in quantitative experimental analyses of Josephson junctions

[103–107]. Our results allow the application of the same strategy to the topological case.

Chapter 4

Master equation approach for time-reversal-invariant topological junctions

A number of different regimes were identified and motivated in the previous chapter with regard to the supercurrent flowing across time-reversal-invariant topological Josephson junctions. While the 4π periodicity of the current was lost for regimes involving an energy relaxation timescale that was much faster than the phase sweep, it persisted when the relaxation was sufficiently slow. In this chapter, our goal will be to adopt a master equation approach for junctions between time-reversal-invariant topological superconductors in order to probe, in greater detail, the crossover between the 4π periodic energy-conserving and the energy relaxation dominated regimes. We will consider fermion parity to be conserved.

Such a master equation approach has been found to be of utility in theoretical [54, 98, 108–110] and experimental [111] investigations of junctions involving nontopological [98, 109–111] and (time-reversal symmetry breaking) topological [54, 98, 108] superconductors. Additionally, a recent experiment on a mesoscopic nontopological junction established a similar regime of interest, where external processes associated with parity-conserving

transitions were found to be much faster than their parity-breaking counterparts [112].

The rest of this chapter is structured as follows. Prior to investigating these junctions, it will first be necessary to introduce the density matrix formalism which provides a base upon which the quantum master equation can be derived. Within this framework, a bipartite density operator will be specified in relation to a small subsystem of interest and a large reservoir, allowing for a reduced density operator to be formulated relative to the degrees of freedom of the smaller subsystem only. The exact time evolution of this reduced density operator, however, depends, in principle, upon the full bipartite density matrix. For this reason, a brief outline of a microscopic derivation of the master equation in its so-called Lindblad form is presented, following the works of Refs. [113, 114]. This approximative approach enables the time evolution of the reduced density matrix to be described solely in terms of the reduced density operator.

The remainder of this chapter concerns original work. The Lindblad master equation is well-suited to investigate the aforementioned relaxation regime for the time-reversal-invariant junction between topological superconductors, where the parity-preserving relaxation processes are motivated by an electron-phonon coupling. We use an effective low-energy description for junctions of this type and incorporate the relaxation processes through a phenomenological rate consistent with time-reversal symmetry. In the previous chapter, this regime was found to have current switches (see Sec. 3.5.1.2) which could be attributed to a topological origin for values of the junction transparency τ sufficiently far away from unity. We therefore conclude with our findings for the establishment of these topological current switches with respect to the ratio of the relaxation rate to a linear phase sweep speed.

4.1 The density matrix

Suppose that a quantum system can be described in relation to an eigenbasis of pure states $\{|\psi_n\rangle\}$. If the system is prepared such that there is a classical uncertainty to its

quantum state, i.e. that it can be taken to be a statistical mixture of pure states, then this system can be described by the *density matrix* or *density operator*

$$\rho = \sum_n p_n \left|\psi_n\right\rangle \left\langle\psi_n\right|, \tag{4.1}$$

where $0 \leq p_n \leq 1$ are statistical weights that sum to unity. A key property of this operator with regard to observables follows by tracing it with an operator A,

$$\begin{aligned} \mathrm{tr}\left(\rho A\right) &= \sum_{mn} p_n \left\langle m|\psi_n\right\rangle \left\langle\psi_n|A|m\right\rangle \\ &= \sum_n p_n \left\langle\psi_n\right| A \sum_m \left|m\right\rangle \left\langle m|\psi_n\right\rangle \\ &= \left\langle A\right\rangle . \end{aligned} \tag{4.2}$$

As all measurable information comes from such expectation values, the density operator encapsulates entirely the statistical and quantum mechanical information of a system [115].

4.1.1 Properties of the density matrix

The density matrix has a number of important properties. The first and simplest of these is its Hermiticity

$$\rho = \rho^\dagger, \tag{4.3}$$

which follows straightforwardly from the definition in Eq. (4.1). The second property is

$$\mathrm{tr}\left(\rho\right) = 1, \tag{4.4}$$

which follows from the normalisation condition that the statistical weights must obey. The third property is that of positive semidefiniteness

$$\begin{aligned}\langle\psi|\rho|\psi\rangle &= \sum_n p_n \langle\psi|\psi_n\rangle \langle\psi_n|\psi\rangle \\ &= \sum_n p_n |\langle\psi_n|\psi\rangle|^2 \geq 0 \end{aligned} \tag{4.5}$$

for some state ψ. The fourth and final property is

$$\begin{aligned}\mathrm{tr}\left(\rho^2\right) &= \sum_{mno} p_n p_o \langle m|\psi_n\rangle \langle\psi_n|\psi_o\rangle \langle\psi_o|m\rangle \\ &= \sum_{no} p_n p_o |\langle\psi_n|\psi_o\rangle|^2 \leq 1, \end{aligned} \tag{4.6}$$

where the inequality in the second line follows from $|\langle\psi_n|\psi_o\rangle|^2 \leq 1$ along with the second property. The equality holds in the case that the system is in a pure state, i.e. $p_n = 1$ for some n [116].

4.1.2 Time evolution of the density matrix

The behaviour of the density matrix as time is evolved may be understood by examining the corresponding behaviour of the Schrödinger equation for the wavefunction $|\psi(t)\rangle$,

$$H|\psi(t)\rangle = i\hbar \frac{\mathrm{d}}{\mathrm{d}t}|\psi(t)\rangle, \tag{4.7}$$

The time evolution of the density operator

$$\rho(t) = \sum_n p_n |\psi_n(t)\rangle \langle\psi_n(t)| \tag{4.8}$$

is then

$$\frac{\mathrm{d}\rho}{\mathrm{d}t} = -\frac{i}{\hbar}[H, \rho], \tag{4.9}$$

where the Schrödinger equation along with its Hermitian conjugate have been used. This is the *von Neumann equation*, which governs the behaviour of the density matrix as a function of time.

So far the Schrödinger picture has been implicitly assumed where the time dependence comes entirely from the state vectors. Taking the formal solution of Eq. (4.7) yields

$$|\psi(t)\rangle = U(t)\,|\psi(t_0)\rangle\,, \tag{4.10}$$

where $|\psi(t_0)\rangle$ is some known initial state at a reference time t_0 and $U(t) = e^{-iH(t-t_0)/\hbar}$ is the unitary time evolution operator for a time-independent H. The separation of $U(t)$ is central to the Heisenberg representation, allowing for the time dependence of the state vectors to be shunted onto the operators. Therefore, the density matrix takes the form $\rho_{\mathrm{H}} = U^{\dagger}(t)\,\rho(t)\,U(t)$ in the Heisenberg picture. (Note that the subscript "H" is used to indicate the Hesienberg picture and the omission of a subscript should be taken to indicate the Schrödinger picture for operators and kets.)

It is sometimes convenient to work in a hybrid between the Schrödinger and Heisenberg pictures—the interaction picture. The systems relevant to such a picture have Hamiltonians of the form

$$H = H_0 + V(t)\,, \tag{4.11}$$

where H_0 is time-independent and $V(t)$ is a time-dependent perturbation. The time dependence of the wavefunction is then partially removed in analogue to Eq. (4.10) via

$$|\psi(t)\rangle = \tilde{U}(t)\left|\tilde{\psi}(t)\right\rangle, \tag{4.12}$$

where the tilde represents the associated quantity in the interaction picture and $\tilde{U}(t) = e^{-iH_0(t-t_0)/\hbar}$. The usefulness of such a transformation lies in the fact that, for small

perturbations, the time dependence of state vectors in the interaction picture comes solely from the perturbation. The density matrix and perturbation term in the interaction picture are

$$\tilde{\rho}(t) = \tilde{U}^{\dagger}(t)\,\rho(t)\,\tilde{U}(t)\,, \tag{4.13a}$$

$$\tilde{V}(t) = \tilde{U}^{\dagger}(t)\,V(t)\,\tilde{U}(t)\,, \tag{4.13b}$$

and the corresponding von Neumann equation is

$$\begin{aligned}\frac{\mathrm{d}\tilde{\rho}}{\mathrm{d}t} &= \tilde{U}^{\dagger}(t)\left(\frac{i}{\hbar}\left[H_0,\rho(t)\right]+\frac{\mathrm{d}\rho}{\mathrm{d}t}\right)\tilde{U}(t)\\ &= -\frac{i}{\hbar}\tilde{U}^{\dagger}(t)\left[V(t),\rho(t)\right]\tilde{U}(t)\\ &= -\frac{i}{\hbar}\left[\tilde{V}(t),\tilde{\rho}(t)\right],\end{aligned} \tag{4.14}$$

where the von Neumann equation in the Schrödinger picture [Eq. (4.9)] has been inserted between the first and second lines. Finally, one should note that the expected value of an operator is invariant with regard to the picture; for example, in the interaction picture (suppressing time dependence for brevity)

$$\mathrm{tr}\left(\tilde{\rho}\tilde{A}\right) = \mathrm{tr}\left(\tilde{U}^{\dagger}\rho\tilde{U}\tilde{U}^{\dagger}A\tilde{U}\right) = \langle A\rangle\,, \tag{4.15}$$

where the cyclic property of the trace has been used [115, 117].

4.1.3 The reduced density matrix

The von Neumann equation in the interaction picture is the foundation upon which the master equation, to be discussed in detail in the following section, is derived. However, at this stage, one may question the usefulness of the approximative master equation when the exact von Neumann equation allows for the solution of the density matrix and hence access to all measurable information. The answer is related to practicality, where the

usefulness arises for a particular type of system which is bipartite, specifically those that are composed of a small subsystem of interest and a large reservoir or environment where one is only interested in the environment insofar as to its effect on the smaller subsystem. Therefore, the utility of the master equation becomes apparent when the large number of degrees of freedom associated with the environment are effectively integrated out, allowing the problem to be expressed in terms of the relatively small number of degrees of freedom of the subsystem of interest—such a reduced system is significantly more tractable. This motivates the reduced density operator, which can be taken as the density operator for the subsystem of interest extricated from the environment. The next step is thus to formulate this operator.

Let the total bipartite density matrix be ϱ and the reduced density matrix describing the subsystem of interest be ρ, where both are assumed to be given in the Schrödinger picture. The bipartite density operator can be described in terms of the product of states between the subsystem of interest $\{|s\rangle\}$ and the bath $\{|b\rangle\}$, while the reduced density operator only requires the states $\{|s\rangle\}$.

Furthermore, the reduced density operator must satisfy the property regarding expectation values [Eq. (4.2)] for any subsystem operator A, so that the trace can be taken to be partial, i.e.

$$\langle A\rangle = \sum_s \langle s|\rho A|s\rangle = \mathrm{tr_S}\left(\rho A\right). \tag{4.16}$$

Of course, the same average can be calculated using the bipartite density operator,

$$\langle A\rangle = \mathrm{tr_{S+B}}\left(\varrho A\right) = \sum_{sbs'b'} \left\langle sb\middle|\varrho\middle|s'b'\right\rangle \left\langle s'b'\middle|A\middle|sb\right\rangle, \tag{4.17}$$

where the resolution of unity has been inserted for the second equality. However, in order for A to be an operator defined purely on the subsystem, it follows that

$$\left\langle s'b'\middle|A\middle|sb\right\rangle = \left\langle s'\middle|A\middle|s\right\rangle \delta_{b'b} \tag{4.18}$$

and hence Eq. (4.17) becomes

$$\langle A \rangle = \sum_{ss'b} \langle sb | \varrho | s'b \rangle \langle s' | A | s \rangle = \mathrm{tr_S} \left[\mathrm{tr_B} \left(\varrho \right) A \right]. \tag{4.19}$$

By matching Eq. (4.16) and Eq. (4.19), the reduced density matrix can be simply defined in terms of the bipartite density matrix as

$$\rho = \mathrm{tr_B} \left(\varrho \right). \tag{4.20}$$

Similarly, by taking the time-independent part of the Hamiltonian [Eq. (4.11)] to be bipartite in the same way (i.e. $H_0 = H_\mathrm{S} + H_\mathrm{B}$), the von Neumann equation in the Schrödinger picture [Eq. (4.9)] can be expressed in relation to the reduced density matrix by taking its partial trace with respect to the reservoir to yield

$$\frac{\mathrm{d}\rho}{\mathrm{d}t} = -\frac{i}{\hbar} \left[H_\mathrm{S}, \rho \right] - \frac{i}{\hbar} \mathrm{tr_B} \left[V, \varrho \right]. \tag{4.21}$$

The reduced density matrix $\tilde{\rho}\left(t\right)$ in the interaction picture follows by taking the partial trace of Eq. (4.13a),

$$\begin{aligned} \tilde{\rho}\left(t\right) &= \mathrm{tr_B} \left[\tilde{\varrho}\left(t\right) \right] \\ &= \tilde{U}_\mathrm{S}^\dagger \left(t\right) \mathrm{tr_B} \left[\tilde{U}_\mathrm{B}^\dagger \left(t\right) \varrho \left(t\right) \tilde{U}_\mathrm{B} \left(t\right) \right] \tilde{U}_\mathrm{S} \left(t\right) \\ &= \tilde{U}_\mathrm{S}^\dagger \left(t\right) \rho \left(t\right) \tilde{U}_\mathrm{S} \left(t\right) \end{aligned} \tag{4.22}$$

where $U_\mathrm{S/B} = e^{iH_\mathrm{S/B}(t-t_0)/\hbar}$ and the cyclic commutative property of the trace has been used. Note that as the right-hand-side of Eq. (4.22) is only in terms of the subsystem of interest, the density matrix in the interaction picture has been reduced.

Finally, the von Neumann equation may be expressed in the reduced description for

the interaction picture by taking the derivative with respect to time of Eq. (4.22), yielding

$$\begin{aligned}\frac{\mathrm{d}\tilde{\rho}}{\mathrm{d}t} &= \tilde{U}_{\mathrm{S}}^{\dagger}(t)\left\{\frac{i}{\hbar}\left[H_{\mathrm{S}},\rho(t)\right]+\frac{\mathrm{d}\rho}{\mathrm{d}t}\right\}\tilde{U}_{\mathrm{S}}(t)\\ &= \frac{i}{\hbar}\left[H_{\mathrm{S}},\tilde{\rho}(t)\right]-\frac{i}{\hbar}\tilde{U}_{\mathrm{S}}^{\dagger}(t)\left\{\left[H_{\mathrm{S}},\rho(t)\right]+\mathrm{tr}_{\mathrm{B}}\left[V(t),\varrho(t)\right]\right\}\tilde{U}_{\mathrm{S}}(t)\\ &= -\frac{i}{\hbar}\,\mathrm{tr}_{\mathrm{B}}\left[\tilde{V}(t),\tilde{\varrho}(t)\right], \end{aligned} \tag{4.23}$$

where Eq. (4.21) has been used for the second line and Eq. (4.13) has been used for the final line [117].

The von Neumann equation in the reduced description has now been formulated, but while it involves the partial tracing out of the bath, its right-hand-side still involves the total bipartite density matrix $\tilde{\varrho}(t)$. As a result, one cannot use this equation to describe the time evolution of the reduced density operator solely in terms of the variables of the subsystem. To make progress, certain approximations will need to be made, leading to the master equation as discussed in the following section.

4.2 The quantum master equation

The quantum master equation in its Lindblad form is a system of first-order Markovian differential equations describing the nonunitary time evolution of a class of density matrices which represent a small subsystem coupled externally to a large reservoir. Its usefulness resides in its wide applicability and its efficacy as it only involves the reduced density matrix where the nonunitary part enters through a correlation function which captures interactions between the small subsystem and the environment. In the rest of this section, a brief outline of a microscopic derivation of the Lindblad form of the master equation is presented, following the works of Refs. [113, 114].

The starting point for the master equation derivation is the von Neumann equation

in the interaction picture,

$$\frac{\mathrm{d}\tilde{\rho}}{\mathrm{d}t} = \frac{1}{i\hbar}\,\mathrm{tr}_{\mathrm{B}}\left[\tilde{V}\left(t\right),\tilde{\varrho}\left(t\right)\right], \tag{4.24}$$

where the Hamiltonian of the system takes the form $H = H_{\mathrm{S}} + H_{\mathrm{B}} + V\left(t\right)$. Formal integration with respect to time of such an equation between the initial time t and a later time $t + \Delta t$ yields

$$\Delta\tilde{\rho}\left(t\right) = \frac{1}{i\hbar}\int_{t}^{t+\Delta t}\mathrm{d}t_{1}\,\mathrm{tr}_{\mathrm{B}}\left[\tilde{V}\left(t_{1}\right),\tilde{\varrho}\left(t_{1}\right)\right], \tag{4.25}$$

where $\Delta\tilde{\rho}\left(t\right) = \tilde{\rho}\left(t+\Delta t\right) - \tilde{\rho}\left(t\right)$. The above expression may be iteratively integrated further by utilising

$$\tilde{\rho}\left(t_{k}\right) = \mathrm{tr}_{\mathrm{B}}\left\{\tilde{\varrho}\left(t\right) + \frac{1}{i\hbar}\int_{t}^{t_{k}}\mathrm{d}t_{k+1}\left[\tilde{V}\left(t_{k+1}\right),\tilde{\varrho}\left(t_{k+1}\right)\right]\right\}, \tag{4.26}$$

so that after two more iterations

$$\begin{aligned}\Delta\tilde{\rho}\left(t\right) =& \frac{1}{i\hbar}\int_{t}^{t+\Delta t}\mathrm{d}t_{1}\,\mathrm{tr}_{\mathrm{B}}\left[\tilde{V}\left(t_{1}\right),\tilde{\varrho}\left(t\right)\right] \\ &+ \frac{1}{\left(i\hbar\right)^{2}}\int_{t}^{t+\Delta t}\mathrm{d}t_{1}\int_{t}^{t_{1}}\mathrm{d}t_{2}\,\mathrm{tr}_{\mathrm{B}}\left[\tilde{V}\left(t_{1}\right),\left[\tilde{V}\left(t_{2}\right),\tilde{\varrho}\left(t\right)\right]\right] \\ &+ \frac{1}{\left(i\hbar\right)^{3}}\int_{t}^{t+\Delta t}\mathrm{d}t_{1}\int_{t}^{t_{1}}\mathrm{d}t_{2}\int_{t}^{t_{2}}\mathrm{d}t_{3}\,\mathrm{tr}_{\mathrm{B}}\left[\tilde{V}\left(t_{1}\right),\left[\tilde{V}\left(t_{2}\right),\left[\tilde{V}\left(t_{3}\right),\tilde{\varrho}\left(t_{3}\right)\right]\right]\right],\end{aligned} \tag{4.27}$$

where the time-ordering is $t + \Delta t \geq t_{1}$ and $t_{k} \geq t_{k+1}$. Note that the integral equation in its present form is exact; the purpose of iteratively integrating has been to push the the t_{k} dependence of ϱ to higher-order terms. As it will soon become apparent, the second-order term is vital, and by iterating to third-order or higher, the density operator appearing in the second-order term of the integrand depends only upon the initial moment of time t.

A discussion on the timescales of the system is now appropriate. The timescale Δt has already been introduced as the time increment for the density matrix. Two more relevant timescales arise when considering the reservoir and the small subsystem of interest. In

the case of the former, correlations within the reservoir are taken to have a lifetime characterised by the timescale τ_{B}. With respect to the latter, the small subsystem of interest has a characteristic relaxation timescale T_{S} due to interactions with the reservoir and is defined by

$$\frac{\Delta\tilde{\rho}\left(t\right)}{\Delta t} \sim \frac{1}{T_{\mathrm{S}}}\tilde{\rho}\left(t\right). \tag{4.28}$$

A key assumption for the system being dealt with is

$$\tau_{\mathrm{B}} \ll \Delta t \ll T_{\mathrm{S}}, \tag{4.29}$$

which effectively states that the correlations of the reservoir decay rapidly, while the relaxation timescale is considerably longer for the subsystem of interest. Alternatively, from the uncertainty principle, the condition $\tau_{\mathrm{B}} \ll T_{\mathrm{S}}$ can be formulated in terms of an average interaction strength $\bar{V}$, so that

$$\frac{\bar{V}\tau_{\mathrm{B}}}{\hbar} \ll 1 \tag{4.30}$$

must also be satisfied.

Furthermore, it should be noted that the bipartite density matrix can be generally written in two parts: as a product between the reduced density matrices of the subsystem and the reservoir, and the correlations between the subsystem and the reservoir

$$\tilde{\varrho} = \tilde{\rho}\left(t\right) \otimes \mathrm{tr}_{\mathrm{S}}\left[\tilde{\varrho}\left(t\right)\right] + \tilde{\rho}_{\mathrm{correlations}}\left(t\right). \tag{4.31}$$

In what follows, we focus on simplifying the uncorrelated part of Eq. (4.27).

As the reservoir has a short relaxation timescale, it is assumed to thermalise to a temperature T before any meaningful changes can occur in the subsystem of interest. The

reduced density operator for the bath becomes

$$\sigma = \mathrm{tr}_{\mathrm{S}}\left[\tilde{\varrho}\left(t\right)\right] = \sum_{b} Z^{-1} e^{-E_b/k_{\mathrm{B}}T} \left|b\right\rangle \left\langle b\right|, \quad Z = \sum_{b} e^{-E_b/k_{\mathrm{B}}T}. \tag{4.32}$$

By expressing the interaction part of the Hamiltonian via the operators for the reservoir B_α and the subsystem of interest S_α, i.e.

$$\tilde{V} = \sum_{\alpha} \tilde{S}_\alpha \otimes \tilde{B}_\alpha, \tag{4.33}$$

along with the assumption that the average $\mathrm{tr}_{\mathrm{B}}\left[B_\alpha \sigma\right] = 0$, then it follows that

$$\mathrm{tr}_{\mathrm{B}}\left(\tilde{B}_\alpha \sigma\right) = \mathrm{tr}_{\mathrm{B}}\left(e^{iH_{\mathrm{B}}t/\hbar} B_\alpha e^{-iH_{\mathrm{B}}t/\hbar} \sigma\right) = \mathrm{tr}_{\mathrm{B}}\left(B_\alpha \sigma\right) = 0 \tag{4.34}$$

where cyclic permutations of the trace and the commutativity between σ and H_{B} have been used. Therefore, the first-order term in the uncorrelated part of Eq. (4.27) vanishes since its integrand vanishes,

$$\mathrm{tr}_{\mathrm{B}}\left[\tilde{V}\left(t_1\right), \tilde{\varrho}\left(t\right)\right] = \sum_{\alpha} \left\{\tilde{S}_\alpha\left(t_1\right)\tilde{\rho}\,\mathrm{tr}_{\mathrm{B}}\left[\tilde{B}_\alpha\left(t_1\right)\sigma\right] - \tilde{\rho}\tilde{S}_\alpha\left(t_1\right)\mathrm{tr}_{\mathrm{B}}\left[\sigma\tilde{B}_\alpha\left(t_1\right)\right]\right\} = 0. \tag{4.35}$$

The order of magnitude of the remaining uncorrelated terms of Eq. (4.27) can now be estimated. The interactions are approximated by their average strength $\bar{V}$ and, owing to the rapidly decaying bath correlations, the integrals themselves can be taken to contribute terms like $\tau_{\mathrm{B}}^{n-1}\Delta t$ at each order n. A term at order n then has the estimated magnitude

$$\left.\frac{\Delta\tilde{\rho}}{\Delta t}\right|^{(n)} \sim \left(\frac{\bar{V}\tau_{\mathrm{B}}}{\hbar}\right)^{n} \frac{\tilde{\rho}}{\tau_{\mathrm{B}}} \tag{4.36}$$

so that, as a result of Eq. (4.30), the series expansion of Eq. (4.27) can be truncated to second order. Moreover, this allows for an estimate of the timescale governing the

subsystem of interest

$$\frac{1}{T_{\mathrm{S}}} \sim \frac{\bar{V}^2 \tau_{\mathrm{B}}}{\hbar^2}. \tag{4.37}$$

It should also be noted that the correlated part can be taken to be negligible by a similar argument. The interaction strength is again replaced by its mean value, but the integrals contribute terms like τ_{B}^n at order n as the correlations rapidly decay for time differences greater than τ_{B}. At second order, the correction due to the correlations is approximately

$$\frac{1}{T_{\mathrm{S}}} \frac{\tau_{\mathrm{B}}}{\Delta t} \ll \frac{1}{T_{\mathrm{S}}}, \tag{4.38}$$

which is negligible as a result of the assumptions on the timescales [Eq. (4.29)]. Hence, when Eqs. (4.29) and (4.30) hold, it is justified to take only the uncorrelated part of the density matrix as contributing in the truncated form of Eq. (4.27). Therefore, the truncated form for the time evolution of the reduced density operator now reads

$$\Delta\tilde{\rho}\left(t\right) = \frac{1}{\left(i\hbar\right)^2} \int_t^{t+\Delta t} \mathrm{d}t_1 \int_t^{t_1} \mathrm{d}t_2 \, \mathrm{tr}_{\mathrm{B}} \sum_{\alpha\beta} \left[\tilde{S}_\alpha\left(t_1\right) \otimes \tilde{B}_\alpha\left(t_1\right), \left[\tilde{S}_\beta\left(t_2\right) \otimes \tilde{B}_\beta\left(t_2\right), \tilde{\rho} \otimes \sigma\left(t\right)\right]\right]. \tag{4.39}$$

By taking the eigendecomposition of the Hamiltonian for the subsystem of interest $H_{\mathrm{S}} = \sum_n \hbar\omega_n \left|n\right\rangle \left\langle n\right|$, the operators S_α can formally be given a frequency dependence by introducing

$$S_\alpha\left(\Omega\right) = \sum_{mn} \delta\left(\omega_{nm} - \Omega\right) \left|m\right\rangle \left\langle m\right| S_\alpha \left|n\right\rangle \left\langle n\right|, \tag{4.40}$$

where δ is a Kronecker delta and $\omega_{nm} = \left(E_n - E_m\right)/\hbar$. Using this we have

$$S_\alpha = \sum_\Omega S_\alpha\left(\Omega\right). \tag{4.41}$$

The corresponding operator in the interaction picture can then be written as

$$\begin{aligned}\tilde{S}_{\alpha}(\Omega) &= e^{iH_{\mathrm{S}}t/\hbar} S_{\alpha}(\Omega) e^{-iH_{\mathrm{s}}t/\hbar} \\ &= e^{-i\Omega t} S_{\alpha}(\Omega),\end{aligned} \tag{4.42}$$

which, upon substitution into Eq. (4.39), yields

$$\begin{aligned}\Delta\tilde{\rho}(t) = \frac{1}{\hbar^2}\int_{t}^{t+\Delta t} \mathrm{d}t_1 \int_{t}^{t_1} \mathrm{d}t_2 \sum_{\substack{\alpha\beta \\ \Omega\Omega'}} \Big\{ & e^{i\left(\Omega'-\Omega\right)t_1} e^{i\Omega(t_1-t_2)} G_{\alpha\beta}(t_1-t_2) \\ & \times \Big[S_{\beta}(\Omega)\,\tilde{\rho}(t)\, S_{\alpha}^{\dagger}\left(\Omega'\right) - S_{\alpha}^{\dagger}\left(\Omega'\right) S_{\beta}(\Omega)\,\tilde{\rho}(t) \Big] + \mathrm{H.c.} \Big\},\end{aligned} \tag{4.43}$$

where the commutator has been expanded with the appropriate Hermitian conjugate pairs grouped together and the reservoir correlation function

$$\begin{aligned}G_{\alpha\beta}(t_1,t_2) &= \mathrm{tr}_{\mathrm{B}}\left[\tilde{B}_{\alpha}^{\dagger}(t_1)\,\tilde{B}_{\beta}(t_2)\,\sigma_{\mathrm{B}}\right] \\ &= \mathrm{tr}_{\mathrm{B}}\left[e^{iH_{\mathrm{B}}(t_1-t_2)/\hbar} B_{\alpha}^{\dagger} e^{-iH_{\mathrm{B}}(t_1-t_2)/\hbar} B_{\beta}\sigma_{\mathrm{B}}\right] \\ &= G_{\alpha\beta}(t_1-t_2)\end{aligned} \tag{4.44}$$

has been identified.

The argument of the reservoir correlation function suggests that the substitution $\tau = t_1 - t_2$ may be useful. In terms of the variables (t_1, t_2), the limits of the integrals in Eq. (4.43) sweep out a triangular area with vertices placed at (t,t), $(t, t+\Delta t)$, and $(t+\Delta t, t+\Delta t)$. The straight line connecting the first and third vertices corresponds to $\tau = 0$, while the parallel line passing through the second vertex corresponds to $\tau = \Delta t$. Therefore, the triangular area that is swept out can be equivalently described in terms of the variables (τ, t_1), where the limits of integration span $\tau \in (0, \Delta t)$ and $t_1 \in (t+\tau, t+\Delta t)$. Moreover, as the correlations decay rapidly for $\tau > \tau_{\mathrm{B}}$, negligible errors are introduced by extending the integration limits to $\tau \in (0, \infty)$ and $t_1 \in (t, t+\Delta t)$. Following through with this substitution, performing the integration over t_1, and dividing

through by Δt, Eq. (4.43) takes the form

$$\begin{aligned}\frac{\mathrm{d}\tilde{\rho}}{\mathrm{d}t} =& \frac{1}{\hbar^2}\sum_{\substack{\alpha\beta\\ \Omega\Omega'}}\Big\{e^{i\left(\Omega'-\Omega\right)(t+\Delta t/2)}\,\frac{\sin\left[\left(\Omega'-\Omega\right)\Delta t/2\right]}{\left(\Omega'-\Omega\right)\Delta t/2}W_{\alpha\beta}\left(\Omega\right)\\ &\times\Big[S_\beta\left(\Omega\right)\tilde{\rho}\left(t\right)S_\alpha^\dagger\left(\Omega'\right)-S_\alpha^\dagger\left(\Omega'\right)S_\beta\left(\Omega\right)\tilde{\rho}\left(t\right)\Big]+\mathrm{H.c.}\Big\},\end{aligned} \tag{4.45}$$

where the half-Fourier transform of the reservoir correlator has been introduced as

$$W_{\alpha\beta}=\int_0^\infty \mathrm{d}\tau\, e^{i\Omega\tau}G_{\alpha\beta}\left(\tau\right) \tag{4.46}$$

and the quantity $\Delta\tilde{\rho}\left(t\right)/\Delta t$ has been replaced by the coarse-grained derivative $\mathrm{d}\tilde{\rho}/\mathrm{d}t$, which is the Markovian approximation since any influence of the past behaviour of $\tilde{\rho}\left(t\right)$ has been neglected—only the current value of $\tilde{\rho}\left(t\right)$ determines its instantaneous rate of change.

By transitioning to the Schrödinger picture via substitution of Eq. (4.13a) into Eq. (4.45), respectively premultiplying and postmultiplying by $e^{-iH_\mathrm{S}t/\hbar}$ and $e^{iH_\mathrm{S}t/\hbar}$, and using Eq. (4.42) to identify that

$$e^{-iH_\mathrm{S}t/\hbar}S_\alpha\left(\Omega\right)e^{iH_\mathrm{S}t/\hbar}=e^{i\Omega t}S_\alpha\left(\Omega\right), \tag{4.47a}$$

$$e^{-iH_\mathrm{S}t/\hbar}S_\alpha^\dagger\left(\Omega\right)e^{iH_\mathrm{S}t/\hbar}=e^{-i\Omega t}S_\alpha^\dagger\left(\Omega\right), \tag{4.47b}$$

the time derivative of the reduced density matrix becomes

$$\begin{aligned}\frac{\mathrm{d}\rho}{\mathrm{d}t} =& -\frac{i}{\hbar}\left[H_\mathrm{S},\rho\left(t\right)\right]+\frac{1}{\hbar^2}\sum_{\substack{\alpha\beta\\ \Omega\Omega'}}\Big\{e^{i\left(\Omega'-\Omega\right)\Delta t/2}\,\frac{\sin\left[\left(\Omega'-\Omega\right)\Delta t/2\right]}{\left(\Omega'-\Omega\right)\Delta t/2}W_{\alpha\beta}\left(\Omega\right)\\ &\times\Big[S_\beta\left(\Omega\right)\rho\left(t\right)S_\alpha^\dagger\left(\Omega'\right)-S_\alpha^\dagger\left(\Omega'\right)S_\beta\left(\Omega\right)\rho\left(t\right)\Big]+\mathrm{H.c.}\Big\}.\end{aligned} \tag{4.48}$$

The next simplification as regards the master equation is known as the secular approxi-

mation, amounting to

$$e^{i\left(\Omega'-\Omega\right)\Delta t/2}\frac{\sin\left[\left(\Omega'-\Omega\right)\Delta t/2\right]}{\left(\Omega'-\Omega\right)\Delta t/2}=\begin{cases}1 & \text{if } \Omega=\Omega',\\ 0 & \text{if } \Omega\neq\Omega',\end{cases} \tag{4.49}$$

which is valid for times Δt which are significantly larger than the inverse of the corresponding frequency spacings—this follows since the function has a maximum at $\Omega=\Omega'$ where it is unity and for $\left(\Omega'-\Omega\right)\Delta t\ll 1$ the function is near its maximum and for $\left(\Omega'-\Omega\right)\Delta t\gg 1$ the function has negligible value. With this last approximation, the master equation reads

$$\frac{\mathrm{d}\rho}{\mathrm{d}t}=-\frac{i}{\hbar}\left[H_{\mathrm{S}},\rho\left(t\right)\right]+\frac{1}{\hbar^{2}}\sum_{\substack{\alpha\beta\\ \Omega}}\left\{W_{\alpha\beta}\left(\Omega\right)\left[S_{\beta}\left(\Omega\right)\rho\left(t\right)S_{\alpha}^{\dagger}\left(\Omega\right)-S_{\alpha}^{\dagger}\left(\Omega\right)S_{\beta}\left(\Omega\right)\rho\left(t\right)\right]+\mathrm{H.c.}\right\}. \tag{4.50}$$

Now, by introducing

$$\Gamma_{\alpha\beta}\left(\Omega\right)=W_{\alpha\beta}\left(\Omega\right)+W_{\beta\alpha}^{*}\left(\Omega\right), \tag{4.51}$$

which is the full Fourier transform of the correlation function of the reservoir, along with the modified Hamiltonian

$$H'=H_{\mathrm{S}}+\frac{1}{i2\hbar}\sum_{\substack{\alpha\beta\\ \Omega}}\left[W_{\alpha\beta}\left(\Omega\right)-W_{\beta\alpha}^{*}\left(\Omega\right)\right]S_{\alpha}^{\dagger}\left(\Omega\right)S_{\beta}\left(\Omega\right), \tag{4.52}$$

the master equation is cast into its Lindblad form

$$\frac{\mathrm{d}\rho}{\mathrm{d}t}=-\frac{i}{\hbar}\left[H',\rho\left(t\right)\right]+\frac{1}{\hbar^{2}}\sum_{\substack{\alpha\beta\\ \Omega}}\Gamma_{\alpha\beta}\left(\Omega\right)\left[S_{\beta}\left(\Omega\right)\rho\left(t\right)S_{\alpha}^{\dagger}\left(\Omega\right)-\frac{1}{2}\left\{S_{\alpha}^{\dagger}\left(\Omega\right)S_{\beta}\left(\Omega\right),\rho\left(t\right)\right\}\right], \tag{4.53}$$

where the first term appearing in the master equation is responsible for unitary evolution and the second term is a dissipative part with the interactions between the subsystem

and the reservoir encoded through the correlation function of the bath operators.

With the Lindblad form of the master equation now displayed, it is worth reflecting upon its singular merit: it describes the time evolution of the reduced density operator for a small subsystem in contact with a large reservoir without need for the full bipartite density matrix. The operators for the small subsystem are incorporated explicitly, while the reservoir operators play an implicit role as they determine the value of the rate term $\Gamma_{\alpha\beta}(\Omega)$. This is in contrast to the von Neumann equation, which has less practical applicability as it requires a density matrix for the full system.

4.3 Time-reversal-invariant topological junctions in the low-energy limit

Before the master equation technique can be applied to the topological–topological junction introduced in Chapter 3, some preliminaries regarding this junction must first be established. The master equation [Eq. (4.53)] requires a formal operator description for the junction and an effective rate term arising from interactions between the junction and its environment, neither of which have yet been given. In the case of the former, an effective low-energy description will be formulated in terms of the Majorana zero modes which reside at a topological Josephson junction. Additionally, we shall briefly investigate the effects of finite nanowires on the junction energy. For the latter, bath operators are physically motivated from an electron-phonon coupling originating from spatial vibrations at the junction. Then, by considering a general time-reversal-invariant perturbation to this junction, a phenomenological method is employed with a constant rate term for the dissipative terms in the master equation, allowing for parity-preserving transitions which lower the total junction energy. Equipped with both of these preliminaries, the master equation is then ready to be applied to examine how the relaxation regime, discussed earlier in Sec. 3.5.1.2, can be set up for the topological Josephson junction.

4.3.1 The electron operator

Prior to the consideration of topological junctions with time-reversal symmetry, we examine the spinless case for simplicity. Such an example will serve to illustrate clearly how the phase difference across a junction manifests in terms of the electron operator.

We therefore take the system described by the Hamiltonian in Eq. (1.20) with the antiunitary operator as defined in Eq. (1.22) and eigenexpansion given by Eqs. (1.27)–(1.30b), where we take the operators to have an explicit dependence on the position x. Suppose that the Bogoliubov–de Gennes Hamiltonian [Eq. (1.21)] described a superconductor with zero phase $H_{\mathrm{BdG}}(0)$ and the following eigenexpansion was also taken at zero phase. A nonzero phase can be incorporated in terms of $H_{\mathrm{BdG}}(0)$ through the gauge transformation

$$H_{\mathrm{BdG}}(\phi) = \Phi^{\dagger}(\phi) H_{\mathrm{BdG}}(0) \Phi(\phi), \tag{4.54}$$

where

$$\Phi(\phi) = \begin{bmatrix} e^{i\phi/2}\mathbb{1}_{2N} & 0 \\ 0 & e^{-i\phi/2}\mathbb{1}_{2N} \end{bmatrix}. \tag{4.55}$$

The phase may be absorbed into the definition of the electron operators via

$$\begin{bmatrix} \tilde{\mathbf{c}} \\ \tilde{\mathbf{c}}^{\dagger} \end{bmatrix} = \Phi \begin{bmatrix} \mathbf{c} \\ \mathbf{c}^{\dagger} \end{bmatrix}, \tag{4.56}$$

so that the BCS Hamiltonian reads

$$H = \frac{1}{2} \begin{bmatrix} \tilde{\mathbf{c}}^{\dagger} & \tilde{\mathbf{c}} \end{bmatrix} H_{\mathrm{BdG}}(0) \begin{bmatrix} \tilde{\mathbf{c}} \\ \tilde{\mathbf{c}}^{\dagger} \end{bmatrix} \tag{4.57}$$

and since this is formally the same as the Hamiltonian in Eq. (1.21), the eigenexpansion detailed in Eqs. (1.27)–(1.30b) applies. Therefore, by introducing the vector containing

the eigenoperators,

$$\boldsymbol{\alpha}_{\pm E} = \begin{bmatrix} \alpha_{\pm E_1} \\ \vdots \\ \alpha_{\pm E_{2N}} \end{bmatrix}, \tag{4.58}$$

the eigenexpansion gives

$$\begin{bmatrix} \tilde{\mathbf{c}} \\ \tilde{\mathbf{c}}^\dagger \end{bmatrix} = U \begin{bmatrix} \boldsymbol{\alpha}_E \\ \boldsymbol{\alpha}_{-E} \end{bmatrix} \tag{4.59}$$

so that the electron operators can be written with respect to the eigenoperators

$$\begin{aligned} \tilde{c}_n &= \sum_j \psi_{E_j,n} \alpha_{E_j} \\ &= \sum_{E_j>0} \left(\psi_{E_j,n} \alpha_{E_j} + \hat{\sigma}_1 \psi^*_{E_j,n} \alpha^\dagger_{E_j} \right) \equiv c_{n,\phi=0}, \end{aligned} \tag{4.60}$$

where $\psi_{E_j,n}$ is the n^{th} element in the vector ψ_{E_j} (with n labelling, e.g., lattice sites) and the equivalency with $c_{n,\phi=0}$ follows since we have used the same eigenexpansion as in the case with $\phi = 0$. Moreover, the original electron operators can be expressed via

$$\begin{bmatrix} \mathbf{c} \\ \mathbf{c}^\dagger \end{bmatrix} = \Phi^\dagger U \begin{bmatrix} \boldsymbol{\alpha}_E \\ \boldsymbol{\alpha}_{-E} \end{bmatrix}, \tag{4.61}$$

so that the phase dependence emerges in the electron operators as [118]

$$c_n = e^{-i\phi/2} c_{n,\phi=0}. \tag{4.62}$$

Now, consider a junction between two superconductors that meet at $x = 0$ with corresponding phases $\phi_{\text{L/R}}$. The Hamiltonian for such a system can be decomposed into left and right superconducting wires with respective Hamiltonians H_{L} and H_{R}, along with

a tunnelling term H_{t} at the contact, i.e.

$$H = H_{\mathrm{L}} + H_{\mathrm{R}} + H_{\mathrm{t}}, \tag{4.63}$$

where

$$H_{\mathrm{t}} = \lambda c_{\mathrm{R}}^{\dagger} c_{\mathrm{L}} + \lambda^{*} c_{\mathrm{L}}^{\dagger} c_{\mathrm{R}} \tag{4.64}$$

with hopping term λ and fermion operators $c_{\mathrm{L/R}}$ which are the the left/right electron operators at the junction. The phase difference $\phi = \phi_{\mathrm{R}} - \phi_{\mathrm{L}}$ between the superconductors is a gauge-invariant quantity and can be seen to enter by the substitution of the type of operators appearing in Eq. (4.62),

$$H_{\mathrm{t}} = \lambda e^{i\phi/2} c_{\mathrm{R},\phi=0} c_{\mathrm{L},\phi=0} + \lambda^{*} e^{-i\phi/2} c_{\mathrm{L},\phi=0} c_{\mathrm{R},\phi=0}. \tag{4.65}$$

Finally, a low-energy approximation can be made through

$$c_{\mathrm{L/R}} \mapsto e^{-i\phi_{\mathrm{L/R}}/2} \gamma_{L/R} \tag{4.66}$$

where $\gamma_{L/R}$ are the operators for the left/right Majorana modes at the junction and where, due to the exponential suppression of their wavefunctions in the inter-Majorana distance, it has been assumed that the Majorana modes at the edges furthest from the junction do not contribute [8]. One can therefore write the effective Hamiltonian at low energy as

$$H_{\mathrm{eff}} = \lambda e^{i\phi/2} \gamma_{\mathrm{R}} \gamma_{\mathrm{L}} + \lambda^{*} e^{-i\phi/2} \gamma_{\mathrm{L}} \gamma_{\mathrm{R}}. \tag{4.67}$$

4.3.2 Topological junctions with Majorana–Kramers pairs

We now consider time-reversal-invariant junctions between topological superconductors which have finite length. In such a setup [Fig. 4.1], each wire hosts a Kramers pair of

Majorana modes per boundary. The Majorana modes at the edges furthest from the junction are labelled by η, while those residing at the junction are labelled by γ, and the respective time-reversed partners are indicated with a tilde. By working at energies much below the gap and to first order in the tunnelling [Eq. (4.66)], couplings may be expressed solely in terms of the Majorana–Kramers pairs at each edge. In what follows, only those couplings between Majorana modes of the same wire $V_{\mathrm{L/R}}$ and those across the junction V_{C} are taken into consideration.

Tunnel couplings between the Majorana modes must be represented by quaternion-real matrices as a result of time-reversal symmetry [Eq. (2.34)]. We therefore parameterise the couplings as

$$V_{\mathrm{L/C/R}} = \begin{bmatrix} 0 & \nu_{\mathrm{L/C/R}} \\ \nu_{\mathrm{L/C/R}}^{\dagger} & 0 \end{bmatrix}, \tag{4.68}$$

where

$$\nu_{\mathrm{L/C/R}} = A_{\mathrm{L/C/R}} \left(a_0^{\mathrm{L/C/R}} \mathbb{1}_2 + i \sum_{k=1}^{3} a_k^{\mathrm{L/C/R}} \sigma_k \right), \tag{4.69}$$

with $A_{\mathrm{L/C/R}} \in \mathbb{R}$ and $a_\mu^{\mathrm{L/C/R}} \in \mathbb{R}$ for $\mu = 0, 1, 2, 3$. Furthermore, choosing $\sum_{\mu=0}^{4} \left(a_\mu^{\mathrm{L/C/R}} \right)^2 = 1$ without loss of generality, we can take

$$a_0^{\mathrm{L/C/R}} = \sin\left(\frac{\omega_{\mathrm{L/C/R}}}{2} \right) \cos\left(\alpha_{\mathrm{L/C/R}} \right), \tag{4.70a}$$

$$a_1^{\mathrm{L/C/R}} = \cos\left(\frac{\omega_{\mathrm{L/C/R}}}{2} \right) \cos\left(\beta_{\mathrm{L/C/R}} \right), \tag{4.70b}$$

$$a_2^{\mathrm{L/C/R}} = \sin\left(\frac{\omega_{\mathrm{L/C/R}}}{2} \right) \sin\left(\alpha_{\mathrm{L/C/R}} \right), \tag{4.70c}$$

$$a_3^{\mathrm{L/C/R}} = \cos\left(\frac{\omega_{\mathrm{L/C/R}}}{2} \right) \sin\left(\beta_{\mathrm{L/C/R}} \right), \tag{4.70d}$$

where $\omega_{\mathrm{L/C/R}}$, $\alpha_{\mathrm{L/C/R}}$, and $\beta_{\mathrm{L/C/R}}$ are parameters which are analogous to the SU(2) parameterisation in Eq. (3.12).

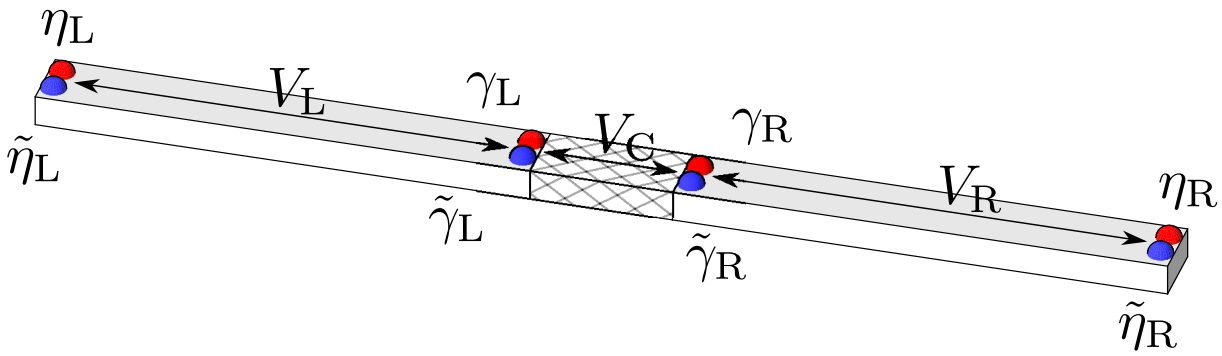

Figure 4.1: The Josephson junction formed between two topological nanowires that have finite length and are connected by a short normal-state bridge (cross-hatched region). Each pair of red and blue hemispheres represents a Majorana–Kramers pair $(\eta_{\mathrm{L/R}}, \tilde{\eta}_{\mathrm{L/R}}, \gamma_{\mathrm{L/R}}, \tilde{\gamma}_{\mathrm{L/R}})$ and the most general case that is considered is with finite couplings between the Majorana–Kramers pairs of the same wire ($V_{\mathrm{L/R}}$), which are responsible for splittings of Majorana modes away from zero energy, and between those in immediate vicinity of the junction (V_{C}).

In terms of the effective coupling matrix

$$M = -2i \begin{bmatrix} e^{i\phi_{\mathrm{L}}/2}\mathbb{1}_4 & 0 \\ 0 & e^{i\phi_{\mathrm{R}}/2}\mathbb{1}_4 \end{bmatrix} \begin{bmatrix} 0 & \nu_{\mathrm{L}} & 0 & 0 \\ \nu_{\mathrm{L}}^\dagger & 0 & \nu_{\mathrm{C}} & 0 \\ 0 & \nu_{\mathrm{C}}^\dagger & 0 & \nu_{\mathrm{R}} \\ 0 & 0 & \nu_{\mathrm{R}}^\dagger & 0 \end{bmatrix} \begin{bmatrix} e^{-i\phi_{\mathrm{L}}/2}\mathbb{1}_4 & 0 \\ 0 & e^{-i\phi_{\mathrm{R}}/2}\mathbb{1}_4 \end{bmatrix}, \tag{4.71}$$

where the factor of $-2i$ has been separated for convenience, the junction Hamiltonian may be written as

$$H = \frac{i}{2} \begin{bmatrix} \hat{\eta}_{\mathrm{L}} & \hat{\gamma}_{\mathrm{L}} & \hat{\gamma}_{\mathrm{R}} & \hat{\eta}_{\mathrm{R}} \end{bmatrix} M \begin{bmatrix} \hat{\eta}_{\mathrm{L}} \\ \hat{\gamma}_{\mathrm{L}} \\ \hat{\gamma}_{\mathrm{R}} \\ \hat{\eta}_{\mathrm{R}} \end{bmatrix} \tag{4.72}$$

where we have used the operator shorthands $\hat{\eta}_{\mathrm{L/R}} = \begin{bmatrix} \eta_{\mathrm{L/R}} & \tilde{\eta}_{\mathrm{L/R}} \end{bmatrix}$ and similarly for $\hat{\gamma}_{\mathrm{L/R}}$. Since M is traceless, the Hamiltonian may be rewritten by using the anticommutation

properties for Majorana operators [Eq. (1.3)]

$$H = \frac{i}{4}\begin{bmatrix}\hat{\eta}_{\mathrm{L}} & \hat{\gamma}_{\mathrm{L}} & \hat{\gamma}_{\mathrm{R}} & \hat{\eta}_{\mathrm{R}}\end{bmatrix}\left(M - M^{\mathsf{T}}\right)\begin{bmatrix}\hat{\eta}_{\mathrm{L}} \\ \hat{\gamma}_{\mathrm{L}} \\ \hat{\gamma}_{\mathrm{R}} \\ \hat{\eta}_{\mathrm{R}}\end{bmatrix}. \tag{4.73}$$

Now, $M - M^{\mathsf{T}}$ is clearly antisymmetric. Additionally, owing to the Hermiticity of H, $M - M^{\mathsf{T}}$ must also be anti-Hermitian. These two properties together mean that $M - M^{\mathsf{T}}$ is real antisymmetric. Hence the spectral decomposition [Eq. (A.7)] allows the Hamiltonian to be expanded as

$$H = \frac{i}{4}\begin{bmatrix}\hat{\eta}_{\mathrm{L}} & \hat{\gamma}_{\mathrm{L}} & \hat{\gamma}_{\mathrm{R}} & \hat{\eta}_{\mathrm{R}}\end{bmatrix} O^{\mathsf{T}}\begin{bmatrix} i\sigma_2 E_1 & 0 & 0 & 0 \\ 0 & i\sigma_2 E_2 & 0 & 0 \\ 0 & 0 & i\sigma_2 E_3 & 0 \\ 0 & 0 & 0 & i\sigma_2 E_4 \end{bmatrix} O \begin{bmatrix}\hat{\eta}_{\mathrm{L}} \\ \hat{\gamma}_{\mathrm{L}} \\ \hat{\gamma}_{\mathrm{R}} \\ \hat{\eta}_{\mathrm{R}}\end{bmatrix} \tag{4.74}$$

in terms of the Andreev levels E_n and the orthogonal matrix of eigenvectors O. This motivates transformed operators

$$\begin{bmatrix}\Gamma_1 \\ \Gamma_2 \\ \vdots \\ \Gamma_8\end{bmatrix} = O\begin{bmatrix}\hat{\eta}_{\mathrm{L}} \\ \hat{\gamma}_{\mathrm{L}} \\ \hat{\gamma}_{\mathrm{R}} \\ \hat{\eta}_{\mathrm{R}}\end{bmatrix}, \tag{4.75}$$

each of which obeys the Hermiticity condition and anticommutes with the other operators; hence they are Majorana operators. Therefore, the Hamiltonian has been diagonalised

$$H = \frac{i}{2}\sum_{n=1}^{4} E_n \Gamma_{2n-1}\Gamma_{2n} \tag{4.76}$$

or, in terms of fermion operators $d_{mn} = \frac{1}{2}\left(\Gamma_m + i\Gamma_n\right)$,

$$H = \sum_{n=1}^{4} E_n\left(d^{\dagger}_{2n-1,2n} d_{2n-1,2n} - \frac{1}{2}\right). \tag{4.77}$$

In the simplest case where both nanowires can be taken to be effectively infinite

in length, the faraway couplings V_{L} and V_{R} can be neglected. In this case, only four Majorana modes must be considered and the Andreev energies match the form of those derived in the corresponding scattering matrix approach [Eq. (3.22)].

In the case where only one or none of the faraway couplings are neglected, the crossings at zero energy are no longer protected. The Andreev levels at positive energy are given by

$$E_{+} = \sqrt{p_{\pm} \pm' \sqrt{p_{\pm}^2 - A_{\mathrm{L}}^2 A_{\mathrm{R}}^2 \cos^2\left(\frac{\omega_{\mathrm{L}}}{2}\right) \cos^2\left(\frac{\omega_{\mathrm{R}}}{2}\right)}}, \tag{4.78}$$

where

$$p_{\pm} = \frac{1}{2}\left[A_{\mathrm{C}}^2 \cos^2\left(\frac{\phi \pm \omega_{\mathrm{C}}}{2}\right) + A_{\mathrm{L}}^2 \cos^2\left(\frac{\omega_{\mathrm{L}}}{2}\right) + A_{\mathrm{R}}^2 \cos^2\left(\frac{\omega_{\mathrm{R}}}{2}\right)\right] \tag{4.79}$$

and the negative energies follow by particle-hole symmetry. Therefore, the couplings $V_{\mathrm{L/R}}$ are each responsible for a splitting of the Majorana modes away from zero energy. The Andreev and total energies are depicted for junctions between an infinite and a finite nanowire [Fig. 4.2(a)-(b)] and two finite nanowires [Fig. 4.2(c)-(d)].

We note that $\omega_{\mathrm{L/R}} = (2n+1)\pi$, where n is an integer, is equivalent to setting the corresponding $A_{\mathrm{L/R}} = 0$. This is because the component of the Hamiltonian describing couplings between these Majorana modes has terms of the form (for example in the left nanowire)

$$H_{\mathrm{L}} = i2\left[(\eta_{\mathrm{L}}\gamma_{\mathrm{L}} - \tilde{\eta}_{\mathrm{L}}\tilde{\gamma}_{\mathrm{L}})\sin(\beta_{\mathrm{L}}) + (\eta_{\mathrm{L}}\tilde{\gamma}_{\mathrm{L}} + \tilde{\eta}_{\mathrm{L}}\gamma_{\mathrm{L}})\cos(\beta_{\mathrm{L}})\right] A_{\mathrm{L}} \cos\left(\frac{\omega_{\mathrm{L}}}{2}\right). \tag{4.80}$$

Therefore, without loss of generality, the effective length of the nanowire can be controlled by setting $\omega_{\mathrm{L/R}} = 0$ and allowing only $A_{\mathrm{L/R}}$ to vary.

With only one finite nanowire ($A_{\mathrm{R}} = 0$), what would be a crossing between Andreev levels at zero energy in the case with two infinite nanowires is now an anticrossing. Fig. 4.2(b) illustrates that the corresponding total energies fall into two classes distin-

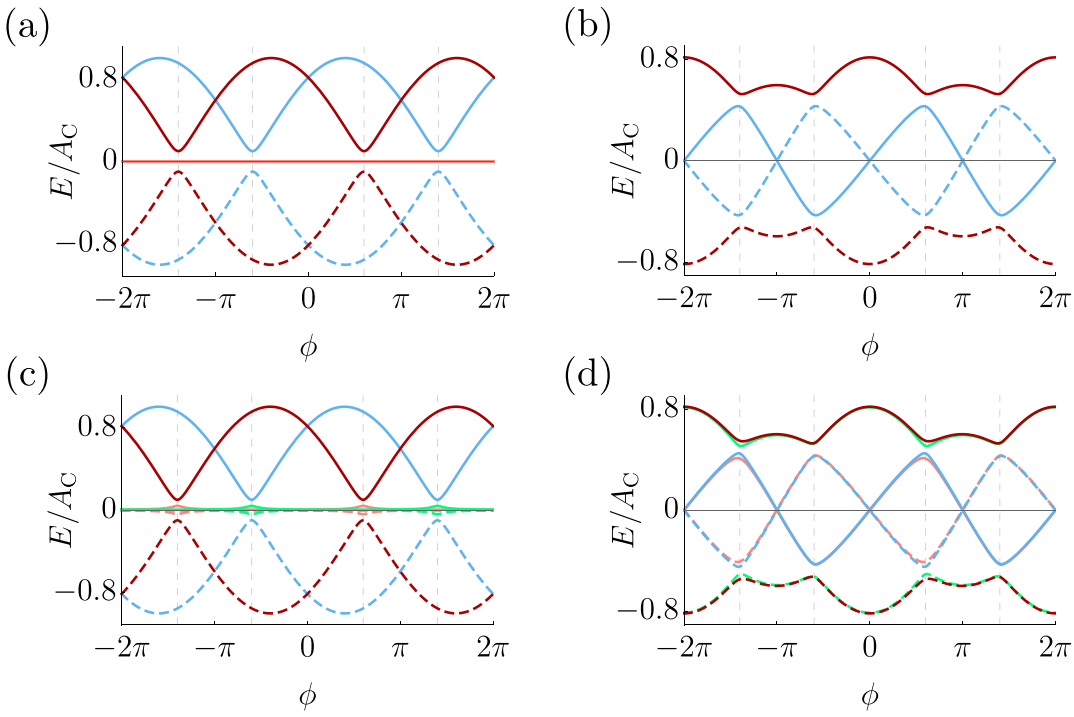

Figure 4.2: Andreev energies (first column) and the possible total energy configurations (second column) for a topological Josephson junction formed of (a)-(b) a finite and an infinite nanowire and (c)-(d) two finite nanowires. For both setups, we take coupling strengths $A_L = 0.1A_C$ with spin-orbit couplings $\omega_L = \omega_R = 0$ and $\omega_C = 0.4\pi$, while for (a)-(b) we take $A_R = 0$ and in (c)-(d) $A_R = 0.05A_C$.

guished by parity. Moreover, when A_L is appreciably smaller than A_C, the configuration with both negative energy levels filled resembles qualitatively the case with both energy and parity relaxation for a junction between effectively infinite nanowires [Fig. 3.6(d)], and in a similar way could allow for the readout of ω_C.

For junctions where both nanowires are finite, the energies do not, provided that $A_R \ll A_c$, differ significantly from the case with a single finite nanowire. Viewing it in terms of the energies of Fig. 4.2(b), the additional coupling serves only to introduce a fine splitting of the total junction energies [Fig. 4.2(d)].

4.3.3 Electron-phonon coupling

In the interest of investigating the energy relaxation regime with parity conservation described in Sec. 3.5.1.2, we now focus on the system between two infinite nanowires

where the crossing at $E = 0$ is protected, setting $A_{\mathrm{C}} = 1$ for brevity in the equations to follow for the remainder of this chapter. While an explicit low-energy Hamiltonian has been provided for the junction, how a reservoir can couple to the junction has yet to be motivated. We provide reasoning for this junction–reservoir interaction below.

The system can be taken to be coupled to a bath of harmonic oscillators by allowing for phonon modes which arise as a result of vibrations at either side of the junction, so that there are displacements

$$x_n \sim \left(b_n + b_n^\dagger\right) / \sqrt{\omega_n} \tag{4.81}$$

in terms of boson operators b_n with associated frequencies ω_n. In this way, the quaternionic parameters a_μ of Eq. (4.69) (where we now drop the superscript L/C/R) are made displacement-dependent via

$$a_\mu \mapsto a_\mu\left(x_n\right) \approx a_\mu\left(0\right) + \sum_n g_n x_n \tag{4.82}$$

where $a_\mu\left(0\right)$ is the value of the parameter when the displacement from equilibrium is zero, $g_n \in \mathbb{R}$ is the electron-phonon coupling parameter which is taken to be independent of μ for simplicity, and the displacements are assumed to be small so that only terms up to the first order in x_n are kept. Taking the part of the Hamiltonian in Eq. (4.73) that involves the Majorana modes residing at the junction, the unperturbed Hamiltonian takes the form

$$\begin{aligned} H_0 = i \Bigg[& a_0 \sin\left(\frac{\phi}{2}\right)\left(\gamma_{\mathrm{R}}\gamma_{\mathrm{L}} + \tilde{\gamma}_{\mathrm{R}}\tilde{\gamma}_{\mathrm{L}}\right) - a_3 \cos\left(\frac{\phi}{2}\right)\left(\gamma_{\mathrm{R}}\gamma_{\mathrm{L}} - \tilde{\gamma}_{\mathrm{R}}\tilde{\gamma}_{\mathrm{L}}\right) \\ & - a_1 \cos\left(\frac{\phi}{2}\right)\left(\gamma_{\mathrm{R}}\tilde{\gamma}_{\mathrm{L}} + \tilde{\gamma}_{\mathrm{R}}\gamma_{\mathrm{L}}\right) - a_2 \sin\left(\frac{\phi}{2}\right)\left(\gamma_{\mathrm{R}}\tilde{\gamma}_{\mathrm{L}} - \tilde{\gamma}_{\mathrm{R}}\gamma_{\mathrm{L}}\right) \Bigg] \end{aligned} \tag{4.83}$$

and the part associated with the low-energy electron-phonon coupling is

$$\begin{aligned} H_{\text{e-ph}} = i \Bigg[& \sin\left(\frac{\phi}{2}\right)\left(\gamma_{\text{R}}\gamma_{\text{L}} + \tilde{\gamma}_{\text{R}}\tilde{\gamma}_{\text{L}}\right) - \cos\left(\frac{\phi}{2}\right)\left(\gamma_{\text{R}}\gamma_{\text{L}} - \tilde{\gamma}_{\text{R}}\tilde{\gamma}_{\text{L}}\right) \\ & - \cos\left(\frac{\phi}{2}\right)\left(\gamma_{\text{R}}\tilde{\gamma}_{\text{L}} + \tilde{\gamma}_{\text{R}}\gamma_{\text{L}}\right) - \sin\left(\frac{\phi}{2}\right)\left(\gamma_{\text{R}}\tilde{\gamma}_{\text{L}} - \tilde{\gamma}_{\text{R}}\gamma_{\text{L}}\right) \Bigg] \\ & \times \sum_n \frac{g_n}{\sqrt{\omega_n}} \left(b_n + b_n^\dagger\right), \end{aligned} \tag{4.84}$$

which provides a mechanism for energy relaxation with parity conservation.

This type of energy relaxation is incorporated into the master equation by including it as a phenomenological rate term. Such a term must be consistent with time-reversal symmetry, so that transitions occurring between the Kramers degenerate states are forbidden. In order to make the rate term time-reversal-invariant, we take the most general tunnelling perturbation

$$\begin{aligned} H_{\text{e-ph}} = i \Bigg[& \delta a_0 \sin\left(\frac{\phi}{2}\right)\left(\gamma_{\text{R}}\gamma_{\text{L}} + \tilde{\gamma}_{\text{R}}\tilde{\gamma}_{\text{L}}\right) - \delta a_3 \cos\left(\frac{\phi}{2}\right)\left(\gamma_{\text{R}}\gamma_{\text{L}} - \tilde{\gamma}_{\text{R}}\tilde{\gamma}_{\text{L}}\right) \\ & - \delta a_1 \cos\left(\frac{\phi}{2}\right)\left(\gamma_{\text{R}}\tilde{\gamma}_{\text{L}} + \tilde{\gamma}_{\text{R}}\gamma_{\text{L}}\right) - \delta a_2 \sin\left(\frac{\phi}{2}\right)\left(\gamma_{\text{R}}\tilde{\gamma}_{\text{L}} - \tilde{\gamma}_{\text{R}}\gamma_{\text{L}}\right) \Bigg], \end{aligned} \tag{4.85}$$

which is of the same form as Eq. (4.83) due to time-reversal symmetry. (The displacements x_n are implicit within the parameters δa_j.) By employing the Majorana transformation used in Eq. (4.75) to rewrite the tunnelling perturbation with respect to the fermion operators $d_{12} = \frac{1}{2}\left(\Gamma_1 + i\Gamma_2\right)$ and $d_{34} = \frac{1}{2}\left(\Gamma_3 + i\Gamma_4\right)$ that diagonalise Eq. (4.83), the phase dependence which enforces time-reversal symmetry can be extracted from the off-diagonal (relative to the d_{12} and d_{34} basis) part of the Hamiltonian as these terms describe transitions between Kramers pairs which must vanish at the time-reversal-invariant phases. We outline the procedure for this extraction now.

The orthogonal matrix of eigenvectors [from the transformation in Eq. (4.75)] can

be chosen as

$$O = \begin{bmatrix} 0 & 0 & \nu_+ & \nu_- \\ \mu_- & \mu_+ & 0 & 0 \\ 0 & 0 & -\nu_- & \nu_+ \\ -\mu_+ & \mu_- & 0 & 0 \end{bmatrix} \tag{4.86}$$

where

$$\mu_\pm = \sin\left(\frac{\alpha+\beta}{2} \pm \pi/4\right), \qquad \nu_\pm = \sin\left(\frac{\alpha-\beta}{2} \pm \pi/4\right) \tag{4.87}$$

with α and β coming from the real quaternionic parameterisation used in Eq. (4.70). The unperturbed Hamiltonian is diagonalised by this transformation such that

$$H_0 = 4\left[-\cos\left(\frac{\phi-\omega}{2}\right)\left(d_{12}^\dagger d_{12} - \frac{1}{2}\right) + \cos\left(\frac{\phi+\omega}{2}\right)\left(d_{34}^\dagger d_{34} - \frac{1}{2}\right)\right]. \tag{4.88}$$

Now, we treat the electron-phonon part: substituting Eq. (4.75) into Eq. (4.85) and then regrouping in terms of the fermion operators d_{mn} yields

$$\begin{aligned} H_{\text{e-ph}} = 4\Bigg[& (\nu_+\mu_-\zeta_{03-} + \nu_-\mu_+\zeta_{03+} - \nu_+\mu_+\zeta_{21+} + \nu_-\mu_-\zeta_{21-})\left(d_{12}^\dagger d_{12} - \frac{1}{2}\right) \\ & + (\nu_-\mu_-\zeta_{03+} - \nu_+\mu_+\zeta_{03-} - \nu_+\mu_-\zeta_{21+} - \nu_-\mu_+\zeta_{21-})\left(d_{14}^\dagger d_{14} - \frac{1}{2}\right) \\ & + (\nu_-\mu_-\zeta_{03-} - \nu_+\mu_+\zeta_{03+} - \nu_-\mu_+\zeta_{21+} - \nu_+\mu_-\zeta_{21-})\left(d_{23}^\dagger d_{23} - \frac{1}{2}\right) \\ & + (\nu_-\mu_+\zeta_{03-} + \nu_+\mu_-\zeta_{03+} + \nu_-\mu_-\zeta_{21+} - \nu_+\mu_+\zeta_{21-})\left(d_{34}^\dagger d_{34} - \frac{1}{2}\right)\Bigg] \end{aligned} \tag{4.89}$$

where

$$\zeta_{ij\pm} = \delta v_i \sin\left(\frac{\phi}{2}\right) \pm \delta v_j \cos\left(\frac{\phi}{2}\right). \tag{4.90}$$

Recall that the fermion operators d_{12} and d_{34} span the Hilbert space of the four Majorana operators. The d_{14} and d_{23} that appear in Eq. (4.89) provide an alternative pairing of these operators and thus are not independent from d_{12} and d_{34}. Specifically, they can be

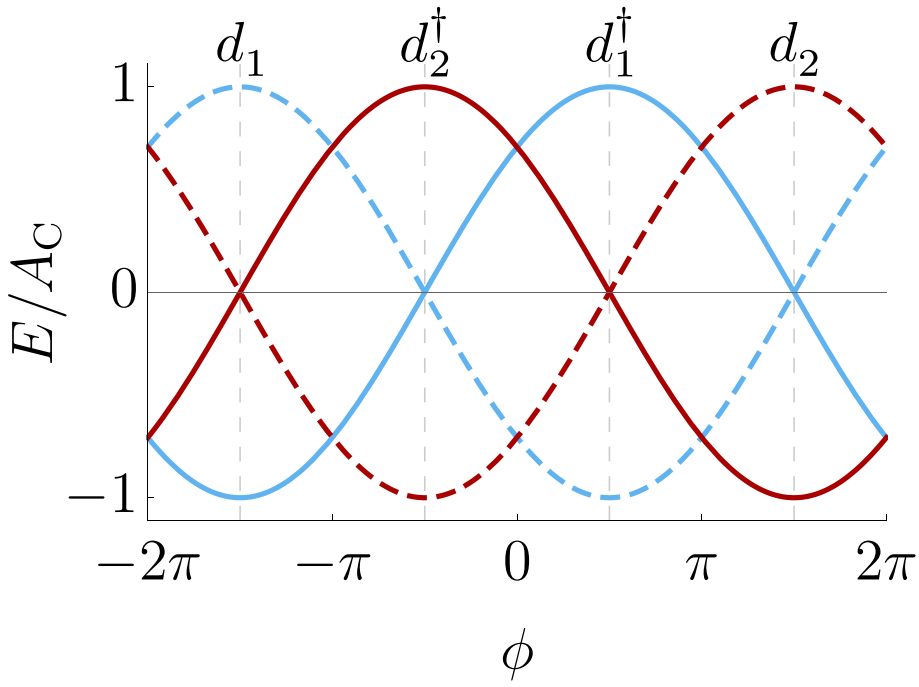

Figure 4.3: Andreev levels for a Josephson junction between topological superconductors, where the spin-orbit parameter has been set to $\omega = \pi/2$. Each Andreev level has been labelled with its respective operator, illustrating that the operators can be associated with either adding or removing a level at positive energy depending on the value of the phase difference ϕ.

represented through

$$d_{14}^\dagger d_{14} - \frac{1}{2} = \frac{1}{2}\left(d_{12}d_{34} - d_{12}d_{34}^\dagger + d_{12}^\dagger d_{34} - d_{12}^\dagger d_{34}^\dagger\right), \tag{4.91a}$$

$$d_{23}^\dagger d_{23} - \frac{1}{2} = \frac{1}{2}\left(d_{12}d_{34} + d_{12}d_{34}^\dagger - d_{12}^\dagger d_{34} - d_{12}^\dagger d_{34}^\dagger\right). \tag{4.91b}$$

For clarity, we relabel the fermion operators via $d_1 = d_{12}$ and $d_2 = d_{34}^\dagger$. The off-diagonal component of the Hamiltonian then reads

$$\begin{aligned} H_{\text{off-diag}} = -\frac{1}{4}\Big\{ &\left[\delta v_0 \sin(\alpha) - \delta v_2 \cos(\alpha)\right] \sin\left(\frac{\phi}{2}\right)\left(d_1 d_2^\dagger - d_1^\dagger d_2\right) \\ &+ \left[\delta v_3 \cos(\beta) - \delta v_1 \sin(\beta)\right] \cos\left(\frac{\phi}{2}\right)\left(d_1 d_2 - d_1^\dagger d_2^\dagger\right)\Big\}, \end{aligned} \tag{4.92}$$

which includes a phase dependence that must be obeyed as a result of time-reversal symmetry. In interpreting Eq. (4.92), it is useful to note that if one were to intuitively

think of the $d^\dagger$ operators as adding Andreev levels at $E > 0$ and the d operators as removing levels at $E > 0$, the second line of Eq. (4.92) would seem to describe processes unrelated to transitions between branches, while the first line would describe transitions between branches but would allow them to happen at half of the time-reversal-invariant phases. Kramers degeneracy, however, forbids branch transitions at all time-reversal-invariant phases. The resolution to this inconsistency lies in the Andreev crossing at zero energy: the operator $d^\dagger$ can describe either the addition or removal of an Andreev level at $E > 0$ depending on the value of ϕ. Following the labelling in Fig. 4.3, it is clear that the terms associated with a transition within the even parity sector (i.e. $d_1 d_2$ and $d_1^\dagger d_2^\dagger$) must vanish at $\phi = (2n+1)\,\pi$ where n is an integer, while the terms associated with a transition within the odd parity sector (i.e. $d_1 d_2^\dagger$ and $d_1^\dagger d_2$) must vanish at $\phi = 2n\pi$. The phase-dependent coefficient that appears with each operator combination precisely ensures this, i.e. transitions between Kramers pairs at the time-reversal-invariant phases are forbidden as they should be.

4.4 Master equation approach

Having formulated the low-energy description of the topological Josephson junction and motivated an environmental bath, we now focus on utilising the master equation approach in order to investigate the Andreev level occupancies in terms of the phase sweep speed and a generic time-reversal-invariant relaxation rate. Before proceeding directly to the master equation, it is first necessary to make clear how the phase sweep arises.

4.4.1 Time-dependent Hamiltonian description

The effect of a phase sweep may be incorporated by considering a constant voltage V_0 across the junction at $x = 0$

$$V(x) = \frac{V_0}{2}\,\mathrm{sgn}\,(x)\,, \tag{4.93}$$

which, by the Josephson relation, is expressible in terms of a linear phase sweep

$$eV(x) = \frac{\hbar}{4}\frac{\mathrm{d}\phi}{\mathrm{d}t}\operatorname{sgn}(x). \tag{4.94}$$

The time-dependent Bogoliubov–de Gennes equations give

$$[H(\phi) + eV(x)\sigma_3]|\psi\rangle = i\hbar\partial_t|\psi\rangle, \tag{4.95}$$

where σ_3 is the third Pauli matrix in particle-hole space. By expanding into an instantaneous Fock eigenbasis [119]

$$|\psi\rangle = \sum_n c_n(t)|n(\phi)\rangle, \tag{4.96}$$

we convert Eq. (4.95) into a matrix form relative to the vector of time-dependent coefficients $\mathbf{c}(t)$

$$\hat{H}\mathbf{c} = i\hbar\partial_t\mathbf{c}. \tag{4.97}$$

By inserting Eq. (4.96) into Eq. (4.95) and rearranging into the form presented in Eq. (4.97), we have

$$\sum_n \left[E_n\delta_{mn} + \hbar\frac{\mathrm{d}\phi}{\mathrm{d}t}\left\langle m(\phi)\left|\frac{\sigma_3\operatorname{sgn}(x)}{4} - i\partial_\phi\right|n(\phi)\right\rangle\right] = i\hbar\sum_n \partial_t c_n(t)\delta_{mn} \tag{4.98}$$

so that a general element of the Hamiltonian $\hat{H}$ is given by

$$\hat{H}_{mn} = E_m(\phi)\delta_{mn} + \hbar\frac{\mathrm{d}\phi}{\mathrm{d}t}M_{mn}(\phi), \tag{4.99}$$

where $E_m(\phi)$ is an instantaneous Andreev energy and

$$M_{mn}(\phi) = \left\langle m\left|\frac{\sigma_3\operatorname{sgn}(x)}{4} - i\partial_\phi\right|n\right\rangle \tag{4.100}$$

are the connections between instantaneous eigenstates of the Bogoliubov–de Gennes Hamiltonian [108].

4.4.2 Lindblad equation

The master equation in its Lindblad form [Eq. (4.53)] can now be employed to describe the topological junction between two effectively infinite nanowires. We assume that the continuum is well-separated from the Andreev levels, such that the effects of the continuum can be neglected in what follows. The master equation takes the form

$$\begin{aligned}\frac{\mathrm{d}\rho}{\mathrm{d}t} = -\frac{i}{\hbar}\left[H,\rho\right] + \frac{\Gamma_{\mathrm{r}}}{\hbar^2}\Bigg\{&\left[\xi_{\mathrm{c}+}\left(\phi\right)\chi(d_1 d_2)\left\{\rho\right\} - \xi_{\mathrm{c}-}\left(\phi\right)\chi(d_1^\dagger d_2^\dagger)\left\{\rho\right\}\right]\cos\left(\frac{\phi}{2}\right)\\ &+\left[\xi_{\mathrm{s}+}\left(\phi\right)\chi(d_1 d_2^\dagger)\left\{\rho\right\} - \xi_{\mathrm{s}-}\left(\phi\right)\chi(d_1^\dagger d_2)\left\{\rho\right\}\right]\sin\left(\frac{\phi}{2}\right)\Bigg\}.\end{aligned} \tag{4.101}$$

The first term is unitary with its Hamiltonian given in terms of the low-energy Andreev levels of Eq. (4.77), the sweep speed v_{s}, and the connections $M_{mn}\left(\phi\right)$, with the overall form

$$H = \sum_{n=1}^{2} E_n\left(d_n^\dagger d_n - \frac{1}{2}\right) + \hbar v_{\mathrm{s}}\sum_{mn=-2}^{2} M_{mn}\left(\phi\right) d_m^\dagger d_n. \tag{4.102}$$

The second term of the master equation is dissipative, allowing for transitions with phenomenological rate constant Γ_{r} which lower the total energy of the junction within each fermion parity sector. The superoperator

$$\chi\left(O\right)\left\{\rho\right\} = O\rho O^\dagger - \frac{1}{2}\left\{O^\dagger O,\rho\right\} \tag{4.103}$$

describes general dissipations of the Lindblad type associated with the operator O and the phase-dependent terms

$$\xi_{\mathrm{c}\pm} = \frac{1 \pm \mathrm{sgn}\left[\cos\left(\frac{\phi}{2}\right)\right]}{2}, \tag{4.104a}$$

$$\xi_{\mathrm{s}\pm} = \frac{1 \pm \mathrm{sgn}\left[\sin\left(\frac{\phi}{2}\right)\right]}{2}, \tag{4.104b}$$

ensure that the transitions associated with χ are dissipative, while the operator combinations and the rest of the phase dependence are informed from general considerations of time-reversal symmetry [Eq. (4.92)].

4.4.2.1 Zero sweep speed

It is convenient to first consider the case where the phase is not swept along ($v_{\mathrm{s}} = 0$). The reason for this is twofold: firstly, it will allow for a straightforward determination of whether or not the junction tends towards the regime characterised by energy relaxation and fermion parity conservation; secondly, it enables us to monitor how relaxation processes work in isolation of any complications that could be introduced by a finite phase sweep.

We assume that the junction has been initially prepared with negative total energy at $\phi = -2\pi$ for both fermion parity classes. We numerically solve the master equation for phases $\phi \in [-2\pi, 2\pi]$, which connect smoothly (i.e. without branch switches) to the negative energy at $\phi = -2\pi$, with $\hbar\Gamma_{\mathrm{r}} = 10^{-2} A_{\mathrm{C}}$ and obtain the junction energy through $\langle E(\phi) \rangle = \mathrm{tr}\left[\rho(t) H(\phi)\right]$ for various times t. We find that the junction converges with increasing time from the initial 4π periodic state towards the 2π periodic state with crossings at the relevant time-reversal-invariant phases (i.e. where the total junction energy is zero for a particular parity class), demonstrating that the regime with energy relaxation and parity conservation, which was first described in Sec. 3.5, is accessible.

Total junction energies with $\omega = 0.4\pi$ for various times are illustrated in Fig. 4.4(a)-(f), along with the Andreev occupancies of the state that is being converged to for each

respective parity class in Fig. 4.4(g)-(h). These results show that, as a consequence of the transitions at the Kramers degeneracies being forbidden, the energy relaxes the more swiftly the further the phase is from the relevant time-reversal-invariant phases, resulting in maximally effective relaxations at $\phi = (2n + p)\pi$ where $p = 0, 1$ is the fermion parity of the junction.

4.4.2.2 Finite sweep speed

We now allow for a finite phase sweep speed ($v_\mathrm{s} > 0$) and consider junctions which are, again, initially prepared at $\phi = -2\pi$ with negative total energy for a particular fermion parity class. For clarity, we employ $\phi' \equiv [\phi \pmod{4\pi}] - 2\pi$. For relaxation rates that are sufficiently strong relative to the phase sweep speed, we find that the system approximates to a good degree the regime with energy relaxation and fermion parity conservation, with exact matching as $\hbar\Gamma_\mathrm{r}/v_\mathrm{s} \mapsto \infty$.

Examples of the Josephson current are demonstrated in Fig. 4.5, where the ratio $\hbar\Gamma_\mathrm{r}/v_\mathrm{s}$ is varied for even and odd fermion parities and the corresponding current-phase relations are displayed for late times when an equilibrium has been reached. For sufficiently large $\hbar\Gamma_\mathrm{r}/v_\mathrm{s}$, we note that the switchlike features at $\phi' = (2n + 1 + p)\pi$ associated with this regime are recovered, while they become more smoothed out away from this limit. As was highlighted in Sec. 3.5.1.5, these switches are topological in origin. With regard to their observation in experiment, we suggest that, provided external processes which flip fermion parity can be controlled for, it is most judicious to work with sufficiently slow v_s (i.e. for small applied voltages) in order to preserve these switchlike features.

Moreover, transitions at $\phi = (2n + 1 + p)\pi$ are forbidden as a result of time-reversal symmetry, and, as was observed in the case with no phase sweep, relaxations happen at a slower effective rate the nearer they are to these points. This effect is exacerbated by the fact that v_s is now finite—while for long enough times with $v_\mathrm{s} = 0$ and $\Gamma_\mathrm{r} > 0$, convergence to a pure state was guaranteed, this is no longer necessarily true with $|v_\mathrm{s}| > 0$.

This can be shown directly by comparison with a phenomenological relaxation term

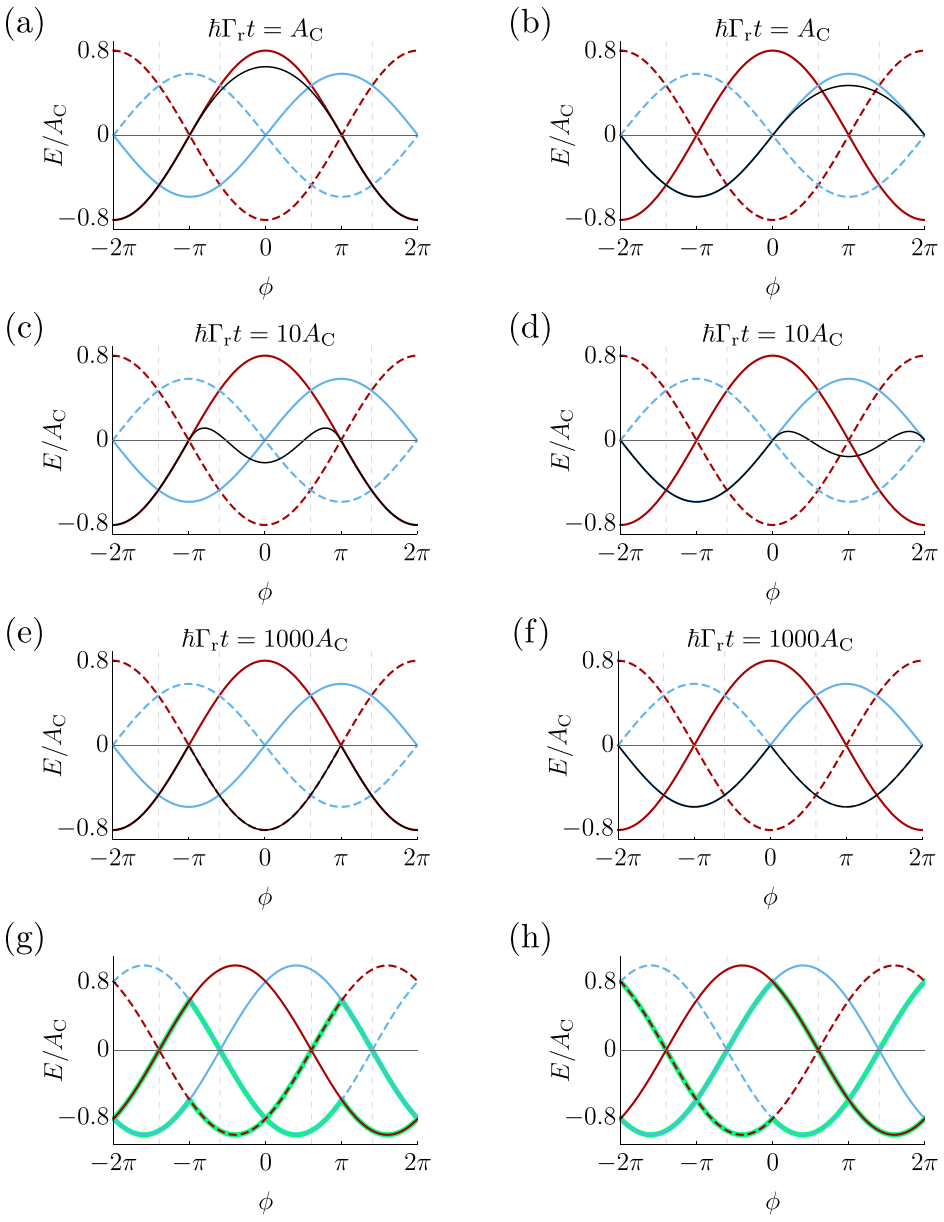

Figure 4.4: (a)-(f) Total junction energies at various times t for a Josephson junction between topological superconductors with $\omega = 0.4\pi$, where the blue and red curves represent odd and even fermion parities, respectively, and the black curves represent the expected value of the energy. The junction is initially prepared for a phase ϕ which smoothly connects (i.e. without branch switches) to the negative energy state at $\phi = -2\pi$, with an even fermion parity for the first column and an odd fermion parity for the second column. For (g)-(h), the Andreev levels and occupancies (highlighted in green) of the energy being converged to are displayed.

which does not respect time-reversal symmetry, where the time-reversal-invariant rate is found to be slower than its time-reversal-broken counterpart [Fig. 4.6]. Moreover,

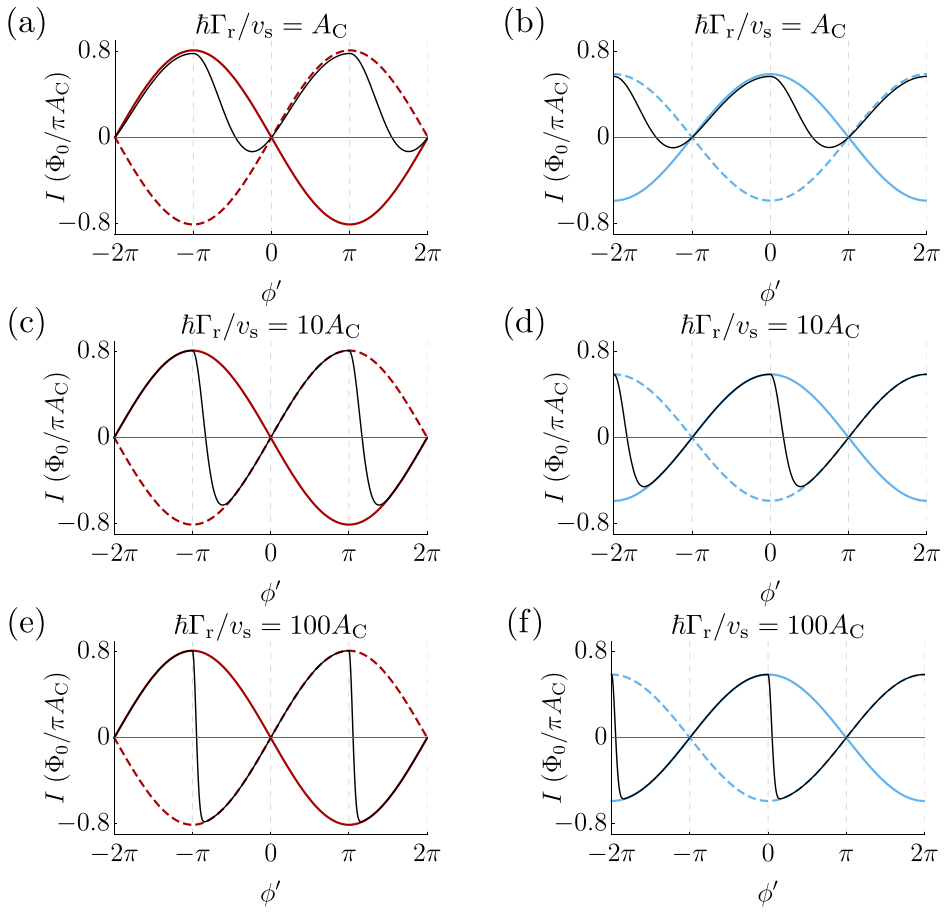

Figure 4.5: The subgap current for a Josephson junction between topological superconductors with $\omega = 0.4\pi$ and for various relaxation rates Γ_r and phase sweep speeds v_s. The junction is initially prepared with negative total energy at $\phi = -2\pi$ for even fermion parity (left column) and odd fermion parity (right column). Red and blue curves represent, respectively, the even and odd parity currents associated with pure states of the density matrix, while the black curve is the expected value of the current established in the long-time limit.

the time-reversal-broken rate demonstrates that the switchlike features can still be lost, as a result of the finite value of v_s, despite allowing transitions at the time-reversal-invariant phases.Therefore, we can attribute the difficulty of Andreev branch switches to two sources: the finite sweep speed and the transitions forbidden by time-reversal symmetry. This explains a feature illustrated in Fig. 4.6(c)-(f), where the maximum in energy at $\phi = \pm\pi$ is more skewed in the direction of the phase sweep for the time-reversal-invariant case than in the time-reversal-broken case; this extra skewness arises from the additional difficulty in switching due to the forbidden transitions near the Kramers degeneracies.

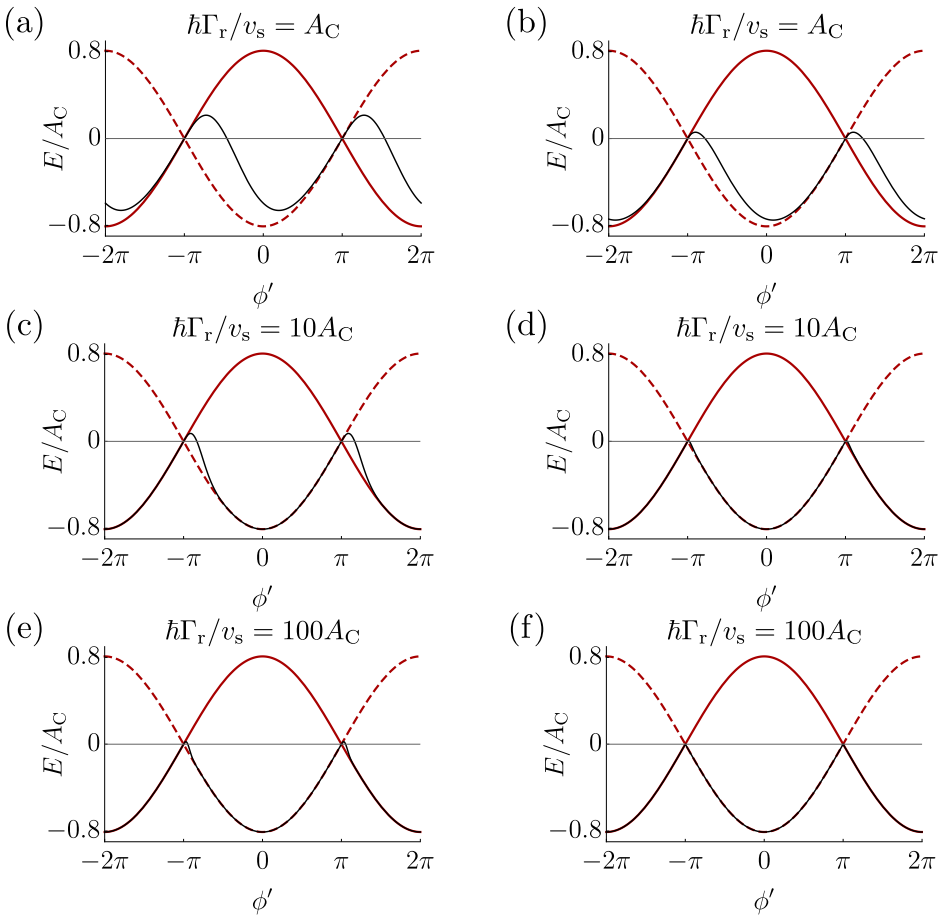

Figure 4.6: Total junction energies for a Josephson junction between topological superconductors with $\omega = 0.4\pi$ for various relaxation rates Γ_r and phase sweep speeds v_s, comparing rates which respect time-reversal symmetry (left column) and those that break time-reversal symmetry (right column). The junction energies associated with even parity pure states of the density matrix are depicted by the red curves, while the black curves represent the expected total energy of the impure state in the long-time limit.

When the ratio $\hbar\Gamma_r/v_s$ is sufficiently small and the junction is initialised according to the usual preparatory protocol, the 4π periodicity of the Josephson current can be maintained for the initial periods [Fig. 4.7(a)-(b)]. However, over numerous cycles the weak relaxation rate eventually suppresses the total junction energy such that it becomes 2π periodic with a severely diminished magnitude [Fig. 4.7(c)-(d)]. This can be understood intuitively. Since the phase sweep is so much faster than the relaxation rate, the junction spends approximately half of its time with positive total energy and the other half with negative total energy. The relaxation processes act slowly such that the total energy over

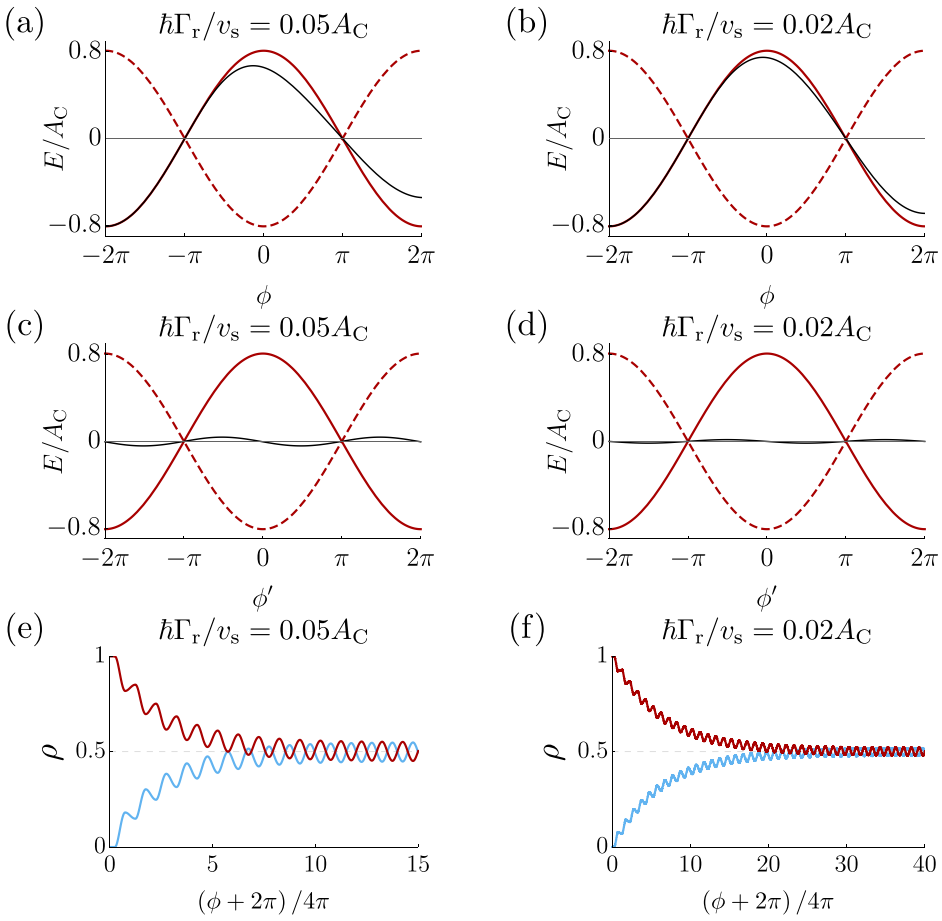

Figure 4.7: Total energies and occupancies for a Josephson junction between topological superconductors with $\omega = 0.4\pi$ where the relaxation rate Γ_r is significantly smaller than the phase sweep speed v_s. The junction is initially prepared with even fermion parity and with negative total energy at $\phi = -2\pi$. The total energy of the initial phase sweep is shown in (a)-(b), while the state it eventually converges to after many cycles is depicted in (c)-(d). For (e)-(f), the occupancies of the two states with even fermion parity are shown, starting from the initial phase sweep.

the positive sector is only slightly diminished after each cycle. Over many cycles, this results in the occupancies of the relevant levels having a small oscillation about a half-filling for each level where the magnitude of the oscillations is related to the magnitude of the ratio $\hbar\Gamma_r/v_s$. These occupancies are illustrated with respect to the finite density matrix elements for a junction initially prepared with even fermion parity in Fig. 4.7(e)-(f).

4.5 Conclusion

Previously, in Chapter 3, we provided a theory for the current-phase relationship for mesoscopic junctions involving time-reversal-invariant topological superconductors in terms of a small number of experimentally accessible parameters. With regard to a finite phase sweep (i.e. through the ac Josephson effect $\dot{\phi} = 2eV/\hbar$), we identified, in addition to the fractional ac Josephson effect, two distinct regimes characterised by strong energy relaxation and distinguished by whether or not they allow for external processes which violate the conservation of fermion parity. A key feature of both these regimes is the emergence of current switches which potentially serve as indicators of the junction's nontrivial topology.

In conjunction with these exact results, we have utilised a master equation approach and studied the topological–topological junction in an effective low-energy limit in order to investigate, in further detail, junctions with energy relaxation and parity conservation. We find that such a setup can be accessed upon the incorporation of a time-reversal-invariant phenomenological relaxation rate which can arise through an electron-phonon coupling due to vibrations at either side of the junction.

A transient 4π periodic Josephson effect was found to exist for relaxation rates Γ_{r} which were sufficiently slow with respect to the phase sweep speed v_{s} and where the junction had been initially prepared with a particular fermion parity with minimum energy at a given ϕ. However, over many phase sweep cycles, the small nonzero Γ_{r} leads to a nearly even filling, within that fermion parity class, between the positive and negative Andreev levels, eventually resulting in a greatly diminished current magnitude and a 2π periodicity. This suggests that, even for small Γ_{r}, the 4π periodic Josephson effect will not persist indefinitely and its observation is limited to the initial phase sweep cycles.

In contrast, a regime analogous to the one discussed in Sec. 3.5.1.2 can be established permanently provided that fermion parity is conserved. The adherence to this regime is found to be most strict when the ratio of Γ_{r} to v_{s} is appreciably large. Regarding measurable topological signatures, switchlike features in the current which appear at the time-reversal-invariant phases are established concurrently with this regime. However, the

recovery of switchlike features is found to be hindered not only by the finite value of v_{s}, but also by time-reversal symmetry: transitions between the Kramers degenerate states are forbidden. As concerns the robust detection of these topological features, this suggests that the magnitude of v_{s} should be taken to be as small as possible, while still ensuring that external processes which flip the fermion parity can be consistently controlled for, in order to maximise the visibility of these current switches.

Conclusions

We have studied one-dimensional Josephson junctions involving time-reversal-invariant topological superconductors. As a result of the nontrivial topology of these systems, the superconductors host a single Majorana–Kramers pair at each boundary. The Josephson current that flows across such junctions was found to have conspicuous features associated with the pairs at the junction. By separately applying a scattering matrix technique and a master equation approach, we have made several qualitative and quantitative predictions regarding these junctions which allow, through such supercurrent readouts, for the time-reversal-invariant and topological properties of these junctions to be robustly detected in experiment.

For nontopological Josephson junctions between s-wave superconductors, time-reversal symmetry is known to yield compact relations in terms of the normal-state junction properties [14–19]. Motivated by this, we applied the scattering matrix technique to the topological case in order to obtain the Josephson current,[1] which was found to generally have finite contributions from both the Andreev levels and the continuum, with a small number of independently measurable junction parameters as inputs. While this technique facilitates quantitative comparisons with experimental data, we additionally identified a number of outstanding features which showcase the properties of time-reversal symmetry and topology, occurring in various regimes associated with the ac Josephson effect ($\dot{\phi} = 2eV/\hbar$).

For gap-symmetric junctions between two topological superconductors, the gap pa-

[1] See Ref. [1] of the Publications section at the beginning of this thesis.

rameters were taken to be composed of an admixture between a p-wave component and an s-wave component $\Delta_\pm = \Delta_s \pm \Delta_p$ with $\Delta_- < 0$ for topological superconductors. With respect to the subgap spectrum, Andreev levels were found to approach and escape into the continuum above a critical junction transparency τ_c that is dependent on $\Delta_\pm$; a similar feature arises in the purely s-wave case ($\Delta_+ = \Delta_-$), but only for gap-asymmetric junctions [49]. Moreover, crossings between subgap levels were found to occur in two types. The first is due to time-reversal symmetry, where there are generally crossings at finite energy for phases $\phi = n\pi$ with n integer. The second is related to the presence of Majorana–Kramers pairs at the junction, resulting in zero-energy crossings that occur at phases $\phi_n = \pm\omega + (2n+1)\,\pi$ where ω is the degree of spin-flip scattering.

With respect to the Josephson current, we considered the effect of a voltage bias across the junction, resulting in a finite sweep speed for the phase ($\dot{\phi} = 2eV/\hbar$). When the phase can be swept with fermion parity conservation and no energy relaxation, we found a 4π periodic current-phase relation. This is a time-reversal-invariant generalisation [56, 58] of the fractional ac Josephson effect [6, 50, 51, 70, 71, 92, 93]. This periodicity is twice that of the conventional 2π periodic Josephson effect and is a signature of topological superconductivity. This effect, however, is fragile to processes which lower the total energy of the junction.

By allowing for fermion parity conservation and a fast energy relaxation, a 2π periodic current was found to emerge. In relation to the subgap energy spectrum, branch switches occur at the phases $\phi = (p + 2n + 1)\,\pi$, where p is the fermion parity of the junction, corresponding to switches in the Josephson current where the current flips its sign and maintains its magnitude upon traversing these points. The switches occurring at these phases embody time-reversal symmetry: distinct energy branches must cross at the time-reversal-invariant phases as a result of Kramers' degeneracy theorem, enabling energy-minimising processes to take place in the vicinity of, but not at, these locations. The current switches are most suitable to be attributed to a topological origin when the junction transparency τ is of an intermediate value, as this suppresses any potential

nontopological false positives while maintaining switch visibility.

For both fast fermion parity relaxation and energy relaxation (i.e. the dc Josephson effect), the current was found to be 2π periodic with current switches—which flip sign but do not necessarily preserve magnitude—coincident with the zero-energy Andreev branch crossings. These switches therefore occur in pairs equidistant from $\phi = n\pi$ with a distance set by ω, enabling experimental readouts of ω through the measurement of the distance between current switches. Moreover, these switches can be recognised as of a topological nature for values of ω appreciably far enough away from $n\pi$ or for when τ is far enough away from unity.

As regards junctions between an s-wave superconductor and a topological superconductor, we obtained a number of compact analytical results in relation to the subgap spectrum for various limits involving the superconducting gaps when there is no s-wave admixture present in the topological superconductor. Allowing for a finite s-wave admixture, we generally found there to be two pairs of subgap energies distinguished by their energy magnitude: a high-energy type, extending up to and possibly into the continuum, and a low-energy type with zero-energy crossings concurrent with the time-reversal-invariant phases $\phi = n\pi$.

Upon consideration of a finite phase sweep, the case with fermion parity nonconservation was found to have the clearest signatures of topology. For sufficiently slow phase sweeps, the junction's total energy can be taken to be minimised with switches occurring between the subgap branches at the Kramers degenerate phases. In the Josephson current, these switches between Andreev branches again manifest as switches in the Josephson current and, owing to the time-reversal properties of the spectrum, the current maintains its magnitude after a switch. Moreover, provided that τ is significantly far enough away from unity, these switches are absent in the nontopological variant. Therefore, these current switches can serve as indicators of the nontrivial junction topology.

The effect of a finite phase sweep for junctions between two topological superconductors can be studied in further detail by adopting a master equation approach. By

formulating a low-energy description for these junctions, we investigated the setup characterised by fermion parity conservation and energy relaxation and how it can be realised in terms of a phenomenological relaxation rate. It was argued that this rate could arise from an electron-phonon coupling as a result of, e.g., the spatial vibrations between either end of the junction. Depending primarily on the ratio of the relaxation rate to the phase sweep speed, two types of topologically relevant current-phase relations can occur.

For junctions prepared in a particular fermion parity class with a minimum energy at a given ϕ, the 4π periodic Josephson effect was found, for sufficiently small relaxation rates with respect to the phase sweep speed, to endure over a number of phase sweep cycles. As the relaxation rate is nonzero, however, the Andreev level occupancies tend toward oscillating about a nearly equal filling, ultimately leading to a 2π periodic Josephson effect. Hence the window for the observation of the 4π periodic Josephson effect is limited to the initial cycles, and the phase sweep speed should be taken to be as fast as possible, without introducing unintended Landau-Zener tunnellings, to maximise this window.

Conversely, provided that there are no processes which violate fermion parity conservation, the topological regime with strong energy relaxation can be permanently established. The current switches associated with this regime were found to be reproduced most authentically when the relaxation rate was taken to be considerably faster than the phase sweep speed. This can be understood as the relaxation processes act to minimise the total energy of the junction with respect to the fermion parity, so given that that the phase sweep is slow enough, relaxation processes have enough time to occur after a finite energy branch crossing for switchlike features in the current to be restored. As the phase sweep speed can be directly controlled by the voltage applied across the junction, it is most judicious to work with voltages that are as low in magnitude as possible without compromising the fermion parity of the junction.

Furthermore, we found that time-reversal symmetry presented an additional difficulty with regard to the reproducibility of the current switches: transitions at the time-reversal-invariant phases are forbidden because these are between the Kramers degenerate

states. As the branch switches are coincidental with the time-reversal-invariant phases, relaxation processes happening in close vicinity to these switches are slower relative to analogous processes not bound by time-reversal symmetry.

Our findings on topological Josephson junctions allow for quantitative predictions of the Josephson current relative to the excitation spectrum and a small number of directly and independently measurable junction parameters. With respect to a finite phase sweep, our results revealed salient, qualitative characteristics of the supercurrent in the form of switches that herald the nontrivial topology and symmetry inherent in these systems. Additionally, the application of the master equation technique enabled us to examine how some of these topological features can be robustly established in terms of the phase sweep speed and a general time-reversal-invariant relaxation rate. Owing to the highly general features that we find, our work may be of aid in experimental endeavours involving junctions between time-reversal-invariant topological superconductors.

Appendix A

Spectral theory for real antisymmetric matrices

Consider a real antisymmetric square matrix A of order $2N$ which, by definition, satisfies the property

$$A = -A^{\mathsf{T}}. \tag{A.1}$$

It follows that iA is Hermitian and hence the eigenvalues of A are imaginary. Moreover, the characteristic equation for an eigenvalue λ_n is augmented by the relation

$$\det\left(A + \lambda_n \mathbb{1}\right) = 0, \tag{A.2}$$

from which it follows that A has eigenvalues occurring in pairs $\{\pm i\lambda_1, \pm i\lambda_2, \ldots, \pm i\lambda_N\}$. Note also that the square of A is real symmetric since

$$A^2 = A^{\mathsf{T}} A^{\mathsf{T}} = (A^2)^{\mathsf{T}}. \tag{A.3}$$

Given that A^2 has eigenvectors $\mathbf{v}_n$ with corresponding eigenvalues -λ_n^2, then

$$-\lambda_n^2 \mathbf{v}_m^\mathsf{T} \mathbf{v}_n = \mathbf{v}_m^\mathsf{T} A^2 \mathbf{v}_n = \left(A^2 \mathbf{v}_m\right)^\mathsf{T} \mathbf{v}_n = -\lambda_m^2 \mathbf{v}_m^\mathsf{T} \mathbf{v}_n \tag{A.4}$$

so that

$$-\left(\lambda_m^2 - \lambda_n^2\right) \mathbf{v}_m^\mathsf{T} \mathbf{v}_n = 0 \tag{A.5}$$

which demonstrates that the eigenvectors, provided that they have distinct eigenvalues, are orthogonal. Therefore, A^2 has the eigendecomposition

$$A^2 = O^\mathsf{T} \begin{bmatrix} -\lambda_1^2 \mathbb{1}_2 & 0 & \dots & 0 & 0 \\ 0 & -\lambda_2^2 \mathbb{1}_2 & \dots & 0 & 0 \\ \vdots & \vdots & \ddots & \vdots & \vdots \\ 0 & 0 & \dots & -\lambda_{N-1}^2 \mathbb{1}_2 & 0 \\ 0 & 0 & \dots & 0 & -\lambda_N^2 \mathbb{1}_2 \end{bmatrix} O \tag{A.6}$$

where O is an orthogonal matrix. By taking an antisymmetric square root of the above equation, A may be decomposed via

$$A = O^\mathsf{T} \begin{bmatrix} i\lambda_1 \sigma_2 & 0 & \dots & 0 & 0 \\ 0 & i\lambda_2 \sigma_2 & \dots & 0 & 0 \\ \vdots & \vdots & \ddots & \vdots & \vdots \\ 0 & 0 & \dots & i\lambda_{N-1} \sigma_2 & 0 \\ 0 & 0 & \dots & 0 & i\lambda_N \sigma_2 \end{bmatrix} O \tag{A.7}$$

where, without loss of generality, we take $\lambda_n \geq 0$ for integers $1 < n < N$.

Appendix B

Time-reversal symmetry and particle-hole symmetry in an alternative basis

A new basis is motivated and the conditions that the scattering matrix must obey due to particle-hole symmetry and time-reversal symmetry must be updated. The use of this basis is twofold: it results in the s-wave superconducting pairing becoming proportional to the identity matrix and allows for a simple time-reversal relation between the electron part and the hole part of the Bogoliubov–de Gennes Hamiltonian.

The new basis for the scattering matrix is represented by S, while the old basis, as used in Sec. 2.3.1, is represented by S'. The transformation to the new basis is

$$S(E) = ZS'(E)Z^{\mathsf{T}}, \tag{B.1}$$

where $Z = \mathbb{1}_2 \oplus i\sigma_2$. Since Z only contains real elements and the time-reversal operator has the form $\mathcal{T} = i\sigma_2 K$, then each submatrix of Z commutes with that of $\mathcal{T}$. As a result, the condition imposed by time-reversal symmetry on the scattering matrix remains

unchanged, i.e.

$$S\left(E\right)=\breve{\sigma}_{2}S\left(E\right)^{\mathsf{T}}\breve{\sigma}_{2}. \tag{B.2}$$

Note also that, if there is no cross-scattering between electrons and holes, then by utilising the electron-hole structure of S,

$$S=\begin{bmatrix}S_{\mathrm{e}} & 0\\ 0 & S_{\mathrm{h}}\end{bmatrix}, \tag{B.3}$$

the condition can be expressed as

$$S_{\mathrm{e}}\left(E\right)=\sigma_{2}S_{\mathrm{e}}\left(E\right)^{\mathsf{T}}\sigma_{2}. \tag{B.4}$$

In the old basis, particle-hole symmetry required that

$$S'\left(E\right)=\hat{\sigma}_{1}S'\left(-E\right)^{*}\hat{\sigma}_{1} \tag{B.5}$$

where $\hat{\sigma}_{1}=\sigma_{1}\otimes\mathbb{1}_{2}$. By recognising that

$$i\hat{\sigma}_{2}\breve{\sigma}_{2}=-\begin{bmatrix}\mathbb{1}_{2} & 0\\ 0 & i\sigma_{2}\end{bmatrix}\begin{bmatrix}0 & \mathbb{1}_{2}\\ \mathbb{1}_{2} & 0\end{bmatrix}\begin{bmatrix}\mathbb{1}_{2} & 0\\ 0 & i\sigma_{2}^{\mathsf{T}}\end{bmatrix}, \tag{B.6}$$

then, in the new basis, the particle-hole symmetry condition becomes

$$S\left(E\right)=i\hat{\sigma}_{2}\breve{\sigma}_{2}S'\left(-E\right)^{*}i\hat{\sigma}_{2}\breve{\sigma}_{2}, \tag{B.7}$$

so that the particle-hole operator is now $\mathcal{C}=i\hat{\sigma}_{2}\breve{\sigma}_{2}K$. Furthermore, the electron-hole structure of S [as in Eq. (B.3)] allows for this property to be expressed succinctly as

$$S_{\mathrm{h}}\left(E\right)=\mathcal{T}S_{\mathrm{e}}\left(-E\right)\mathcal{T}^{-1}. \tag{B.8}$$

In terms of the Bogoliubov–de Gennes Hamiltonian in the old basis, we have

$$H' = \begin{bmatrix} h & \Delta \\ -\Delta^* & -h^* \end{bmatrix}, \tag{B.9}$$

and upon transforming to the new basis, this becomes

$$H = \begin{bmatrix} h & -\Delta i\sigma_2 \\ -i\sigma_2\Delta^* & -i\sigma_2 h^* i\sigma_2^{\mathsf{T}} \end{bmatrix}, \tag{B.10}$$

where it becomes evident that the hole part of the Hamiltonian h_{h} can be expressed in terms of the electron part $h_{\mathrm{e}} = h$ via

$$h_{\mathrm{h}} = -\mathcal{T} h_{\mathrm{e}} \mathcal{T}^{-1} \tag{B.11}$$

Furthermore, the s-wave component in the old basis $\Delta_s = \Delta_0 i\sigma_2$ therefore becomes proportional to the unit matrix in the new basis.

Appendix C

Scattering calculations for the time-reversal-invariant Josephson junction

Here we provide a more detailed outline of how the amplitudes used in the matrices of Eq. (3.36), which describe the scattering about the normal–superconductor interfaces in the time-reversal-invariant Josephson junction, are calculated.

Taking the Hamiltonian in Eq. (3.1) where $h_{\mathrm{e}} = -i\hbar v_{\mathrm{F}} \mathbb{1}_2 \partial_x$ is taken to be linearised and $\Delta = \Delta_s \mathbb{1}_2 - \Delta_p \sigma_1$, we make a unitary transformation described by the matrix $\mathbb{1}_2 \otimes U$, where

$$U = \frac{1}{\sqrt{2}} \begin{bmatrix} 1 & 1 \\ 1 & -1 \end{bmatrix}, \tag{C.1}$$

to diagonalise the Bogoliubov–de Gennes Hamiltonian in spin-space. In terms of the s-wave and p-wave pairings Δ_s and Δ_p,

$$U \Delta U^{\dagger} = \Delta_s \mathbb{1}_2 - \Delta_p \sigma_3, \tag{C.2}$$

which decouples the 4×4 Bogoliubov–de Gennes Hamiltonian into two 2×2 blocks

$$H_{\pm} = \begin{bmatrix} -i\hbar v_{\pm}\partial_x & \Delta_{\pm} e^{i\phi/2} \\ \Delta_{\pm} e^{-i\phi/2} & i\hbar v_{\pm}\partial_x \end{bmatrix}, \tag{C.3}$$

where $v_{\pm}$ are the Fermi velocities and $\Delta_{\pm} = \Delta_s \pm \Delta_p$. This effectively reduces the scattering problem to two single-channel copies (which differ from one another by the pairing amplitude) of the problem originally treated in the multi-channel case by Beenakker [15].

C.1 Subgap scattering

The calculation for the subgap scattering amplitudes associated with Andreev reflection is very similar to the spinless s-wave case in Sec. 2.3.2. For example, consider an impinging electron at a normal–superconductor interface (i.e. with the superconductor to the right of the normal conductor) placed at $x = 0$ with superconducting phase $\phi/2$, where the wavefunctions take the form

$$\Psi\left(x < 0\right) = \begin{bmatrix} e^{ixE/\hbar v_{\pm}} \\ r'_{\mathrm{h}\pm} e^{-ixE/\hbar v_{\pm}} \end{bmatrix}, \quad \Psi\left(x > 0\right) = \begin{bmatrix} f_{\mathrm{e}\pm} \\ f_{\mathrm{h}\pm} \end{bmatrix} C e^{-x\sqrt{\Delta_{\pm}^2 - E^2}/\hbar v_{\pm}}. \tag{C.4}$$

By enforcing continuity of the wavefunction at $x = 0$, the solution of the Bogoliubov–de Gennes equations [Eq. (C.3)] for the Andreev amplitudes $r'_{\mathrm{h}\pm}$ yields

$$r'_{\mathrm{h}\pm} = e^{-i\phi/2}\alpha_{\pm}, \tag{C.5}$$

where $\alpha_{\pm} = e^{-i \arccos\left(E/\Delta_{\pm}\right)}$. For an impinging hole at the same interface, this amounts to letting $v_{\pm} \mapsto -v_{\pm}$ and $\Delta_p \mapsto -\Delta_p$ in $H_{\pm}$. The Bogoliubov–de Gennes equations then yield amplitudes

$$r'_{\mathrm{e}\pm} = e^{i\phi/2}\alpha_{\pm}. \tag{C.6}$$

The case of a superconductor–normal interface (i.e. with the superconductor to the left of the normal conductor) with phase parameter $-\phi/2$ is identical to the cases just considered, except that the velocity and phase parameter have flipped sign, so the corresponding Andreev reflection amplitudes follow by letting $\pm \mapsto \mp$ and $\phi \mapsto -\phi$ in Eqs. (C.5) and (C.6).

We now make explicit the distinction between the pairing amplitudes of the right superconductor $\Delta_{\pm\mathrm{R}}$ and the left superconductor $\Delta_{\pm\mathrm{L}}$, with $\alpha_{\pm L,R}$ similarly defined. The submatrices

$$\kappa_{1o} = \begin{bmatrix} \alpha_{-o} & 0 \\ 0 & \alpha_{+o} \end{bmatrix} e^{-i\frac{\phi}{2}}, \quad \kappa_{2o} = \begin{bmatrix} \alpha_{+o} & 0 \\ 0 & \alpha_{-o} \end{bmatrix} e^{i\frac{\phi}{2}}, \tag{C.7}$$

represent hole-to-electron reflection amplitudes in the cases of $\kappa_{1\mathrm{L}}$ and $\kappa_{2\mathrm{R}}$ and electron-to-hole reflection amplitudes in the cases of $\kappa_{2\mathrm{L}}$ and $\kappa_{1\mathrm{R}}$. This ultimately results in the Andreev reflection blocks as they appear in Eq. (3.5).

C.2 Scattering above all gaps

By considering modes in the junction with an energy greater than either gap of the superconductors, the scattering problem changes as a result of the modes being able to indefinitely extend through either superconducting lead. As a result, one must additionally consider the effect of modes being transmitted through to the superconducting leads and also the reflection and transmission processes at the junction associated with modes that originate from deep within the superconducting leads.

First, consider an electron emanating from the normal side onto a normal–superconductor interface at $x = 0$. The wavefunctions take the form

$$\Psi\left(x<0\right) = \begin{bmatrix} e^{ixE/\hbar v_\pm} \\ r'_{\mathrm{h}\pm} e^{-ixE/\hbar v_\pm} \end{bmatrix}, \quad \Psi\left(x>0\right) = \frac{t'_{\mathrm{e}\pm}}{\left|\sqrt{\left|f_{\mathrm{e}\pm}\right|^2 - \left|f_{\mathrm{h}\pm}\right|^2}\right|} \begin{bmatrix} f_{\mathrm{e}\pm} \\ f_{\mathrm{h}\pm} \end{bmatrix} e^{ix\sqrt{E^2-\Delta_\pm^2}/\hbar v_\pm}. \tag{C.8}$$

Solution of the Bogoliubov–de Gennes equations [Eq. (C.3)], enforcement of the continuity of the wavefunctions at $x = 0$, and the free choice that $f_{\mathrm{e}} = 1$ results in the following transmission $t'_{\mathrm{e}\pm}$ and Andreev reflection $r'_{\mathrm{h}\pm}$ amplitudes

$$t'_{\mathrm{e}\pm} = \sqrt{1 - \alpha_{\pm}^2}, \quad r'_{\mathrm{h}\pm} = \alpha_{\pm} e^{-i\phi/2}. \tag{C.9}$$

As with the subgap case, an impinging hole at the same interface follows by letting $v_{\pm} \mapsto -v_{\pm}$ and $\Delta_p \mapsto -\Delta_p$ in the Bogoliubov–de Gennes Hamiltonian, resulting in the analogous amplitudes

$$t'_{\mathrm{h}\pm} = \sqrt{1 - \alpha_{\pm}^2}, \quad r'_{\mathrm{e}\pm} = \alpha_{\pm} e^{i\phi/2}. \tag{C.10}$$

For a superconductor–normal interface, both the phase parameter and velocity flip sign, so that the corresponding amplitudes for reflection and transmission are the same as in Eqs. (C.9) and (C.10), but with $\pm \mapsto \mp$ and $\phi \mapsto -\phi$.

An electron-like particle, originating from deep within the right superconductor, incident upon a normal–superconductor interface at $x = 0$ is described by the wavefunction

$$\begin{aligned} \Psi(x > 0) = & \frac{1}{\left| \sqrt{\left| f_{\mathrm{e}}^{\mathrm{in}} \right|^2 - \left| f_{\mathrm{h}}^{\mathrm{in}} \right|^2} \right|} \begin{bmatrix} f_{\mathrm{e}}^{\mathrm{in}} \\ f_{\mathrm{h}}^{\mathrm{out}} \end{bmatrix} e^{-ix\sqrt{E^2 - \Delta_{\pm}^2}/\hbar v_{\pm}} \\ & + \frac{r_{\mathrm{h}\pm}}{\left| \sqrt{\left| f_{\mathrm{e}}^{\mathrm{out}} \right|^2 - \left| f_{\mathrm{h}}^{\mathrm{out}} \right|^2} \right|} \begin{bmatrix} f_{\mathrm{e}}^{\mathrm{out}} \\ f_{\mathrm{h}}^{\mathrm{out}} \end{bmatrix} e^{ix\sqrt{E^2 - \Delta_{\pm}^2}/\hbar v_{\pm}}, \end{aligned} \tag{C.11}$$

while the part transmitted through to the normal side has the wavefunction

$$\Psi(x < 0) = \begin{bmatrix} t_{\mathrm{e}\pm} \\ 0 \end{bmatrix} e^{-ixE/\hbar v_{\pm}}. \tag{C.12}$$

Solving the Bogoliubov–de Gennes equations [Eq. (C.3)] for the electron-like and hole-like components, enforcing continuity of the wavefunctions at $x = 0$, and choosing $f_{\mathrm{e}}^{\mathrm{in}} =$

$f_{\mathrm{h}}^{\mathrm{out}} = 1$ results in the following transmission $t_{\mathrm{e}\pm}$ and Andreev reflection $r_{\mathrm{h}\pm}$ amplitudes

$$t_{\mathrm{e}\pm} = \sqrt{1-\alpha_{\pm}^2}, \quad r_{\mathrm{h}\pm} = -\alpha_{\pm} e^{-i\phi/2}. \tag{C.13}$$

Likewise for an incident hole-like particle, the amplitudes follow from the reversed velocity and p-wave pairing components, so that

$$t_{\mathrm{h}\pm} = \sqrt{1-\alpha_{\pm}^2}, \quad r_{\mathrm{e}\pm} = -\alpha_{\pm} e^{i\phi/2}. \tag{C.14}$$

The amplitudes for the identical processes which occur at a superconductor–normal interface follow as usual due to the sign reversal in the velocity and phase parameter, so that they are just Eqs. (C.13) and (C.14) with $\pm \mapsto \mp$ and $\phi \mapsto -\phi$.

Combining all of these amplitudes together, one can write the full set of submatrices $\hat{R}', \hat{T}', \hat{R}$, and $\hat{T}$ which form the scattering matrix of the total junction S_{SNS}. Keeping in mind the electron-hole structure of the Hamiltonian [Eq. (3.3)], which is ordered further according to each Fermi point and yet further by spin, these matrices take the form

$$\hat{R}' = \begin{bmatrix} 0 & 0 & \kappa_{1\mathrm{L}} & 0 \\ 0 & 0 & 0 & \kappa_{2\mathrm{R}} \\ \kappa_{2\mathrm{L}} & 0 & 0 & 0 \\ 0 & \kappa_{1\mathrm{R}} & 0 & 0 \end{bmatrix}, \quad \hat{R} = -\begin{bmatrix} 0 & 0 & \kappa_{2\mathrm{L}}^* & 0 \\ 0 & 0 & 0 & \kappa_{1\mathrm{R}}^* \\ \kappa_{1\mathrm{L}}^* & 0 & 0 & 0 \\ 0 & \kappa_{2\mathrm{R}}^* & 0 & 0 \end{bmatrix}, \tag{C.15}$$

for the reflection matrices and

$$\begin{aligned} \hat{T}' = \mathrm{diag}\Big(&\sqrt{1-\alpha_{+L}^2}, \sqrt{1-\alpha_{-L}^2}, \sqrt{1-\alpha_{-R}^2}, \sqrt{1-\alpha_{+R}^2}, \\ &\sqrt{1-\alpha_{-L}^2}, \sqrt{1-\alpha_{+L}^2}, \sqrt{1-\alpha_{+R}^2}, \sqrt{1-\alpha_{-R}^2} \Big), \end{aligned} \tag{C.16}$$

$$\begin{aligned} \hat{T} = \mathrm{diag}\Big(&\sqrt{1-\alpha_{-L}^2}, \sqrt{1-\alpha_{+L}^2}, \sqrt{1-\alpha_{+R}^2}, \sqrt{1-\alpha_{-R}^2}, \\ &\sqrt{1-\alpha_{+L}^2}, \sqrt{1-\alpha_{-L}^2}, \sqrt{1-\alpha_{-R}^2}, \sqrt{1-\alpha_{+R}^2} \Big), \end{aligned} \tag{C.17}$$

for the transmission matrices, from which one may verify that the relations in Eq. (3.38),

where σ_1 is the first Pauli matrix acting in spin-space, are true. In addition to these relations, one also has

$$\hat{R}' = \hat{T}\hat{R}'\hat{T}'^{-1}, \quad \hat{R}'^{\dagger} = \sigma_1 \hat{R}' \sigma_1, \tag{C.18}$$

from which S_{SNS} can be simplified via

$$\begin{aligned} S_{\mathrm{SNS}} &= \hat{R} + \hat{T}' \left(\mathbb{1}_8 - S_{\mathrm{N}} \hat{R}' \right)^{-1} S_{\mathrm{N}} \hat{T} \\ &= \hat{T}' \sigma_1 \left[-\hat{R}' + \sigma_1 \left(\mathbb{1}_8 - S_{\mathrm{N}} \hat{R}' \right)^{-1} S_{\mathrm{N}} \sigma_1 \left(\mathbb{1}_8 + \hat{R}\hat{R}' \right) \right] \hat{T}'^{-1} \sigma_1 \\ &= \hat{T}' \left[\left(\mathbb{1}_8 + S_{\mathrm{N}} \hat{R}' + \dots \right) S_{\mathrm{N}} \sigma_1 - \left(\sigma_1 \hat{R}' + S_{\mathrm{N}} \hat{R}' \sigma_1 \hat{R}' + \dots \right) \right] \hat{T}'^{-1} \sigma_1 \\ &= \hat{T}' \left(\mathbb{1}_8 - S_{\mathrm{N}} \hat{R}' \right)^{-1} \left(S_{\mathrm{N}} \sigma_1 - \sigma_1 \hat{R}' \right) \hat{T}'^{-1} \sigma_1. \end{aligned} \tag{C.19}$$

C.3 Scattering between the gaps

An intergap regime for the junction is generally possible, either owing to a gap asymmetry across the junction, $\Delta_- \neq \Delta_+$, or some combination of the two, so that the submatrices describing reflection and transmission will be of a different size depending on the intergap configuration. The general form of S_{SNS} as it appears in Eq. (3.36), however, remains the same.

The new submatrices which appear can be derived from the general above-the-gap blocks that appear in Eqs. (C.15)–(C.17). The trivial case is with $\hat{R}'$, which maintains its above-the-gap form as it describes Andreev reflections from subgap scatterers inside the junction. A general method to update the other blocks is as follows: delete the corresponding rows and columns of $\hat{R}$ which are associated with modes no longer able to extend indefinitely through their respective superconductor, and then to delete the corresponding rows of $\hat{T}'$ and columns of $\hat{T}$ or make their corresponding entries equivalent to zero (whichever preserves the order of S_{SNS}).

For the topological–topological junction, we only consider the gap-symmetric case,

so the only intergap regime that must be considered are for energies spanning $|\Delta_-| < E < \Delta_+$.

For the nontopological–topological junction, four regimes each with up to two subregimes arise. These depend on the superconducting order parameters of each superconductor, with the three main regime types that are possible being

$$\begin{aligned} &(1) : \Delta_0 < \Delta_- \leq \Delta_+, \\ &(2) : \Delta_- \leq \Delta_0 \leq \Delta_+, \\ &(3) : \Delta_- \leq \Delta_+ < \Delta_0. \end{aligned} \tag{C.20}$$

Bibliography

[1] E. Majorana, *Teoria simmetrica dell'elettrone e del positrone,* Nuovo Cimento **14**, 171 (1937).

[2] F. Wilczek, *Majorana returns,* Nature Phys. **5**, 614 (2009).

[3] G. E. Volovik, *Fermion zero modes on vortices in chiral superconductors,* JETP Lett. **70**, 609 (1999).

[4] T. Senthil and M. P. A. Fisher, *Quasiparticle localization in superconductors with spin-orbit scattering,* Phys. Rev. B **61**, 9690 (2000).

[5] N. Read and D. Green, *Paired states of fermions in two dimensions with breaking of parity and time-reversal symmetries and the fractional quantum Hall effect,* Phys. Rev. B **61**, 10267 (2000).

[6] A. Y. Kitaev, *Unpaired Majorana fermions in quantum wires,* Phys.-Usp **44**, 131 (2001).

[7] A. P. Schnyder, S. Ryu, A. Furusaki, and A. W. W. Ludwig, *Classification of topological insulators and superconductors in three spatial dimensions,* Phys. Rev. B **78**, 195125 (2008).

[8] J. Alicea, *New directions in the pursuit of Majorana fermions in solid state systems,* Rep. Prog. Phys **75**, 076501 (2012).

[9] C. W. J. Beenakker, *Search for Majorana Fermions in Superconductors,* Annu. Rev. Condens. Matter Phys. **4**, 113 (2013).

[10] L. Fu and C. L. Kane, *Superconducting Proximity Effect and Majorana Fermions at the Surface of a Topological Insulator,* Phys. Rev. Lett. **100**, 096407 (2008).

[11] F. Hassler, A. R. Akhmerov, C.-Y. Hou, and C. W. J. Beenakker, *Anyonic interferometry without anyons: how a flux qubit can read out a topological qubit,* New Journal of Physics **12**, 125002 (2010).

[12] T. Hyart, B. van Heck, I. C. Fulga, M. Burrello, A. R. Akhmerov, and C. W. J. Beenakker, *Flux-controlled quantum computation with Majorana fermions,* Phys. Rev. B **88**, 035121 (2013).

[13] S. Das Sarma, M. Freedman, and C. Nayak, *Majorana Zero Modes and Topological Quantum Computation,* npj Quantum Information **1**, 15001 (2015).

[14] W. Haberkorn, H. Knauer, and J. Richter, *A Theoretical Study of the Current-Phase Relation in Josephson Contacts,* Phys. Status Solidi A **47**, K161 (1978).

[15] C. W. J. Beenakker, *Universal limit of critical-current fluctuations in mesoscopic Josephson junctions,* Phys. Rev. Lett. **67**, 3836 (1991).

[16] Y. Tanaka and S. Kashiwaya, *Theory of the Josephson effect in d-wave superconductors,* Phys. Rev. B **53**, R11957 (1996).

[17] Y. Tanaka and S. Kashiwaya, *Theory of Josephson effects in anisotropic superconductors,* Phys. Rev. B **56**, 892 (1997).

[18] R. A. Riedel and P. F. Bagwell, *Low-temperature Josephson current peak in junctions with d-wave order parameters,* Phys. Rev. B **57**, 6084 (1998).

[19] S. Kashiwaya and Y. Tanaka, *Tunnelling effects on surface bound states in unconventional superconductors,* Rep. Prog. Phys. **63**, 1641 (2000).

[20] J. Bardeen, L. N. Cooper, and J. R. Schrieffer, *Theory of Superconductivity,* Phys. Rev. **108**, 1175 (1957).

[21] J. Sólyom, *Fundamentals of the Physics of Solids Volume 2 – Electronic Properties* (Springer-Verlag Berlin Heidelberg, 2009).

[22] J. Sólyom, *Fundamentals of the Physics of Solids Volume 3 – Normal, Broken-Symmetry, and Correlated Systems* (Springer-Verlag Berlin Heidelberg, 2010).

[23] A. Altland and B. Simons, *Condensed Matter Field Theory* (Cambridge University Press, New York, 2010).

[24] N. N. Bogoljubov, *On a new method in the theory of superconductivity,* Il Nuovo Cimento **7**, 794 (1958).

[25] J. G. Valatin, *Comments on the theory of superconductivity,* Il Nuovo Cimento **7**, 843 (1958).

[26] F. Haake, *Quantum Signatures of Chaos* (Springer-Verlag Berlin Heidelberg, 2010).

[27] M. Z. Hasan and C. L. Kane, *Colloquium: Topological insulators,* Rev. Mod. Phys. **82**, 3045 (2010).

[28] M. Nakahara, *Geometry, Topology and Physics* (Institute of Physics Publishing, 2003).

[29] C. W. J. Beenakker, *Random-matrix theory of Majorana fermions and topological superconductors,* Rev. Mod. Phys. **87**, 1037 (2015).

[30] D. C. Youla, *A normal form for a matrix under the unitary congruence group,* Canad. J. Math **13**, 694 (1961).

[31] E. P. Wigner, *Group Theory and Its Application to the Quantum Mechanics of Atomic Spectra* (Academic Press, 1959).

[32] J. J. Sakurai, *Modern Quantum Mechanics* (Addison-Wesley Publishing Company, 1994).

[33] A. Zee, *Quantum Field Theory in a Nutshell* (Princeton University Press, 2010).

[34] M. Stone and P. Goldbart, *Mathematics for Physics: A Guided Tour for Graduate Students* (Cambridge University Press, 2009).

[35] H. A. Kramers, *Théorie générale de la rotation paramagnétique dans les cristaux,* Proceedings Koninklijke Akademie van Wetenschappen **33**, 959 (1930).

[36] R. Landauer, *Spatial Variation of Currents and Fields Due to Localized Scatterers in Metallic Conduction,* IBM J. Res. Develop. **1**, 223 (1963).

[37] R. Landauer, *Electrical resistance of disordered one-dimensional lattices,* Phil. Mag. **21**, 863 (1970).

[38] M. Büttiker, *Scattering theory of thermal and excess noise in open conductors,* Phys. Rev. Lett. **65**, 2901 (1990).

[39] M. Büttiker, *Scattering theory of current and intensity noise correlations in conductors and wave guides,* Phys. Rev. B **46**, 12485 (1992).

[40] Y. Blanter and M. Büttiker, *Shot noise in mesoscopic conductors,* Phys. Rep. **336**, 1 (2000).

[41] H. Bruus and K. Flensberg, *Many-Body Quantum Theory in Condensed Matter Physics: An Introduction* (Oxford University Press, 2004).

[42] M. V. Moskalets, *Scattering Matrix Approach to Non-Stationary Quantum Transport* (Imperial College Press, 2012).

[43] G. E. Blonder, M. Tinkham, and T. M. Klapwijk, *Transition from metallic to tunneling regimes in superconducting microconstrictions: Excess current, charge imbalance, and supercurrent conversion,* Phys. Rev. B **25**, 4515 (1982).

[44] A. F. Andreev, *The Thermal Conductivity of the Intermediate State in Superconductors,* Zh. Eksp. Teor. Fiz. **46**, 1823 (1964), [Sov. Phys. JETP **19**, 1228 (1964)].

[45] Y. Nazarov and Y. Blanter, *Quantum Transport* (Cambridge University Press, New York, 2009).

[46] P. A. Mello, P. Pereyra, and N. Kumar, *Macroscopic Approach to Multichannel Disordered Conductors,* Annals of Physics **181**, 290 (1988).

[47] T. Martin and R. Landauer, *Wave-packet approach to noise in multichannel mesoscopic systems,* Phys. Rev. B **45**, 1742 (1982).

[48] E. Akkermans, A. Auerbach, J. E. Avron, and B. Shapiro, *Relation between persistent currents and the scattering matrix,* Phys. Rev. Lett. **66**, 76 (1991).

[49] L.-F. Chang and P. F. Bagwell, *Ballistic Josephson-current flow through an asymmetric superconductor–normal-metal–superconductor junction,* Phys. Rev. B **49**, 15853 (1994).

[50] L. Fu and C. L. Kane, *Josephson current and noise at a superconductor/quantum-spin-Hall-insulator/superconductor junction,* Phys. Rev. B **79**, 161408(R) (2009).

[51] P. A. Ioselevich and M. V. Feigel'man, *Anomalous Josephson Current via Majorana Bound States in Topological Insulators,* Phys. Rev. Lett **106**, 077003 (2011).

[52] B. van Heck, F. Hassler, A. R. Akhmerov, and C. W. J. Beenakker, *Coulomb stability of the 4π-periodic Josephson effect of Majorana fermions,* Phys. Rev. B **84**, 180502(R) (2011).

[53] L. Jiang, D. Pekker, J. Alicea, G. Refael, Y. Oreg, and F. von Oppen, *Unconventional Josephson Signatures of Majorana Bound States,* Phys. Rev. Lett **107**, 236401 (2011).

[54] P. San-Jose, E. Prada, and R. Aguado, *ac Josephson Effect in Finite-Length Nanowire Junctions with Majorana Modes,* Phys. Rev. Lett **108**, 257001 (2012).

[55] F. Domínguez, F. Hassler, and G. Platero, *Dynamical detection of Majorana fermions in current-biased nanowires,* Phys. Rev. B **86**, 140503(R) (2012).

[56] F. Zhang, C. L. Kane, and E. J. Mele, *Time-Reversal-Invariant Topological Superconductivity and Majorana Kramers pairs,* Phys. Rev. Lett **111**, 056402 (2013).

[57] S. B. Chung, J. Horowitz, and X.-L. Qi, *Time-reversal anomaly and Josephson effect in time-reversal-invariant topological superconductors,* Phys. Rev. B **88**, 214514 (2013).

[58] X.-J. Liu, C. L. M. Wong, and K. T. Law, *Non-Abelian Majorana doublets in Time-Reversal-Invariant Topological Superconductors,* Phys. Rev. X **4**, 021018 (2014).

[59] D. I. Pikulin, Y. Komijani, and I. Affleck, *Luttinger liquid in contact with a Kramers pair of Majorana bound states,* Phys. Rev. B **93**, 205430 (2016).

[60] P. A. Ioselevich, P. M. Ostrovsky, and M. V. Feigel'man, *Josephson current between topological and conventional superconductors,* Phys. Rev. B **93**, 125435 (2016).

[61] P. Marra, R. Citro, and A. Braggio, *Signatures of topological phase transitions in Josephson current-phase discontinuities,* Phys. Rev. B **93**, 220507 (2016).

[62] X. Liu, X. Li, D.-L. Deng, X.-J. Liu, and S. Das Sarma, *Majorana Spintronics,* Phys. Rev. B **94**, 014511 (2016).

[63] A. Nava, R. Giuliano, G. Campagnano, and D. Giuliano, *Transfer matrix approach to the persistent current in hybrid normal-superconducting rings*, (2016), arXiv:1607.01707 .

[64] L. P. Rokhinson, X. Liu, and J. K. Furdyna, *The fractional ac Josephson effect in a semiconductor-superconductor nanowire as a signature of Majorana particles,* Nature Phys. **8**, 795 (2012).

[65] M. T. Deng, C. L. Yu, G. Y. Huang, M. Larsson, P. Caroff, and H. Q. Xu, *Anomalous Zero-Bias Conductance Peak in a NbInSb NanowireNb Hybrid Device,* Nano Lett. **12**, 6414 (2012).

[66] V. S. Pribiag, A. J. A. Beukman, F. Qu, M. C. Cassidy, C. Charpentier, W. Wegscheider, and L. P. Kouwenhoven, *Edge-mode superconductivity in a two-dimensional topological insulator,* Nat. Nanotechnol. **10**, 593 (2015).

[67] J. Wiedenmann, E. Bocquillon, R. S. Deacon, S. Hartinger, O. Herrmann, T. M. Klapwijk, L. Maier, C. Ames, C. Brüne, C. Gould, A. Oiwa, K. Ishibashi, S. Tarucha, H. Buhmann, and L. W. Molenkamp, *4π-periodic Josephson supercurrent in HgTe-based topological Josephson junctions,* Nature Communications **7**, 10303 (2016).

[68] E. Bocquillon, R. S. Deacon, J. Wiedenmann, P. Leubner, T. M. Klapwijk, C. Brüne, K. Ishibashi, H. Buhmann, and L. W. Molenkamp, *Gapless Andreev bound states in the quantum spin Hall insulator HgTe*, Nat. Nanotechnol. (to be published) (2016), arXiv:1601.08055 .

[69] X.-L. Qi, T. L. Hughes, S. Raghu, and S.-C. Zhang, *Time-Reversal-Invariant Topological Superconductors and Superfluids in Two and Three Dimensions,* Phys. Rev. Lett **102**, 187001 (2009).

[70] R. M. Lutchyn, J. D. Sau, and S. Das Sarma, *Majorana Fermions and a Topological Phase Transition in Semiconductor-Superconductor Heterostructures,* Phys. Rev. Lett **105**, 077001 (2010).

[71] Y. Oreg, G. Refael, and F. von Oppen, *Helical Liquids and Majorana Bound States in Quantum Wires,* Phys. Rev. Lett **105**, 177002 (2010).

[72] M. Duckheim and P. W. Brouwer, *Andreev reflection from noncentrosymmetric superconductors and Majorana bound-state generation in half-metallic ferromagnets,* Phys. Rev. B **83**, 054513 (2011).

[73] S. Nadj-Perge, I. K. Drozdov, B. A. Bernevig, and A. Yazdani, *Proposal for realizing Majorana fermions in chains of magnetic atoms on a superconductor,* Phys. Rev. B **88**, 020407(R) (2013).

[74] S. Nadj-Perge, I. K. Drozdov, J. Li, H. Chen, S. Jeon, J. Seo, A. H. MacDonald, B. A. Bernevig, and A. Yazdani, *Observation of Majorana fermions in ferromagnetic atomic chains on a superconductor,* Science **346**, 602 (2014).

[75] A. Altland and M. R. Zirnbauer, *Nonstandard symmetry classes in mesoscopic normal-superconducting hybrid structures,* Phys. Rev. B **55**, 1142 (1997).

[76] J. Alicea, *Majorana fermions in a tunable semiconductor device,* Phys. Rev. B **81**, 125318 (2010).

[77] S. Nakosai, Y. Tanaka, and N. Nagaosa, *Topological Superconductivity in Bilayer Rashba System,* Phys. Rev. Lett **108**, 147003 (2012).

[78] S. Nakosai, J. C. Budich, Y. Tanaka, B. Trauzettel, and N. Nagaosa, *Majorana Bound States and Nonlocal Spin Correlations in a Quantum Wire on an Unconventional Superconductor,* Phys. Rev. Lett **110**, 117002 (2013).

[79] C. L. M. Wong and K. T. Law, *Majorana Kramers doublets in $d_{x^2-y^2}$-wave superconductors with Rashba spin-orbit coupling,* Phys. Rev. B **86**, 184516 (2012).

[80] K. Sun, C.-K. Chiu, H.-H. Hung, and J. Wu, *Tuning between singlet, triplet, and mixed pairing states in an extended Hubbard chain,* Phys. Rev. B **89**, 104519 (2014).

[81] A. Haim, A. Keselman, E. Berg, and Y. Oreg, *Time-reversal-invariant topological superconductivity induced by repulsive interactions in quantum wires,* Phys. Rev. B **89**, 220504(R) (2014).

[82] J. Klinovaja and D. Loss, *Time-reversal invariant parafermions in interacting Rashba nanowires,* Phys. Rev. B **90**, 045118 (2014).

[83] J. Klinovaja, A. Yacoby, and D. Loss, *Kramers pairs of Majorana fermions and parafermions in fractional topological insulators,* Phys. Rev. B **90**, 155447 (2014).

[84] C. Schrade, A. A. Zyuzin, J. Klinovaja, and D. Loss, *Proximity-Induced π Josephson Junctions in Topological Insulators and Kramers Pairs of Majorana Fermions,* Phys. Rev. Lett. **115**, 237001 (2015).

[85] A. Haim, K. Wölms, E. Berg, Y. Oreg, and K. Flensberg, *Interaction-driven topological superconductivity in one dimension,* Phys. Rev. B **94**, 115124 (2016).

[86] H. Ebisu, B. Lu, J. Klinovaja, and Y. Tanaka, *Theory of time-reversal topological superconductivity in double Rashba wires: symmetries of Cooper pairs and Andreev bound states,* Progr. Theor. Exp. Phys. **2016**, 083I01 (2016).

[87] J. Li, W. Pan, B. A. Bernevig, and R. M. Lutchyn, *Detection of Majorana Kramers Pairs Using a Quantum Point Contact,* Phys. Rev. Lett. **117**, 046804 (2016).

[88] Y. Kim, D. E. Liu, E. Gaidamauskas, J. Paaske, K. Flensberg, and R. M. Lutchyn, *Signatures of Majorana Kramers pairs in superconductor-Luttinger liquid and superconductor-quantum dot-normal lead junctions,* Phys. Rev. B **94**, 075439 (2016).

[89] K. Ishida, Y. Nakai, and H. Hosono, *To what extent iron-pnictide new superconductors have been clarified: a progress report,* J. Phys. Soc. Jpn. **78**, 062001 (2009).

[90] I. I. Mazin, *Superconductivity gets an iron boost,* Nature **464**, 183 (2010).

[91] K. Umezawa, Y. Li, H. Miao, K. Nakayama, Z.-H. Liu, P. Richard, T. Sato, J. B. He, D.-M. Wang, G. F. Chen, H. Ding, T. Takahashi, and S.-C. Wang, *Unconventional Anisotropic s-Wave Superconducting Gaps of the LiFeAs Iron-Pnictide Superconductor,* Phys. Rev. Lett **108**, 037002 (2012).

[92] H.-J. Kwon, K. Sengupta, and V. M. Yakovenko, *Fractional ac Josephson effect in p- and d-wave superconductors,* Eur. Phys. J. B **37**, 349 (2004).

[93] K. T. Law and P. A. Lee, *Robustness of Majorana fermion induced fractional*

Josephson effect in multichannel superconducting wires, Phys. Rev. B **84**, 081304(R) (2011).

[94] P.-G. de Gennes, *Superconductivity of Metals and Alloys* (Westview, Boulder, 1999).

[95] K. K. Likharev, *Superconducting weak links,* Rev. Mod. Phys. **51**, 101 (1979).

[96] B. Béri, J. H. Bardarson, and C. W. J. Beenakker, *Splitting of Andreev levels in a Josephson junction by spin-orbit coupling,* Phys. Rev. B **77**, 045311 (2008).

[97] F. Zhang and C. L. Kane, *Anomalous topological pumps and fractional Josephson effects,* Phys. Rev. B **90**, 020501 (2014).

[98] L. Elster, M. Houzet, and J. S. Meyer, *Magnetic resonance in a singlet-triplet Josephson junction,* Phys. Rev. B **93**, 104519 (2016).

[99] K. T. Law, P. A. Lee, and T. K. Ng, *Majorana Fermion Induced Resonant Andreev Reflection,* Phys. Rev. Lett. **103**, 237001 (2009).

[100] M. Wimmer, A. R. Akhmerov, J. P. Dahlhaus, and C. W. J. Beenakker, *Quantum point contact as a probe of a topological superconductor,* New J. Phys. **13**, 053016 (2011).

[101] D. J. van Woerkom, A. Geresdi, and L. P. Kouwenhoven, *One minute parity lifetime of a NbTiN Cooper-pair transistor,* Nature Phys. **11**, 547 (2015).

[102] N. M. Chtchelkatchev and Y. V. Nazarov, *Andreev Quantum Dots for Spin Manipulation,* Phys. Rev. Lett. **90**, 226806 (2003).

[103] M. C. Koops, G. V. van Duyneveldt, and R. de Bruyn Ouboter, *Direct Observation of the Current-Phase Relation of an Adjustable Superconducting Point Contact,* Phys. Rev. Lett. **77**, 2542 (1996).

[104] M. F. Goffman, R. Cron, A. Levy Yeyati, P. Joyez, M. H. Devoret, D. Esteve, and C. Urbina, *Supercurrent in Atomic Point Contacts and Andreev states,* Phys. Rev. Lett. **85**, 170 (2000).

[105] M. L. Della Rocca, M. Chauvin, B. Huard, H. Pothier, D. Esteve, and C. Urbina, *Measurement of the Current-Phase Relation of Superconducting Atomic Contacts,* Phys. Rev. Lett. **99**, 127005 (2007).

[106] L. Bretheau, Ç. Ö. Girit, H. Pothier, D. Esteve, and C. Urbina, *Exciting Andreev pairs in a superconducting atomic contact,* Nature **499**, 312 (2013).

[107] L. Bretheau, Ç. Ö. Girit, C. Urbina, D. Esteve, and H. Pothier, *Supercurrent Spectroscopy of Andreev States,* Phys. Rev. X **3**, 041034 (2013).

[108] P. Virtanen and P. Recher, *Microwave spectroscopy of Josephson junctions in topological superconductors,* Phys. Rev. B **88**, 144507 (2013).

[109] D. G. Olivares, A. Levy Yeyati, L. Bretheau, Ç. Ö. Girit, H. Pothier, and C. Urbina, *Dynamics of quasiparticle trapping in Andreev levels,* Phys. Rev. B **89**, 104504 (2014).

[110] R. P. Riwar, M. Houzet, J. Meyer, and Y. V. Nazarov, *Shooting quasiparticles from Andreev bound states in a superconducting constriction,* Zh. Eksp. Teor. Fiz. **146**, 1176 (2014), [J. Exp. Theor. Phys. **119**, 1028 (2014)].

[111] M. Zgirski, L. Bretheau, Q. Le Masne, H. Pothier, D. Esteve, and C. Urbina, *Evidence for Long-Lived Quasiparticles Trapped in Superconducting Point Contacts,* Phys. Rev. Lett. **106**, 257003 (2011).

[112] M. Hays, G. de Lange, K. Serniak, and D. J. van Woerkom, *Direct microwave measurement of Andreev-bound-state dynamics in a proximitized semiconducting nanowire*, (2017), arXiv:1711.01645 .

[113] C. Cohen-Tannoudji, J. Dupont-Roc, and G. Grynbeg, *Atom-Photon Interactions: Basic Process and Applications* (Wiley-VCH, 2010).

[114] S. Kryszewski and J. Czechowska-Kryszk, *Master equation - tutorial approach*, (2008), arXiv:0801.1757 .

[115] K. Blum, *Density Matrix Theory and Applications* (Springer-Verlag Berlin Heidelberg, 2012).

[116] C. Gardiner and P. Zoller, *Quantum Noise* (Springer-Verlag Berlin Heidelberg, 2004).

[117] A. Nitzan, *Chemical Dynamics in Condensed Phases* (Oxford University Press, 2006).

[118] L. Fu, *Electron Teleportation via Majorana Bound States in a Mesoscopic Superconductor,* Phys. Rev. Lett. **104**, 056402 (2010).

[119] J. Michelsen and V. S. Shumeiko, *Nonadiabatic Josephson dynamics in junctions with in-gap quasiparticles,* Low Temp. Phys. **36**, 925 (2010).